

Axion Dark Matter from Cosmic String Network

Heejoo Kim[†], Junghyeon Park[†], and Minho Son[†]

[†]*Department of Physics, Korea Advanced Institute of Science and Technology,
291 Daehak-ro, Yuseong-gu, Daejeon 34141, Republic of Korea*

Abstract

We perform the lattice simulation to estimate the axion dark matter abundance radiated from the global cosmic strings in the post-inflationary scenario. The independent numerical confirmation on the recently observed logarithmic growth in both the number of strings per Hubble patch and the spectral index of the power law scaling for the axion spectrum is reported. These logarithmic scalings are checked against two different prescriptions for generating initial random field configurations, namely fat-string type and thermal phase transition. We discuss a possible strong correlation between the axion spectrum and the string evolutions with different initial conditions to support the insensitivity of scaling behaviors against different initial data and we provide a qualitative understanding of it. The impact of various combinations of the power law of the axion spectrum, nonlinearities around the QCD scale, and average inter-string distances on the axion abundance is discussed. Additionally, we introduce a new novel string identification method, based on the tetrahedralization of the space, which guarantees the connectedness of the strings and provides a convenient way of assigning the core location. Finally we derive the lower bound on the axion mass.

Contents

1	Introduction	3
2	Formation of cosmic strings	5
3	Simulation Setup	6
3.1	Discretization	6
3.2	Initial conditions and Relaxation	7
4	String identification on tetrahedron	8
5	Scaling regime	9
5.1	Scaling of inter-string distances	12
6	Cosmological evolution of string network	13
6.1	Energy density	13
6.2	String tension and boost factor	15
7	Axion spectrum	18
7.1	Power law scaling	21
8	Axion abundance	24
8.1	Bound on axion mass	26
9	Correlation between strings and axion spectrum	27
10	Conclusion	28
A	Equation of motion	29
B	Evolutions on the lattice	30
B.1	Common setup	30
B.2	Fat string pre-evolution: $R(t) \propto \sqrt{t}$	32
B.3	Fat string pre-evolution: $R(t) \propto t$	33
B.4	From pre-evolution to physical one	34
B.5	Thermal pre-evolution	34
B.6	Random initial conditions	35
B.7	Tetrahedron-based string identification	36
B.8	Masking	37
C	Dependency on initial conditions and relaxations	38

C.1	Scaling regime and fitting	38
C.2	Cosmological evolution of string network	41
C.2.1	Energy budget	41
C.2.2	Instantaneous emission	41
D	More on axion spectrum	44
D.1	Fitting instantaneous emission function	44
D.2	Analytic understanding of positive correlation	48
E	More on axion abundance	49
E.1	Estimation for $q > 1$	50
E.2	Estimation for $q = 1$	54

1 Introduction

Axion as dark matter has been increasingly attractive, although it was originally introduced in some extensions of the Standard Model to resolve a mysterious fine-tuning in quantum chromodynamics (QCD) [1–6]. While the QCD axion dark matter scenario is a certainly interesting possibility ([7] for a review), its dominant production mechanism is still inconclusive. The topological production such as axions radiated from the global cosmic string network [8] formed during the phase transition of the Peccei-Quinn (PQ) symmetry breaking [1] after inflation in the early universe can be predicted in terms of the symmetry breaking scale. However, it entirely relies on the numerical simulation as the effective field theory (EFT) description does not work due to the evolution occurring between two vastly different scales for the PQ symmetry breaking and QCD crossover and the nonlinearity of the equation of motion. While the precise estimation of the topological production with respect to the misalignment mechanism has been subject to a large uncertainty, any progress for the improvement should be crucial in understanding its origin and role of the QCD axion as the dark matter. Especially, the outcome will have a large impact on the direct search for the QCD axion as the ballpark for the natural axion mass will change.

Using the advanced computing resources, some state-of-art simulations have been performed by several groups on the largest lattice grids of the order $\mathcal{O}(2^{12\sim 13})$ per a dimension. An intriguing discovery of those recent simulations was the strong evidence for the scaling regime, or an attractor solution, exhibiting the logarithmic growth in the number of long strings per Hubble patch, denoted by ξ [9–16]. In this work, we independently confirm the logarithmic growth within the simulation time coverage. Since the cosmic strings will eventually decay into axions in late times, the evolution of ξ is an important property that has to be estimated as precise as possible to determine the axion abundance. If the logarithmic growth in ξ holds until the late times for the QCD crossover, its prediction will be very different from the constant scaling scenario of the order one value [17]. The similar constant scaling behaviors observed in early simulations on the smaller lattice grids [18–23] may not be helpful to support either scenario due to the limited dynamic time range (see related discussions in [24–28]).

The differential axion energy spectrum is another crucial property for the accurate estimation of the axion abundance. In the absence of any non-trivial new scale between the scale of the PQ symmetry breaking and the QCD phase transition, it is expected to follow the power law fall-off behavior. The characteristic scaling feature of the axions radiated from the topological cosmic strings can be captured by the instantaneous emission. However, there has been a disagreement in the determination of the power law scaling $\sim k^{-q}$ in the instantaneous axion emission spectrum. While the static lattice simulation performed in [14] finds a hint on the logarithmic growth of the spectral index q in time, an independent simulation in [15] by the adaptive mesh refinement (AMR) ¹ [33] finds a consistency with the no-log hypothesis. The

¹The AMR method can parametrically extend the simulation time by locally increasing the lattice resolution with recursively created finer grids around strings on-the-fly. The AMReX [29, 30], a software for block-structured AMR, was adopted in [15]. GRChombo [31] is another AMR based open-source code originally developed for

former predicts the dominant topological production over the misalignment mechanism (which favors a heavier axion mass than the natural ballpark for the QCD axions from misalignments) whereas the latter predicts a comparable size. Two simulation results in [14, 15] were obtained by different setups, differing by how the spacetime were discretized, how the initial conditions were generated, and how they were subsequently evolved over time. This makes the transparent comparison quite challenging. In this work, we perform independent static lattice simulations on the grids of $N^3 = 4096^3$ by two commonly used approaches in literature: one using the fat-string type pre-evolution to prepare for initial conditions for the physical string evolution [9, 14] and the other scheme where the field evolution occurs in the finite temperature, what we will call the thermal pre-evolution (for instance, our setup for this approach is similar to those in [10, 15]). While the fat-string pre-evolution may be criticized that it is not the same theory as the one for the physical string evolution, the direct comparison between simulations adopting different schemes should greatly help establishing the validity of the final observations or the insensitivity to the aforementioned relaxation schemes. The result in [10] has not been reported in similar presentations to [9, 14], making it difficult to be used for the meaningful comparison. The AMR technique, adopted in [15], allows to cover much longer dynamic time range than what one has ever imagined to be possible. However, whether it eventually leads us to the better determination in the region beyond the time coverage of the static lattice simulation does not seem to be straightforward. The extending our comprehensive comparison in the context of AMR will be presented in our companion paper.

The parametric behavior of the axion abundance originated from the scaling regime can be significantly affected by the nonlinearities around the QCD scale [14]. In particular, it varies depending on the value of q ($q > 1$ vs $q = 1$) and axion field values (large vs small) around the QCD scale (equivalent to the relevance of the nonlinearities) and the lower momentum cutoff (dictated by average inter-string distances). As different combinations match to different observations in literature, it should be highly useful to work out all relevant cases. Following the similar strategy to [14], we discuss the impact of the modified momentum cutoff (suggested by the scaling of the inter-string distances) and axion field values on the axion abundance, and we extend the discussion to the case with $q = 1$ to estimate the relevance of the nonlinearities around the QCD scale in that situation. This will make the comparisons between different scenarios transparent.

While there are already various string identification algorithms in literature, in this work, we propose a new novel string identification algorithm, based on the tetrahedralization of the space, which guarantees the connectedness of strings. As the name stands, the algorithm works on the tetrahedron instead of the cube. It has a few practical advantages that will be discussed below. Compared to existing techniques [21, 22, 34, 35], its performance time is comparable with them.

The most severe limiting factor of the simulation is CPU and memory resources. We have greatly optimized our own independent codes (made from the scratch) running on OpenMPI to

numerical relativity simulation and it was recently applied to cosmic strings [32].

speed up each simulation. Nevertheless, obtaining a large size of ensemble, performing at the same time all kinds of measurements such as ξ , energy budget, power spectrum, instantaneous emission, string tension, string velocity and checking out the dependencies of various prescriptions for each measurement, from the lattice simulation on the grids of 4096^3 is challenging. Therefore, we extensively used the lattice simulation on smaller scales such as 1024^3 and 2048^3 as well for numerous sanity checks and to get guideline results for an educated selection of the benchmark setups for the simulation on the bigger sized lattice of $N^3 = 4096^3$. Our final result on the axion spectrum, which supports the soft axions of the order of the Hubble scale around the QCD crossover, strongly suggests the simulation on the factor of two larger lattice space.

The paper is organized as follows. In Section 2, we introduce the model for the formation of the global axion strings. In Section 3, brief descriptions on the discretization of the equation of motion and random field configurations are given. In Section 4, a new novel string identification algorithm based on the tetrahedralization is introduced. In Section 5, we present our independent evidence for the logarithmically growing scaling solution in the number of strings in the Hubble patch. The scaling of the average inter-string distance is discussed. In Section 6, the detailed discussion on the energy budget and string properties such as the string tension and velocity are given. In Section 7, we provide our fit results on the spectral index of the power law in the axion spectrum. In Section 8, we discuss the prospect for the axion abundance for given spectral index from our simulation. In Section 9, a possible correlation between axion spectrum and string evolutions with different initial field configurations is discussed. In Appendices, all simulation details are given. Extra detailed discussions and materials are given for various subjects. Especially, the parametric behavior of the axion abundance for several distinctive situations are worked out.

Note added: while this work was being finalized, another work addressing similar aspects of axions from cosmic strings has appeared [36].

2 Formation of cosmic strings

Topological cosmic strings are generated upon the phase transition of the $U(1)_{PQ}$ symmetry by the complex scalar field ϕ in the early Universe [37–39]. The PQ symmetry breaking is conveniently parametrized by the Lagrangian,

$$\mathcal{L} = \partial_\mu \phi^* \partial^\mu \phi - \frac{m_r^2}{2f_a^2} \left(|\phi|^2 - \frac{f_a}{2} \right)^2, \quad (1)$$

where the quartic coupling corresponds to $m_r^2/(2f_a^2) \equiv \lambda$, often denoted by λ in literature, and f_a is the symmetry breaking scale. The dynamical evolution of the cosmic strings in the expanding

universe will be explored, assuming the radiation domination whose metric is given by

$$ds^2 = dt^2 - R^2(t)d\vec{x}^2 , \quad (2)$$

where \vec{x} denotes the comoving coordinates. The equation of motion from the Lagrangian in Eq. (1) in the expanding universe is given by

$$\ddot{\phi} + 3H\dot{\phi} - \frac{1}{R^2}\nabla^2\phi + \frac{m_r^2}{f_a^2}\phi \left(|\phi|^2 - \frac{f_a^2}{2} \right) = 0 , \quad (3)$$

where dot is the differentiation with respect to the cosmic time t and the gradient ∇ is evaluated in the comoving coordinate. The equation of motion in Eq. (3) admits the solitonic solution whose configuration corresponds to the topological cosmic strings. Cosmic strings formed at the PQ scale will evolve for a long dynamic time range all the way up to the QCD crossover where the abundance of the axion dark matter radiated from cosmic strings are estimated. The dynamics of the cosmic strings are traced through the evolution of the fields. As they are highly nonlinear in between largely separated two scales, the EFT approach is not available and it has to proceed through the numerical simulation on the lattice. The numerical simulation of the equation of motion in Eq. (3) on the lattice is limited since it involves three different scaling behaviors. While the lattice spacing scales as $R \propto \sqrt{t}$ in the radiation-dominated universe, the string core width m_r^{-1} stays the same and the Hubble length H^{-1} scales as $\sim t$ during the evolution. At some point, the simulation runs out of the resolution within the string core or the correlation length $\sim H^{-1}$ becomes comparable with the size of the simulation box where the boundary conditions become relevant.

The field evolution on the lattice in terms of ϕ is subject to the convergence condition, or Courant–Friedrichs–Lewy (CFL) condition, $\Delta t < R\Delta x$. This condition requires arbitrarily small time step size in the early stage of the evolution where the scale factor is small. It can be relaxed by re-expressing the equation of motion in terms of the rescaled field $\psi(\tau, \vec{x}) = R\phi(t, \vec{x})$ in the comoving spacetime coordinate. The CFL condition in this situation is relaxed to $\Delta\tau < \Delta x$. All the simulation details are given in Appendices A and B.

3 Simulation Setup

3.1 Discretization

The equation of motion in Eq. (3) is discretized in the conformal frame according to the leap-frog method whose truncation error is the order of $\mathcal{O}((\Delta x)^3)$. The lattice spacing Δx is determined by m_r for the given lattice size N . It is set to reach the maximum dynamic time range allowed by the lattice size, namely $\Delta x = \frac{m_r^{-1}}{n_c} \left(\frac{2n_c n_H}{N} \right)^{1/2}$ where n_c is the number of lattice grids inside the core and n_H is the number of Hubble patches in the simulation box at the final time. $n_c = 1$ and $n_H = 4^{1/3}$ will be our default choice in the simulation unless otherwise specified. $n_H = 4^{1/3}$

ensures at least four Hubble volumes in the simulation box at the final time. See Appendix B.1 for the detail. The time interval $\Delta\tau$ is chosen to be $\Delta\tau/\Delta x = 1/3$ so that it satisfies the CFL condition. Our simulation data set is summarized in Table 3.

3.2 Initial conditions and Relaxation

The string configurations produced out of initial conditions in the very beginning of the simulation are highly noisy. Given the limited dynamic time range of the physical string simulation, a pre-evolution for the purpose of relaxing the string network to a relatively clean level seems to be a necessary step. The relaxation step may be justified if the string network eventually approaches toward the scaling regime [40–42] and becomes insensitive to the initial configurations.

The fat-string evolution [43, 44] was adapted in recent works [9, 14] for the purpose of the relaxation (see Appendices B.2 and B.3 for details). The outcome of the fat-string pre-evolution feeds into the physical string evolution as the initial condition. It is called fat-string since the string core width is forced to scale as R during the pre-evolution so that $\frac{m_r^{-1}}{R}$ stays constant. It is implemented in the simulation by the quartic coupling scaling as R^{-2} for the fixed f_a . $R \propto t$ adopted in [14] is the convenient choice for the scale factor during the fat-string pre-evolution as it ensures the constant Hubble length with respect to the string core length which we can freely choose. The random field configurations were generated such that the Fourier amplitude $\tilde{\phi}(\vec{k})$ below the momentum cutoff $k < k_{\max} = m_r$ follows the standard normal distributions. The initial configurations are rapidly adjusted via the equation of motion in the broken phase. Similarly to [14], the pre-evolution stops when the requested number of strings per Hubble length, denoted by ξ_0 , is achieved.

Another approach is to evolve the equation of motion from the epoch right before the phase transition where the symmetry was restored (see Appendix B.5 for the detail). It is realized by adding the temperature dependent term to the potential [10, 15] (and accordingly modifying the equation of motion), $\Delta\mathcal{L} = -\frac{m_r^2}{6f_a^2}T^2|\phi|^2$ where $T^4 = f_a^4 \cdot \frac{H^2}{m_r^2} \cdot 4\zeta^2$ with $\zeta^2 = \frac{45}{2\pi^2 g_*} \frac{M_p^2 m_r^2}{f_a^4}$ and the Hubble parameter $H^2 = \frac{\pi^2}{90} g_* \frac{T^4}{M_p^2}$. The correlation length over the core size at the critical temperature $T_c (= \sqrt{3}f_a)$ is given by $\frac{m_r}{H}|_{T_c} = \frac{2}{3}\zeta$. The choice $\zeta = \frac{3}{\sqrt{2}} = 2.12123$ corresponds to the case with $H|_{T_c} = f_a$. While $\zeta \sim \mathcal{O}(1)$ ensures the order one size of the correlation length in the unit of the core length at the phase transition where cosmic strings are formed, the natural size of it is roughly $\zeta \sim 10^7$ for $g_* \sim \mathcal{O}(10^2)$, the order one size of the quartic coupling, and $f_a \sim \mathcal{O}(10^{10} \text{ GeV})$ (see Eq. (43) for the explicit expression). The order one size of ζ may correspond to the large symmetry breaking scale of $f_a \sim 10^{17} \text{ GeV}$, a large number of relativistic degrees of freedom of $g_* \sim 10^{14}$, or the combination of them for the fixed order one quartic coupling. This might be considered as a drawback of this approach. The random initial conditions for field configurations were generated, assuming the Gaussian random field configuration following the thermal distributions as in [10] in the symmetric phase. We impose the cut on the momentum $k < k_{\max} = 10m_r$ at the initial time $\tau_i = 0.1\tau_c$ (τ_c as the time at the phase transition). Since $k_{\max} \propto \tau^{-1}$, $k|_{\tau_i} \leq 10m_r$ implies $k|_{\tau_c} \leq m_r$ with the choice

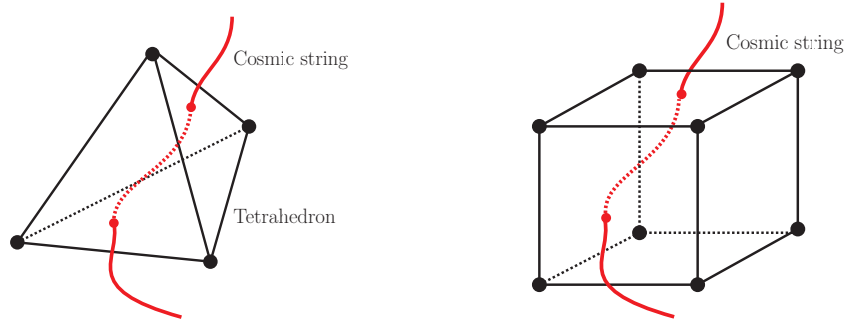


Figure 1: Illustration of a cosmic string configuration in the tetrahedron (left) and in a cube consisting of six plaquettes (right).

of $\tau_i = 0.1\tau_c$, and this looks consistent with the cut imposed in the aforementioned fat-string type relaxation. Unlike the approach exploiting the fat-string technique, the generated initial configurations smoothly transit to those of the broken phase via the equation of motion with the thermal potential naturally realizing the phase transition. More details regarding initial conditions are given in Appendix B.6.

The higher modes above m_r scale can be considered as a short distance or ultraviolet (UV) physics smaller than the string core size. Having the momentum cutoff imposed, the simulation results become insensitive to Δx or equivalently the lattice size N (for instance, see Fig. 20). Otherwise, the higher momentum modes set by a smaller Δx for a larger N kick in, the spectrum becomes more noisy, and it takes longer time to be relaxed. The impact of UV modes above m_r on initial conditions in the properties of the string network will be discussed in the Appendix C.

4 String identification on tetrahedron

A string is basically identified by examining the pattern of phases of the complex scalar fields. While there are various options for string identification algorithm, we yet introduce a new novel string identification algorithm which we find numerically very efficient and guarantees the connectedness of strings. It starts with the tetrahedralization, sub-dividing the lattice space into a series of tetrahedrons. Each tetrahedron, illustrated in the left panel of Fig. 1, has four triangular faces, and each triangular face has three vertices which we can label as $v_{i=1,2,3}$. Let us define $\theta_{123} = \theta_{12} + \theta_{23} + \theta_{31}$ where $\theta_{ij} = \arg(\phi_j \phi_i^*)$ which measures the phase difference of fields at two adjacent vertices. A string core on the triangular face is declared for the configuration with $\theta_{123} = 2\pi$ (-2π). This last statement for the string declaration can be replaced with more numerically efficient and equivalent statement, as was explained in Appendix B.7. With the assignment of $\omega_{ij} = \Re\phi_i \Im\phi_j - \Im\phi_i \Re\phi_j$ and $\omega_{123} \equiv \omega_{12} + \omega_{23} + \omega_{31}$, $\theta_{123} = 2\pi$ (-2π) can be shown to be equivalent to the case where all ω_{ij} 's are non-negative (non-positive) while ω_{123} is

positive (negative):

$$\begin{aligned}\theta_{123} = 2\pi &\leftrightarrow \omega_{ij} \geq 0 \quad \text{and} \quad \omega_{123} > 0, \\ \theta_{123} = -2\pi &\leftrightarrow \omega_{ij} \leq 0 \quad \text{and} \quad \omega_{123} < 0.\end{aligned}\tag{4}$$

The location of the string core inside the triangle r_{core} is assigned via the linear interpolation, or $r_{\text{core}} = (\omega_{23}v_1 + \omega_{31}v_2 + \omega_{12}v_3)/\omega_{123}$ such that the field value vanishes at the core. This may be considered as a leading approximation of more complete expansion in higher orders of vertices. In this prescription, the string core is strictly inside the triangle. This approach is well-defined as each tetrahedron includes either none or a pair of faces on which string cores are declared. This property also proves that strings are always connected without any discontinuity. See [21, 22, 35] for other types of string identifications that ensure the connectedness of strings. In a typical string identification, each cubic cell is associated with one volume and three faces (plaquette)². Upon tetrahedralization of the volume out of existing lattice points as vertices, each cubic cell contains 6 tetrahedrons and it is associated only with 12 triangular faces (only 4 times more). Although there are multiple choices of assigning 6 tetrahedrons, it will be interesting if this method can improve the spatial resolution out of only existing vertices. While our approach has more faces to examine, our criteria based on the signs of ω_{ij} for the string core declaration and the prescription for the string core location save computational times a lot. Overall, our approach for the string identification takes a similar amount of the computation time compared to others in literature.

5 Scaling regime

A pair of string cores found on a tetrahedron forms a line segment, and connecting them forms the cosmic string. In our simulation, the total string length in the simulation box is obtained by summing over all line segments. The average number of strings per Hubble patch is measured by

$$\xi = \frac{\ell_{\text{tot}}(L)t^2}{L^3},\tag{5}$$

where L is the size of the simulation box and $\ell_{\text{tot}}(L)$ is the total string length inside the box. The maximum dynamic time range is limited by $\log \frac{m_r}{H} \leq \log \frac{N}{n_c n_H}$. Early simulations have shown the strong hints that the cosmic string network approaches the scaling regime where the reduction of ξ due to the radiation is balanced with the enhancing ξ by more strings entering into the Hubble volume over time. Once the string network is believed to flow into the scaling regime at some point, its property will have to be insensitive to the initial configurations and the relaxation types. However, apparently the dynamic time range limited by the lattice size is not long enough to reach the asymptote that we expect it to match the scaling solution, and choosing the benchmark parameter sets for the further analyses is rather subjective. We performed a

²For n cells in the simulation box, there are total 6^n faces and each face is shared by two adjacent cells.

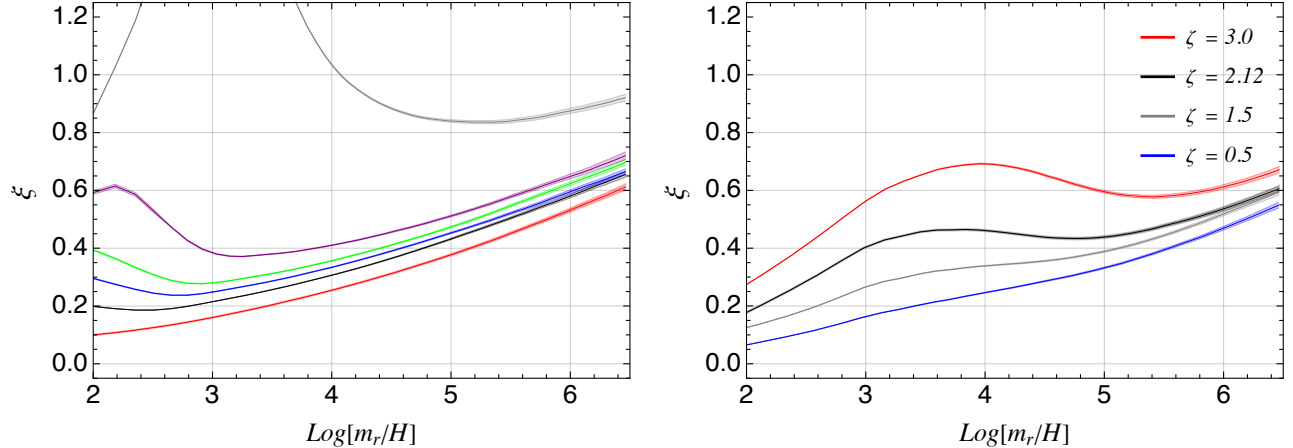


Figure 2: The evolutions of the averaged ξ in the logarithmic scales from simulations on the lattice of $N^3 = 1024^3$ with various initial conditions (distinguished by different curves within the same panel) made using fat-string pre-evolutions (left) and thermal pre-evolutions (right).

large number of simulations on the lattice of $N^3 = 1024^3$ for various initial conditions and two different relaxation schemes explained in Section 3.2, and outcomes are illustrated in Fig. 2. While the curves of ξ in the logarithmic time $\log \frac{m_r}{H}$ in Fig. 2 clearly show the strong evidence for the scaling regime (also looks consistent with the result in [9, 14]), they demonstrate that the residual dependency on initial conditions and relaxation types is not settled down within the time coverage. It takes different amounts of time to be relaxed to a relatively clean level, especially, the ξ evolution started in the finite temperature, in the right panel of Fig. 2, has relatively short time range for a reliable fit ³.

For the physical simulation whose relaxed initial conditions were prepared by the fat-string pre-evolution, following the suggestion in [14], we similarly choose $\xi_0 = 0.2$ at the initial time of the physical string simulation as our benchmark curve for the bigger-sized lattice simulation. This curve with $\xi_0 = 0.2$ can be considered in between over-generated and under-generated string networks, and thus it is hoped to be close to the scaling solution. For simulations starting right before the epoch of the phase transition in finite temperature, the curve corresponding to $\zeta = 2.12$ is chosen as our benchmark. While looking at curves in the right panel of Fig. 2, the one with $\zeta = 1.5$ may be considered to be more consistent with the selection criteria for the benchmark curve in terms of over- and under-produced string networks, $\zeta = 2.12$ can provide with more consistent comparison with the results in literature. The ξ curves for two benchmark points from the simulation on the lattice of $N^3 = 4096^3$ are illustrated in Fig. 3. While it clearly shows the strong dependency on the relaxation methods for $\log \frac{m_r}{H} < 5$ (also supported by the results in Fig. 2), ξ from two benchmarks exhibit similar scaling behaviors for $\log \frac{m_r}{H} > 5$.

If the long-term scaling behavior is assumed to be characterized by the single linear loga-

³We empirically observe that the curves with this type of the relaxation requires a larger ensemble size for the smooth curves than the case with the fat-string pre-evolution.

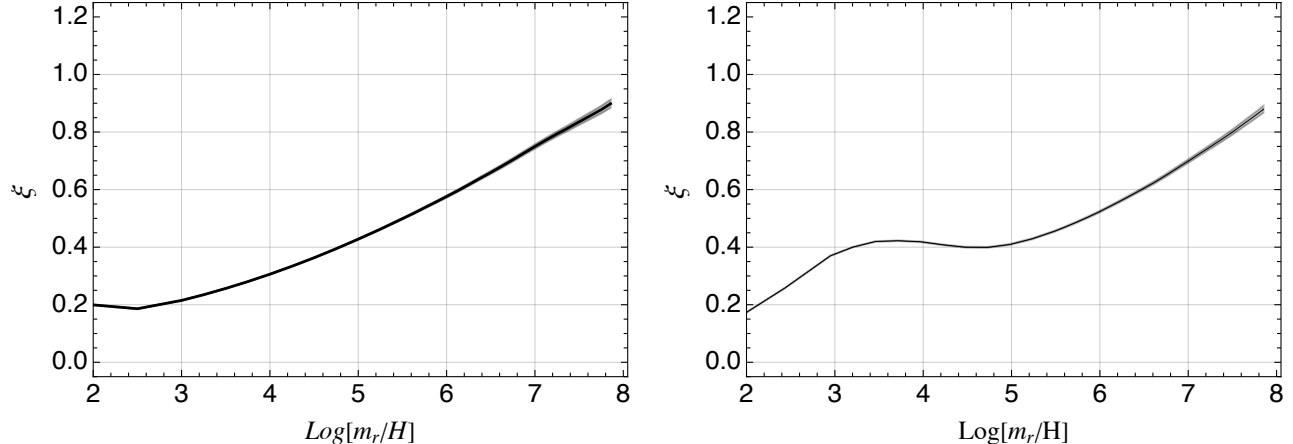


Figure 3: The evolutions of the averaged ξ in the logarithmic scales from simulations on the lattice of $N^3 = 4096^3$ for two relaxations whose initial conditions were prepared using fat-string pre-evolutions (left) and thermal pre-evolutions (right). The width of each curve represents the statistical errors.

rithmic term to which all trajectories with different initial conditions are attracted over time, deviations from the linear term in early times may be parametrized in terms of various mixtures of \log^{-n} ($n \geq 1$) terms. We fit the ξ curves with the ansatz including up to \log^{-2} [14],

$$\xi = \frac{d_2}{\log^2 \frac{m_r}{H}} + \frac{d_1}{\log \frac{m_r}{H}} + c_0 + c_1 \log \frac{m_r}{H} . \quad (6)$$

We refer this to global log-scaling hypothesis. Along this line of reasoning, all curves are fitted together by taking c_0 and c_1 as the global parameters while taking d_1 and d_2 as local ones which are specific to each curve. Variations of c_0 and c_1 when adding \log^{-3} as well to Eq. (6) or when changing the fit interval (two choices, $\log \geq 4.5$ and $\log \geq 5$ are selected) may be taken as the part of the systematic error. The detail of the fit procedure is presented in Appendix C.1. While we find that fitted curves are sensitive to both fit ansatz and range used for the fit, our results from the fit over the range $\log > 5$ are presented in Table 1⁴.

Pre-evolution type	Fit with global log-scaling hypothesis	Interval for fit
Fat-string	$\xi \sim -0.81 + 0.21 \log \frac{m_r}{H}$	$\log \frac{m_r}{H} = [5.0, -]$
Thermal	$\xi \sim -1.15 + 0.26 \log \frac{m_r}{H}$	$\log \frac{m_r}{H} = [5.0, -]$

Table 1: The fitted curve taking the global log-hypothesis from two benchmark simulations differing by the relaxation schemes. The combined data from simulations on the grids of $N^3 = 1024^3$ and 4096^3 (results in Figs. 2 and 3) were used in the fit.

⁴Enlarging the interval to $\log > 4.5$ gives $c_1 = 0.26$, and including \log^{-3} term, while keeping the same interval of $\log > 5$, leads to $c_1 = 0.23$ for the simulation with the fat-string pre-evolution. As the scaling regime occurs at a bit later times in the simulation using the thermal pre-evolution, a similar exercise may not be meaningful.

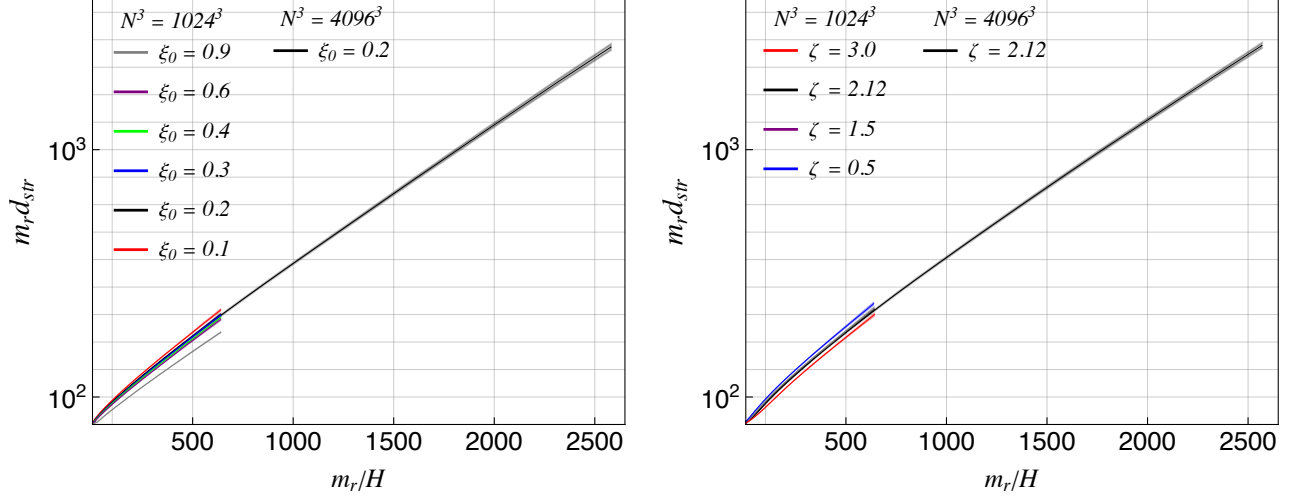


Figure 4: The evolutions of the averaged $m_r d_{\text{str}}$. from simulations on the lattice of $N^3 = 1024^3$ and 4096^3 . Initial conditions were prepared using fat-string pre-evolutions (left) and thermal pre-evolutions (right). The width of each curve represents the statistical errors.

5.1 Scaling of inter-string distances

The average inter-string distance can be measured by $d_{\text{str.}} = (L^3/\ell_{\text{tot}}(L))^{1/2}$. Using the definition for ξ in Eq. (5), the inter-string distance is expected to scale like $d_{\text{str.}} = 1/(2H\sqrt{\xi})$. Taking the log-scaling hypothesis, the simulation data is equivalently fitted with $d_{\text{str.}} = t/\sqrt{\xi}$ where ξ is given by Eq. (6), and $d_{\text{str.}} \propto t/\sqrt{\log t}$ is expected at late times. On contrary, the scenario favoring the constant scaling of ξ at late times is realized as the linear scaling in time for the inter-string distances, or $d_{\text{str.}} \propto x_* t$ with the constant x_* . If the long-term behavior of $d_{\text{str.}}$ is assumed to be attracted to a global linear term in time t , possible deviations from the linear term in early times may be accounted by extra time-dependent terms. We refer this to global constant-scaling hypothesis as it implies that $\xi = 1/(4H^2 d_{\text{str.}}^2)$ asymptotes to a constant. The evolution of $d_{\text{str.}}$ in the m_r^{-1} unit is illustrated in Fig. 4. As is evident in Fig. 4, the curves of $d_{\text{str.}}$ from different initial conditions do not look possible for them to be attracted toward the single linear term in t at late times. While fitting by taking all parameters as local ones for each curve can be carried out, it looks challenging to distinguish between the log-scaling and constant-scaling hypotheses since the evolution of $d_{\text{str.}}$ at late times is dominated by the t term. Instead, the quantity $2Hd_{\text{str.}}$, measured by evaluating $2H(L^3/\ell_{\text{tot}}(L))^{1/2}$, may be better choice to isolate the scaling behavior of the slope of $d_{\text{str.}}$ itself, or $1/\sqrt{\xi}$. Its evolution is illustrated in Fig. 5. Although $m_r d_{\text{str.}}$ at late times looks like following almost straight lines in time t , the asymptote behavior of $2Hd_{\text{str.}}$ in Fig. 5 does not support the constant scaling behavior (as it should be obvious from our observed logarithmic growth behavior of ξ).

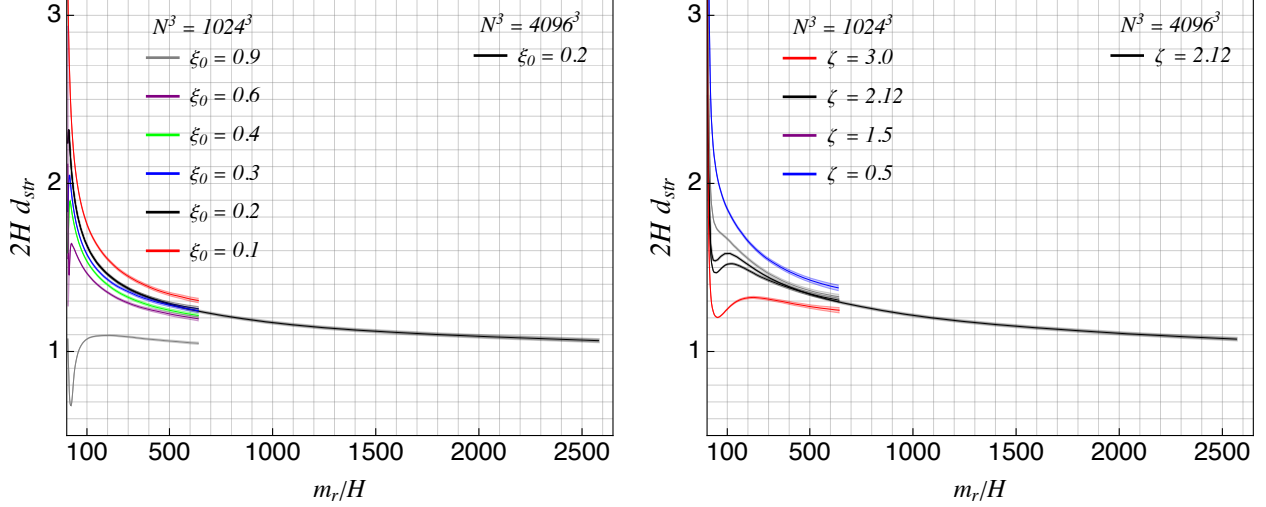


Figure 5: The evolutions of the averaged $2Hd_{\text{str}}$ from simulations on the lattice of $N^3 = 1024^3$ and 4096^3 for relaxations. Initial conditions were prepared using fat-string pre-evolutions (left) and thermal pre-evolutions (right). The width of each curve represents the statistical errors.

6 Cosmological evolution of string network

6.1 Energy density

The cosmological evolutions of the energy densities of individual components, namely axions, radial modes, and strings, demonstrate the interplay among those over time, and provide the dynamic picture of how the string network approaches the scaling regime. The total Hamiltonian density of the PQ field ϕ is given by $T_{00} = \dot{\phi}^* \dot{\phi} + \frac{1}{R^2} \nabla \phi^* \cdot \nabla \phi + V$ where ∇ is the gradient with respect to the comoving coordinate. It can be expressed explicitly in terms of the radial mode r , axion mode a , and their interactions,

$$T_{00} = \frac{1}{2} \left(1 + \frac{r}{f_a} \right)^2 \left(\dot{a}^2 + \frac{1}{R^2} |\nabla a|^2 \right) + \frac{1}{2} \left(\dot{r}^2 + \frac{1}{R^2} |\nabla r|^2 \right) + V. \quad (7)$$

The total energy density is the spatial average of the total Hamiltonian $\rho_{\text{tot}} = \langle T_{00} \rangle$ over the physical coordinates. The energy densities of axions and radial modes are measured by evaluating

$$\begin{aligned} \rho_a &= 2 \times \left\langle \frac{1}{2} \dot{a}^2 \right\rangle, \\ \rho_r &= \left\langle \frac{1}{2} \left(\dot{r}^2 + \frac{1}{R^2} |\nabla r|^2 \right) + V \right\rangle, \end{aligned} \quad (8)$$

where fields are properly masked according to the prescription described in Appendix B.8 to screen off the effect from string cores. Assuming that the total energy density of the PQ field is

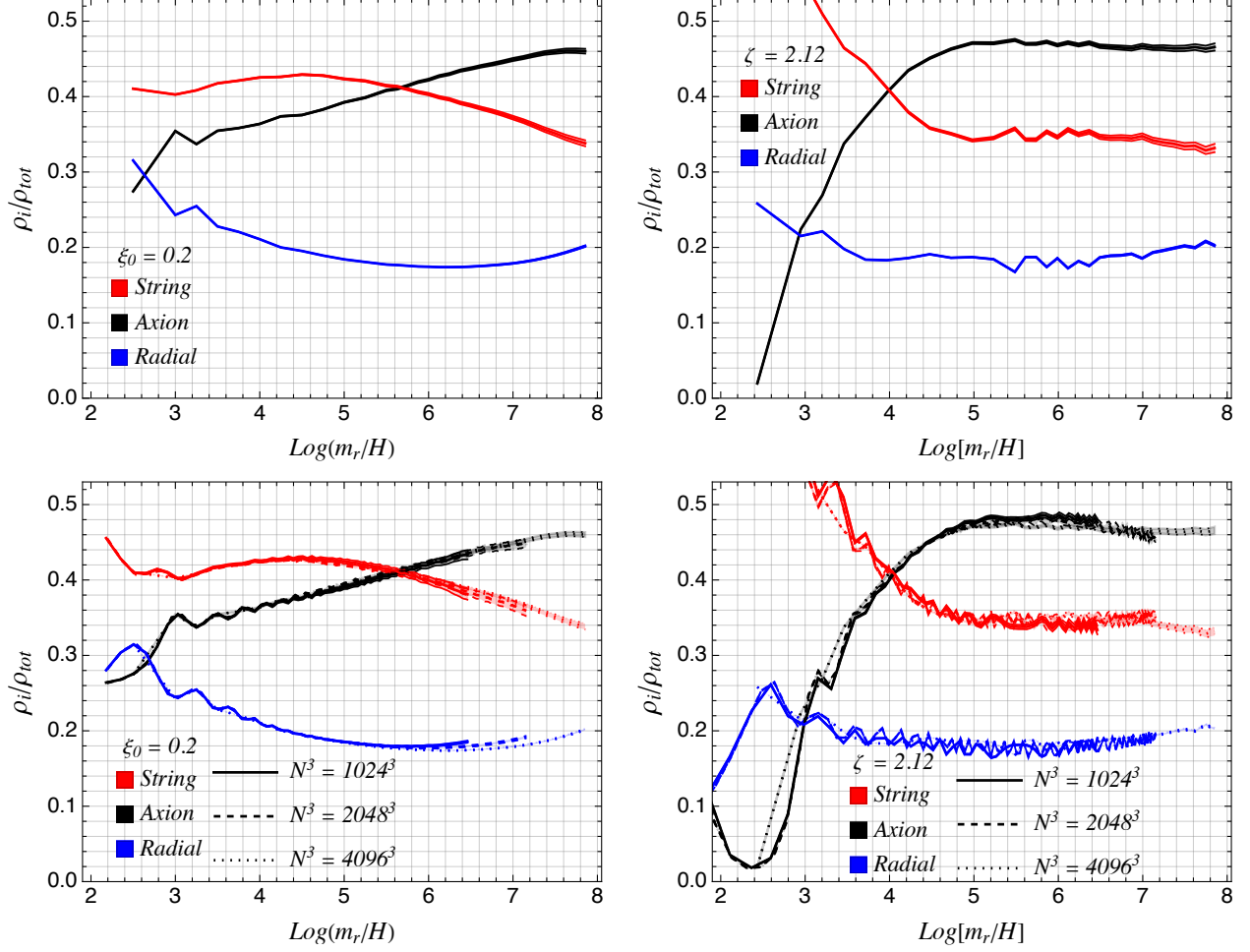


Figure 6: Energy budgets of axions, radial modes, and strings from the simulations with $N^3 = 4096^3$ (top) and also with smaller lattice size (bottom) whose initial data was relaxed by the fat-string pre-evolution (left) and thermal pre-evolution (right).

conserved, the energy density of strings is extracted by subtracting ρ_a and ρ_r in Eq. (8) from the total energy density, $\rho_s = \rho_{\text{tot}} - \rho_a - \rho_r$. The gradient of axions in Eq. (7) mainly contributes to the string tension and it is taken as part of the string energy density.

Energy densities of individual components for two different simulation setups are illustrated in Fig. 6. In the region before the string network enters the scaling regime, the separation between different components should be ambiguous, and their physical meanings become more transparent at late times. Contrary to similar scaling behaviors in ξ curves in Fig. 3 for $\log \frac{m_r}{H} > 5$ for both types of pre-evolutions, the apparent evolution of the energy density for each component look dramatically different. Nevertheless, all energy densities for axions, strings, and radial modes near the end of simulation amazingly agree well. Since two simulations in Fig. 6 differ by the way the initial field configurations were generated and subsequent relaxation schemes, the distinctive behaviors until late times may indicate a source of a large systematic errors

or an ambiguity in selecting the would-be attractor solution. Unlike the energy budget in [9] where the different prescription for the fat-string pre-evolution was used ⁵, the contributions from strings and axions in our simulation cross around $\log \sim 5.5$, as is seen in the left panels of Fig. 6, and the axion-to-string energy density ratio seems to follow the expectation in the scaling regime, $\rho_a/\rho_s \sim \log \frac{m_r}{H}$. The contribution from radial modes is supposed to decrease at late times whereas ρ_r in Fig. 6 shows the arising behavior around $\log \frac{m_r}{H} \sim 6$ in both benchmark simulations. The similar observation was made in [14] except that the overall rate is smaller, for instance, $\rho_r \sim 20\%$ in the scaling regime in Fig. 6 versus $\sim 14\%$ in [14]. The latter [14] compares better with our simulation with $\xi_0 \sim 0.1$ as is indicated in the left of Fig. 21 in Appendix C.2.1 where the radial modes appear taking roughly 14% of the total energy density. However, the crossing point between strings and axions for the case with $\xi_0 = 0.1$ is delayed to more late times, around $\log \frac{m_r}{H} \sim 6.5$. The bottom-left panel of Fig. 6 overlays three simulation results only differing by the lattice size which equivalently can be taken to extract the dependency on the lattice spacing in the string core length unit $m_r \Delta$ ⁶, and it strongly indicates that the arising behavior after around $\log \frac{m_r}{H} \sim 6$ could be an artifact due to the finite size of the lattice spacing. A similar conclusion from the simulation using the thermal pre-evolution is rather difficult due to undamped noises as is evident in the bottom-right panel of Fig. 6.

In the right panels of Fig. 6, the energy budget from simulations using thermal pre-evolution is presented in a similar manner. While energy densities from the simulation with $N^3 = 4096^3$ was coarsely recorded starting only from $\log \frac{m_r}{H} \sim 2.3$ to save the computational time, more dense time samplings starting from earlier times were selected to record the data in the simulations with smaller lattice sizes. While the bottom-right panel of Fig. 6 shows apparently different evolution patterns of axions and strings compared to those using fat-string pre-evolution, the energy budgets of two simulations using the fat-string and thermal pre-evolutions amazingly agree well at the final time, $\log \frac{m_r}{H} \sim 7.8$, as was mentioned above. This agreement may justify the choice of two benchmark simulations on the lattice with $N^3 = 4096^3$. The analogous dependency on the lattice spacing $m_r \Delta$ does not have a clear pattern, for instance, the slightly decreasing ρ_a (and slightly increasing ρ_s) near their final times in simulations with $N^3 = 1024^3$, 2048^3 is flipped when the dynamic time range is extended with the bigger lattice size. The overall relaxation in the simulation using the thermal pre-evolution seems to take longer dynamic time and is subject to the larger uncertainty than the case using the fat-string pre-evolution.

6.2 String tension and boost factor

The total energy stored in strings E_s is given by $E_s = \mu_{\text{eff}} \ell_{\text{tot}}(L)$ where μ_{eff} is an effective tension and $\ell_{\text{tot}}(L)$ is the total string length in the simulation box of size L . The effective tension can be extracted from measurements of ξ and the string energy density $\rho_s = E_s/L^3$. That is, using

⁵The simulation in [9] implements the fat-string pre-evolution with the scale factor scaling as $R \propto \sqrt{t}$ whereas, in our prescription, the scale factor $R \propto t$ as in [14] is used during the pre-evolution.

⁶Since the bigger lattice size N is associated with the smaller lattice spacing Δ , increasing N is equivalent to taking the continuum limit from the smaller-sized-lattice point of view at a fixed time.

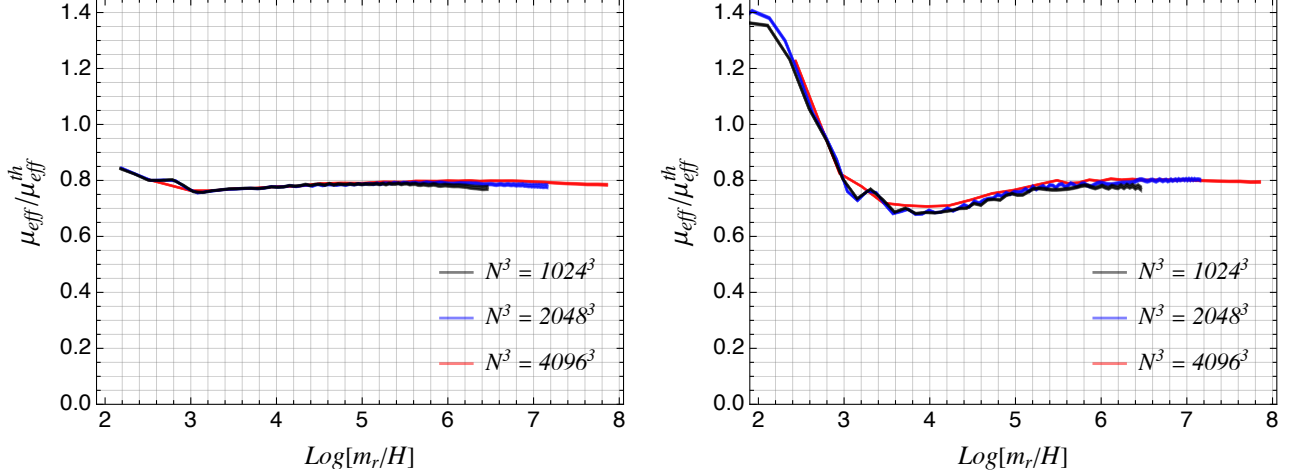


Figure 7: The cosmological evolution of the string tension with respect to the theory expectation from two benchmark simulations whose initial field configurations were prepared by fat-string pre-evolution (left) and thermal pre-evolution (right).

the relation in Eq. (5), μ_{eff} can be expressed as

$$\mu_{\text{eff}} = \frac{E_s}{\ell_{\text{tot}}(L)} = \rho_s \frac{t^2}{\xi}, \quad (9)$$

or the energy density of strings is given by

$$\rho_s = \mu_{\text{eff}} \frac{\xi}{t^2}. \quad (10)$$

The string tension of the global strings in Eq. (9) is logarithmically divergent. Its divergence is cut off by the UV cutoff, r_{UV} , roughly string core length m_r^{-1} , and the inter-string distance, which is roughly $(L^3/\ell_{\text{tot}}(L))^{1/2}$, and it leads to the form that suits well for the straight string [34],

$$\mu_{\text{eff}}^{\text{th}} = \langle \gamma \rangle \mu_0 \log \frac{(L^3/\ell_{\text{tot}}(L))^{1/2}}{r_{\text{UV}}} = \langle \gamma \rangle \mu_0 \log \frac{1}{2r_{\text{UV}} H \xi^{1/2}}, \quad (11)$$

where $\langle \gamma \rangle$ is the averaged (over the length) boost factor of string velocity, and μ_0 denotes the proportionality factor. On contrary, the logarithmic divergence is absent in the local strings [24, 41, 42, 44, 45] due to the compensating contribution from the gauge fields. The logarithmic dependence on distances in global strings indicates the long-range force mediated by massless axions between strings. However, as the coupling of large wavelength axions with strings scales as $1/\log(m_r/H)$ [46], the string network at late times is expected to become similar to the situation of the local strings. By comparing the measured effective string tension in Eq. (9) against the theoretical expectation in Eq. (11), the non-trivial scaling property of the string energy density can be checked. The effective tension μ_{eff} with respect to $\mu_{\text{eff}}^{\text{th}}$ is illustrated in

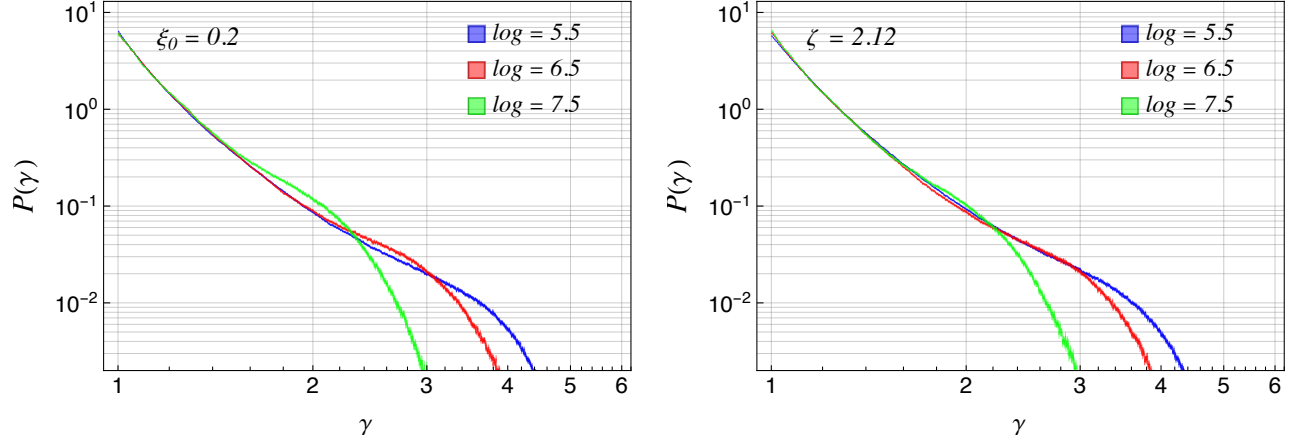


Figure 8: The probabilistic distribution $P(\gamma)$ of the boost factor γ from two benchmark simulations on the grid with $N^3 = 4096^3$.

Fig. 7 where $\mu_{\text{eff}}^{\text{th}}$ is given by Eq. (11) with $\langle\gamma\rangle\mu_0 = \pi f_a^2$ and $r_{\text{UV}} = m_r^{-1}(4\pi)^{1/2}/2$ [14]. As is evident in Fig. 7, the effective string tension-to-theoretical expectation ratio is relaxed to the roughly constant value at later times, and it implies that the expression in Eq. (11) is intriguingly applicable to more generic configurations. Approaching the scaling regime looks more dramatic in the simulation with the thermal pre-evolution as is seen in the right panel of Fig. 7.

The time variation of $\mu_{\text{eff}}^{\text{th}}$ in Eq. (11) is given by

$$\dot{\mu}_{\text{eff}}^{\text{th}} = \frac{\langle\dot{\gamma}\rangle}{\langle\gamma\rangle}\mu_{\text{eff}}^{\text{th}} + \langle\gamma\rangle\mu_0 \left(\frac{1}{t} - \frac{\dot{\xi}}{2\xi} \right). \quad (12)$$

If the averaged boost factor $\langle\gamma\rangle$ approaches the scaling regime, the prefactor $\langle\gamma\rangle\mu_0$ in Eq. (11) is expected to behave like

$$\langle\gamma\rangle\mu_0 = \mu_{\text{eff}}^{\text{th}} \left(\frac{1}{t} - \frac{\dot{\xi}}{2\xi} \right)^{-1}, \quad (13)$$

which can be explicitly checked from lattice simulations. The average boost factor is obtained by evaluating

$$\langle\gamma\rangle = \int_1^\infty \gamma P(\gamma) d\gamma = \int_1^\infty \gamma \frac{1}{\xi} \frac{d\xi_\gamma}{d\gamma} d\gamma, \quad (14)$$

where ξ_γ is the fraction of ξ with the boost factor below γ . The Lorentz boost factor γ of the string core is computed from field configurations through the relation $\gamma^2 - 1 = \beta^{-2}|\dot{\phi}|^2$ evaluated at every string core. Recall that, in our tetrahedron-based string identification method, a pair of string core locations are assigned via the linear interpolation from field values at three vertices on each triangular face. Similarly for $\dot{\phi}$ at the string core. The corresponding tetrahedron includes string line segment (if exists), and the string boost factor γ is evaluated at the mid-point of

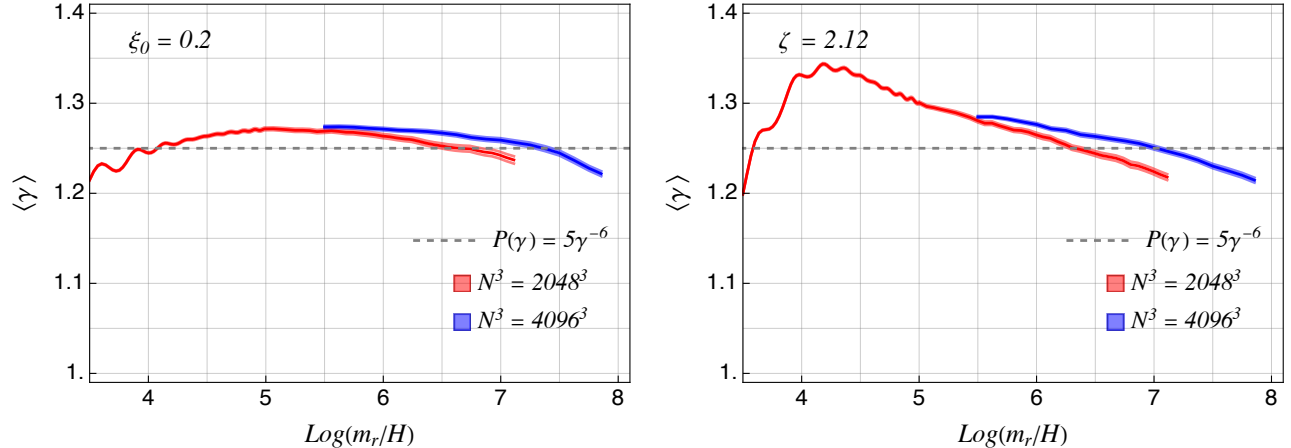


Figure 9: The averaged boost factor $\langle \gamma \rangle$ from two benchmark simulations on grids with $N^3 = 2048^3$ and 4096^3 .

the string line segment. The probability distribution $P(\gamma)$ of the boost factor is illustrated in Fig. 8. $P(\gamma)$ roughly scales like $\sim \gamma^{-6}$ as was also observed in [14]. Finally, the time variation of the averaged boost factor is illustrated in Fig. 9. To save the computational time, the boost factors were computed only at the coarsely selected sampling points. In the simulation with the lattice size of $N^3 = 4096^3$, only time slices after $\log \sim 5.5$ were picked. The earlier times were covered by the simulation on the smaller lattice of $N^3 = 2048^3$ with the small overlap with those from the former. The overall qualitative behavior and averaged boost factor $\langle \gamma \rangle = 1.2 \div 1.3$ agrees well with the result in [14] as is seen in the left panel of Fig. 9. On contrary, the early time behavior appears pronouncedly different for the cosmic strings in the simulation using the thermal pre-evolution although both become similar at late times. The gray dashed lines in both panels in Fig. 9 represent the expectation from the ansatz $P(\gamma) = 5\gamma^{-6}$. Two curves from simulations differing by the lattice sizes, at an instant time, can be effectively thought of as two cases differing by $m_r \Delta$, for instance, $m_r \Delta$ of the red curve at a fixed time within $\log = [5.5, 7]$ will be larger than that of the blue curve which is closer to the continuum limit.

7 Axion spectrum

The strings lose their energy into axions and radial modes, denoted by Γ . Individual transfer rates into axions and radial modes are represented by Γ_a and Γ_r , respectively, and $\Gamma = \Gamma_a + \Gamma_r$. Similarly to [9], our simulation confirms that strings mostly decay into axions with small fraction to radial modes, namely $\Gamma \sim \Gamma_a$, as is illustrated in Fig. 10. The fluctuating evolution of r_a from the simulation using the thermal pre-evolution (red solid line in Fig. 10) is due to the oscillatory behavior in the energy budget as was illustrated in the right panels in Fig. 6. The evolution of

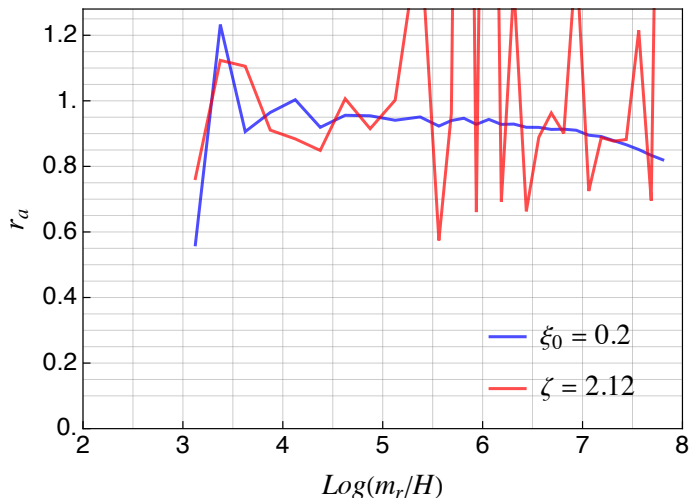


Figure 10: Fraction of the transfer rate from strings to axions, $r_a = \Gamma_a/(\Gamma_a + \Gamma_r)$, from two benchmark simulations using the fat-string ($\xi_0 = 0.2$) and thermal pre-evolutions ($\zeta = 2.12$).

the relativistic axion energy density follows the equation

$$\frac{1}{R^4(t)} \frac{\partial}{\partial t} (R^4(t) \rho_a(t)) = \Gamma_a + \dots \quad (15)$$

where \dots corresponds to the effect from the interaction between axions and radial modes. Similarly for the radial energy density except that it scales like matter. Assuming that Γ_a eventually dominates at late times, $\Gamma \sim \Gamma_a$, in the evolution of ρ_a , the axion energy density can be expressed as the integration of the transfer rate,

$$\rho_a(t) = \int^t dt' \left(\frac{R(t')}{R(t)} \right)^4 \Gamma(t'). \quad (16)$$

The inclusive axion energy density does not tell about the characteristic hardness or softness of the axions radiated from strings, and it is more informative to look into the differential distribution of the axion energy density in momentum $\partial\rho_a/\partial k$, defined by $\rho_a = \int dk (\partial\rho_a/\partial k)$. In the absence of no new scales roughly between m_r and H , the existence of the scaling regime indicates the power law fall-off behavior, $\sim k^{-q}$. The characteristic feature of the axion spectrum falls into roughly three categories depending on the value of q [9]. When $q > 1$ [26, 27, 47, 48], the spectrum is more pronouncedly peaked near the order of Hubble which implies that the spectrum is IR-dominated and axions radiated from strings are soft. On contrary, when $q < 1$, the axion spectrum is relatively suppressed near the Hubble scale and more pronounced near the string core scale. Axions in this category are supposed to be hard and the spectrum is UV-dominated. The situation with $q = 1$ [49, 50] is in between the above two cases.

The distributions of the differential axion energy density, divided by $H f_a^2$ to cancel the overall time dependence, in two different simulation setups, differing by the relaxation scheme, on the

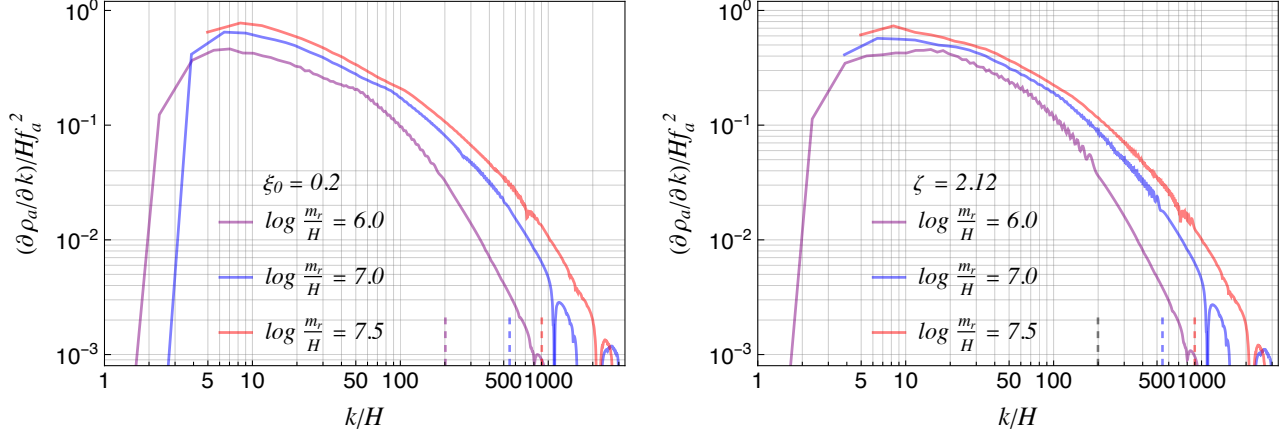


Figure 11: The spectral axion energy density from simulations with $N^3 = 4096^3$ for two benchmark points. Dashed lines represent $m_r/(2H)$ for three choices of time snapshots.

lattice with $N^3 = 4096^3$ are illustrated in Fig. 11 at three instant times, $\log = 6$ (purple), 7 (blue), 7.5 (red), respectively. The positions of $m_r/(2H)$, where the parametric resonances are expected, are also presented by dashed lines with the same color coding. The shape of $\partial\rho_a/\partial k$ at each instant time in Fig. 11 nicely captures the power law fall-off scaling behavior between two scales m_r and H , and the distributions rapidly drop off at the momentum below the Hubble scale H and above the string core scale m_r as is expected. Specifically, from the curves in Fig. 11, the peaks in IR region are located at $k/H \sim 5 \div 10$ and the drop-offs in UV occur around $m_r/(2H)$.

From the transfer rate from strings to axions in the differential form $\Gamma(t) = \int dk (\partial\Gamma(t)/\partial k)$, assuming $\Gamma \sim \Gamma_a$, the normalized instantaneous emission function F can be defined as

$$1 = \int \frac{dk}{H(t)} \frac{H(t)}{\Gamma(t)} \frac{\partial\Gamma}{\partial k}(k, t) \equiv \int dx F[x, y], \quad (17)$$

where $x = k/H$ and $y = m_r/H$. The instantaneous emission F is nothing but the normalized differential transfer rate measured in k/H , and it characterizes the distribution of the axion spectrum in momentum, contributing to the axion energy density in Eq. (16). With the choice of k/H , the peak location at order of the Hubble remains constant. In the simulation, F is measured from the axion spectral energy density $\partial\rho_a/\partial k$,

$$F \left[\frac{k}{H}, \frac{m_r}{H} \right] = \frac{1}{\Gamma_a/H} \frac{1}{R^3} \frac{\partial}{\partial t} \left(R^3 \frac{\partial\rho_a}{\partial k} \right), \quad (18)$$

by taking two time slices of the data, for instance, separated by $\log \frac{m_r}{H} = 0.25$ as our default choice. The time intervals used for the instantaneous emission spectrum differ in literature, and its dependency on the time interval is discussed in Appendix D.1 in detail. The instantaneous emission F from our simulations on the lattice of $N^3 = 4096^3$ for two simulation setups are

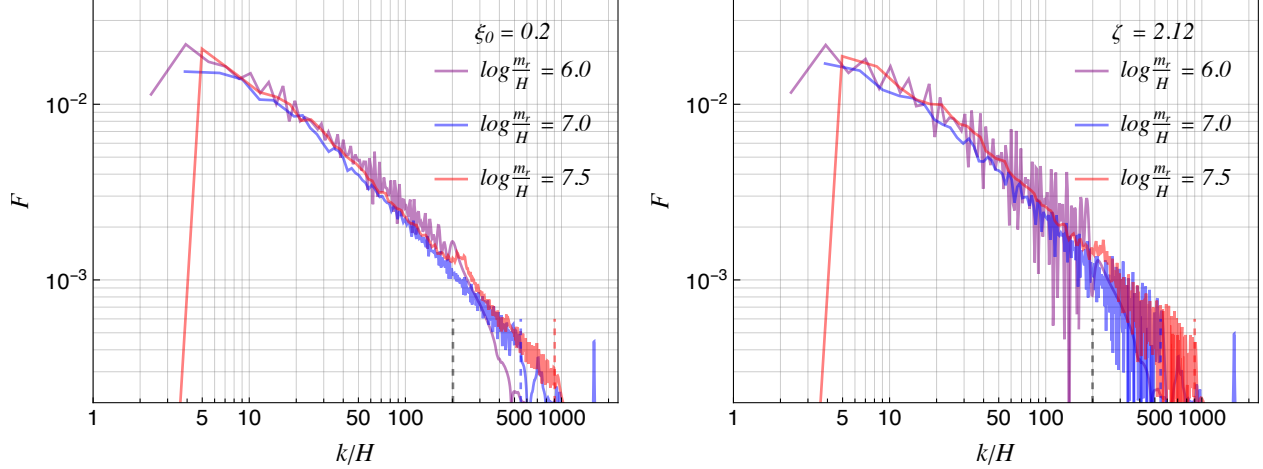


Figure 12: The spontaneous emission F from simulations on the lattice of $N^3 = 4096^3$ for $\xi_0 = 0.2$ (left) and $\zeta = 2.12$ (right) at three instant times snapshots, $\log \frac{m_r}{H} = 6, 7, 7.5$. Dashed vertical bars with the same color coding correspond to $m_r/(2H)$ at each time instant.

illustrated in Fig. 12 for three logarithmic time slices, $\log = 6, 7, 7.5$. While the overall shapes in both panels of Fig. 12 are similar, the emission spectra using the thermal pre-evolution are more noisy although they become cleaner at late times.

7.1 Power law scaling

The power law fall-off behavior of $F \propto k^{-q}$ between m_r and H is the most crucial part of the cosmic string network for the plausibility of the axion as the dark matter candidate. The precise determination of the spectral index q will allow us to estimate the relic abundance of axions. To avoid contaminations from the UV and Infrared (IR) regions, the fit needs to be done inside an appropriate interval away from the string core and Hubble scales, or parametrized as $k = [x_{\text{IR}}H, m_r/x_{\text{UV}}]$. Since there is no obvious choice for the interval for fitting F and it rather depends on the situation, we fit the power law fall-off region for various choices of $x_{\text{UV}}, x_{\text{IR}}$ to screen off UV and IR contaminations. It is instructive to estimate the number of sampling points within the interval for given $x_{\text{IR}}, x_{\text{UV}}$, and the lattice size N . The physical momentum on the lattice is $\vec{k} = \frac{2\pi}{RN\Delta x} \vec{n}_k$ where the index runs up to $\frac{N}{2}$ ⁷, and in the Hubble unit, $x = k/H = \frac{2^{3/2}\pi}{N(\Delta x m_r)} \sqrt{y} n_k$. The number of sampling points used for the fit within the interval $x_{\text{IR}} \leq x \leq y/x_{\text{UV}}$ for the static lattice simulation, using Δx in Eq. (29), is given by

$$N_{\text{fit}} = \frac{\text{Interval of } x}{x\text{-spacing}} = \frac{1}{2^{3/2}\pi} \left(\frac{\sqrt{y}}{x_{\text{UV}}} - \frac{x_{\text{IR}}}{\sqrt{y}} \right) \left(\frac{2n_H N}{n_c} \right)^{1/2}. \quad (19)$$

As is illustrated in Fig. 13 for various intervals, the number of sampling points increases with

⁷It should be distinguished from the physical momentum k truncated at m_r when generating initial conditions for scalar fields. The maximum momentum set by the lattice spacing is $k_{\text{max}} = \frac{2\pi}{R(2\Delta x)}$.

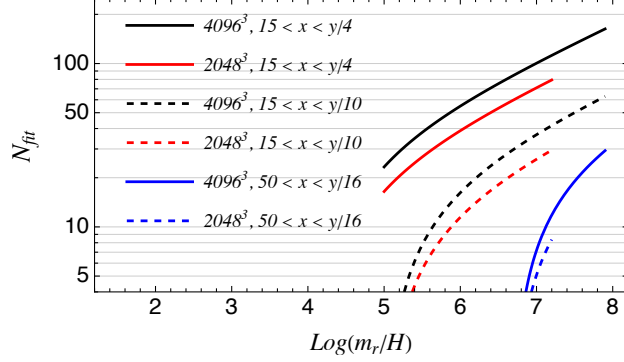


Figure 13: The number of sampling points inside $x_{\text{IR}} \leq x \leq \frac{y}{x_{\text{UV}}}$ for fitting the power law for the lattice size of 2048^3 and 4096^3 . $n_c = 1$, $n_H = 4^{1/3}$ were used. Curves are plotted from 5 to the maximal time coverage $\sim \log \frac{N}{n_c n_H}$.

the increasing time. It is because the spacing of x scales as $\sim \sqrt{y}$ with the time whereas the upper end of the interval scales as $\sim y$ for the fixed lower end value. At later times, both higher and lower k modes previously staying outside the interval enter into the interval. In terms of k scaling as $\sim R^{-1}$, the lower end of the interval $\sim H$ decreases faster than R^{-1} and more lower k modes enter into the interval. More higher modes from above the m_r scale get redshifted below m_r and part of them may also enter into the interval. As is evident in Fig. 13, the lattice size of $N^3 = 2048^3$ seems to be enough for the loose interval, $15 \leq x \leq \frac{y}{4}$, adopted in [14], and not enough for the tight interval, $40 \leq x \leq \frac{y}{16}$ adopted in [15]⁸.

The modes above m_r at the phase transition correspond to the short distance physics above the PQ symmetry breaking scale. At later times, those UV modes such as radial modes are redshifted and can enter the interval. Requiring no contamination from those redshifted UV modes sets the upper bound on the \log_i , or $\frac{y}{x_{\text{UV}}} \leq \frac{m_r}{HR}$ which leads to $\log_i \leq 2 \log[\sqrt{2} x_{\text{UV}}]$. $\log_i \leq 6.2$ (3.47) for $x_{\text{UV}} = 16$ (4). There will be an unavoidable contamination unless the radial modes get decayed away before reaching the scaling regime. Matching this upper limit to the maximal time coverage set by the lattice size leads to $x_{\text{UV}} = \sqrt{N/(2n_c n_H)}$. Assuming $n_c = 1$ and $n_H = 4^{1/3}$, x_{UV} needs to be set to $x_{\text{UV}} = 25.4$ for $N^3 = 2048^3$ and $x_{\text{UV}} = 35.9$ for $N^3 = 4096^3$. Applying this tight UV cutoff will make extracting the power law fall-off behavior challenging due to the limited sampling points. However, upon generating the initial conditions for scalar fields, only momentum modes below m_r were populated. Although higher momentum

⁸When using AMR, assuming the locally refined region around string cores are completely masked for simplicity, the lattice spacing which is relevant for the power spectrum analysis will be similar to the static case except for the modified lattice spacing in Eq. (32). However, as the simulation time extends over beyond the coverage for the static simulation, more momentum modes enter into the interval of x , increasing N_{fit} . One limitation in this situation with AMR will be that the upper end of the interval should be smaller than the maximally allowed x set by Δx , or $\frac{y}{x_{\text{UV}}} \leq x_{\text{max}}$ where $x_{\text{max}} = \frac{\pi}{HR\Delta x} = \pi \sqrt{\frac{n_c N}{2^k n_H}} y$, and it gives the upper limit on $\log_i \leq \log[x_{\text{UV}}^2 \pi^2 (n_c/2^k) \frac{N}{n_H}]$. For the simulations with $N^3 = 2048^3$, $n_c = 4$, $k = 4$, and $n_H = 4^{1/3}$, the limit on the time coverage is estimated to be $\log_i \leq 10.8$ for $x_{\text{UV}} = 4$ and $\log_i \leq 13.6$ for $x_{\text{UV}} = 16$.

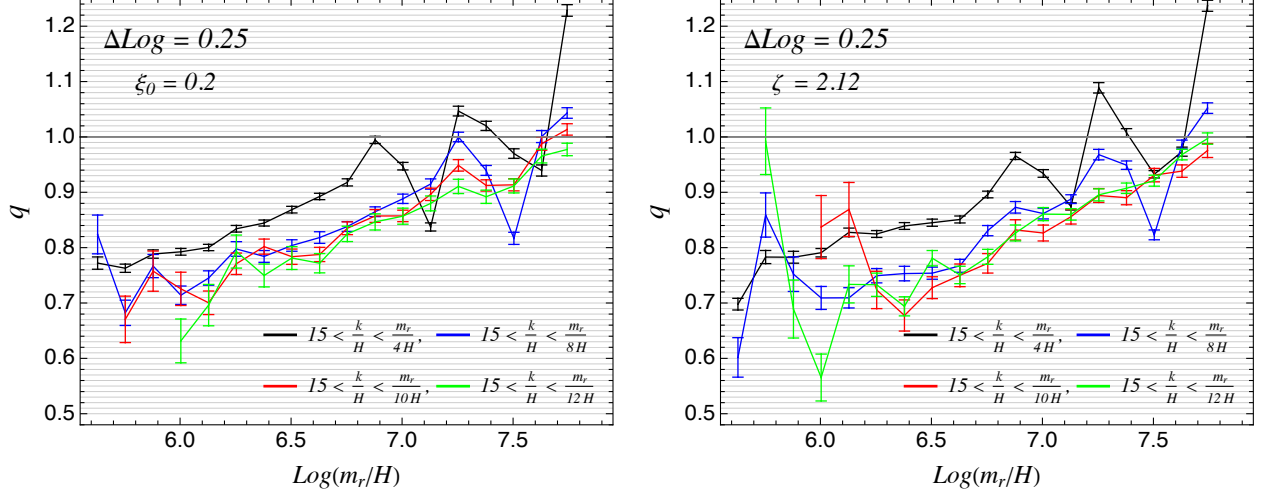


Figure 14: The spectral index q of the instantaneous emission F fitted in the interval with the varying x_{UV} while $x_{IR} = 15$. The error bars are statistical.

modes are generated via the equation of motion, they do not look as harm as those originally generated at the generation of the random field configurations.

The results from our simulations following the fit prescription explained in Appendix D.1 are illustrated in Figs. 14 and 15 for our default choice of $\Delta \log = 0.25$ (see Figs. 25 and 26 for different choices of $\Delta \log$). We observe the similar logarithmic growth to those in [14] except that our result shows a bit steeper slope than that in [14], for instance, the value of q reaches unity within the dynamic time range of the simulation for a similar choice of the interval. It will be interesting to see how q further evolves beyond the time coverage of our current simulation, and this justifies improving the lattice resolution by the factor of two, namely $N^3 = 8192^3$. In Fig. 14, the UV cutoff is varied while IR cutoff x_{IR} is fixed to 15. In Fig. 15, the IR cutoff is varied while UV cutoff x_{UV} is fixed to 10. The error bars in all curves represent the statistical ones over 100 independent simulation runs. Interestingly, the patterns of central values at late times look similar irrespective of types of pre-evolutions. We suspect that the fluctuations of the central values are due to effects from the residual red-shifted high-frequency modes. Based on distributions in Figs. 14 and 15, the interval $k = [15H, m_r/10]$ looks reasonable choice to get the fitted spectral index with a relatively small fluctuations. The fit result of the spectral index q , assuming the log-hypothesis, in the interval $\log = [6.5, 7.8]$ for two benchmark simulations on lattice with $N^3 = 4096^3$ differing by relaxation types is presented in Table 2.

The outcome of fits with different assumptions on the form of the Likelihood function, UV/IR cutoffs on the momentum, and time interval $\Delta \log$ are summarized in Figs. 27 and 28. The discrepancy, compared to the result in Table 2, may be considered as part of systematic errors. Most importantly, despite all variant situations, our conclusion on the spectral index predicting $q \sim O(10)$ at $\log \frac{m_r}{H} \sim 70$ does not change.

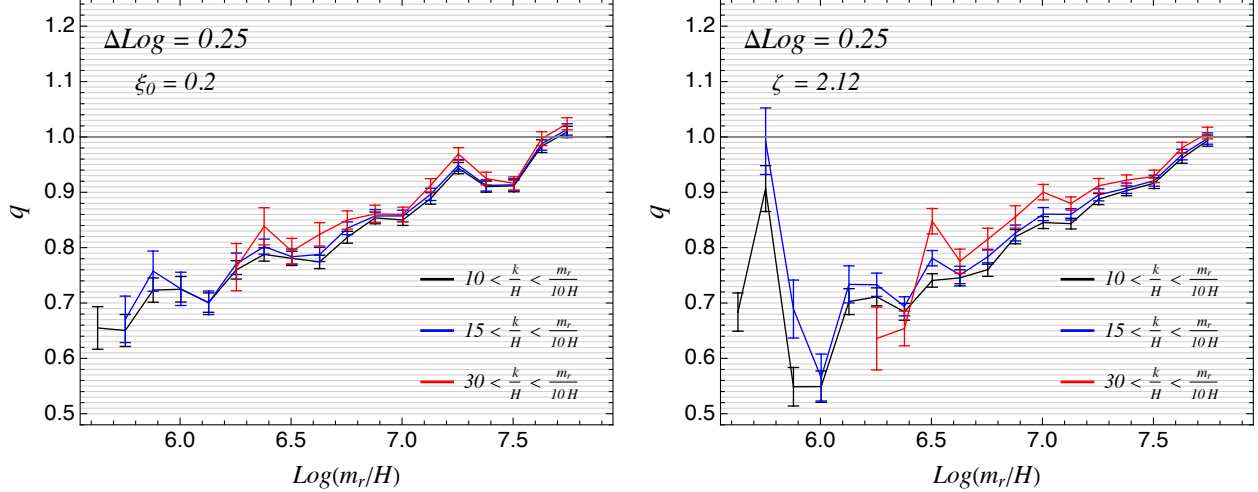


Figure 15: The spectral index q of the instantaneous emission F fitted in the interval with the varying x_{IR} while $x_{\text{UV}} = 10$. The error bars are statistical.

Pre-evolution type	Fit with $(x_{\text{IR}}, x_{\text{UV}}) = (15, 10)$	Interval for fit
Fat-string	$q \sim (-0.349 \pm 0.116) + (0.174 \pm 0.016) \log \frac{m_r}{H}$	$\log \frac{m_r}{H} = [6.5, 7.8]$
Thermal	$q \sim (-0.460 \pm 0.079) + (0.186 \pm 0.011) \log \frac{m_r}{H}$	$\log \frac{m_r}{H} = [6.5, 7.8]$

Table 2: The fit result taking the log-hypothesis from two benchmark simulations on $N^3 = 4096^3$ differing by the relaxation schemes. The presented errors are merely statistical ones within the particular choices of cuts on x_{IR} , x_{UV} and the fit intervals.

8 Axion abundance

The axion string network evolves until the time of the QCD crossover, denoted by t_* (roughly $\log_* \equiv \log \frac{m_r}{H(t_*)} \sim 70$), around which the axion mass m_a becomes comparable with the Hubble, or $m_a(t_*) \sim H_*$ and the axion potential becomes relevant. The impact of the logarithmically growing spectral index q of the instantaneous emission F , obtained from fitting the data in Section 7.1, on the axion abundance is dramatic. Despite the UV-dominated spectrum within the simulation time range, extrapolating the spectral index q until the time of the QCD crossover indicates the IR-dominated spectrum of axions radiated from strings at those late times. The system of strings and domain walls are formed around this time [51, 52]. Especially, when the number of domain walls are one, $N_W = 1$, the strings-and-walls system decay into axions [53] (see [13, 16, 54] for simulations). Similarly to [14], our estimate will not include axions from the collapse of strings-and-walls system. We will focus only on the axions radiated strings in the scaling regime and its evolution afterwards (later times than t_*) through the nonlinear regime in presence of the axion potential. Therefore, it sets the conservative lower bound on the axion abundance (thus the upper bound on the axion decay constant).

The axion energy density from strings in the scaling regime is still bigger than the axion

potential at $t = t_*$ due to the dominant energy density stored in gradient terms. It continues evolving until the time, denoted by t_ℓ , and it becomes comparable to the axion potential where axions transit to nonrelativistic ones. If the average axion field values are smaller than the axion decay constant, $\langle a^2 \rangle^{1/2} \ll f_a$, the nonlinearities due to the axion potential in the axion equations of motion can be ignored and the axion abundance will be obtained simply by evaluating $\int dk k^{-1} (\partial \rho_a / \partial k)$. Whereas, in the opposite situation, $\langle a^2 \rangle^{1/2} \gtrsim f_a$, the axion abundance at t_ℓ is affected by the nonlinearities and the estimation of the axion abundance is more tricky. The parametric behavior of $n_a^{\text{str}}(t_\ell)$, axion abundance from cosmic strings, in terms of string properties takes different forms depending on the spectral index q , the value of $\langle a^2 \rangle^{1/2} / f_a$, and the IR cutoff of the momentum. The detailed derivation of all distinctive cases are postponed to Appendix E. Here, we will discuss only relevant case to our situation.

The axion spectrum at the time $t = t_*$ can be obtained by evaluating

$$\frac{\partial \rho_a}{\partial k} = \int^t dt' \frac{\Gamma(t')}{H(t')} \left(\frac{R(t')}{R(t)} \right)^3 F \left[\frac{k'}{H(t')}, \frac{m_r}{H(t')} \right], \quad (20)$$

where the form of F for $q > 1$ is given in Appendix E and the transfer rate at late times is approximated by $\Gamma \sim \xi \mu_{\text{eff}} / t^3 \sim 8\pi H^3 f_a^2 \xi \log \frac{m_r}{H}$. When $q > 1$, the contribution to the axion abundance at $t = t_*$ from higher momenta is power suppressed as $\partial \rho_a / \partial k$ decreases faster than $\sim 1/k^q$, and only low momenta roughly $k < \sqrt{m_r H_*}$ which leads to the scaling $(\partial \rho_a / \partial k)|_{t_*} \propto k^{-1}$ dominantly contributes. It has been analytically approximated in [14] (and supported by numerical simulation) to estimate the axion abundance around the time $t = t_\ell$, taking into account the nonlinearities. It was shown that the topological production of axions with respect to the contribution from the misalignment mechanism with the angle of unity is expected to be scaling like $(n_a^{\text{str}, q>1} / n_a^{\text{mis}, \theta_0=1})|_{t_\ell} \propto (\xi_* \log_*)^{1/2+\dots}$ where ξ_* is the number of strings per Hubble patch at the time of the QCD crossover, $\log_* \sim 70$ and \dots denotes the dependency on the axion mass evolution. The exact value of q is not relevant as long as it is well above unity at the time of the QCD phase transition. Assuming that q continuously increases logarithmically, the ballpark of the axion dark matter mass will be similar to roughly what was estimated in [14].

As was discussed in Section 5.1, the average inter-string distance is roughly $(H\sqrt{\xi})^{-1}$ instead of H^{-1} . One may worry that axions whose momentum softer than $\sim H\sqrt{\xi}$ are suppressed and it may cause the parametrically reduced axion abundance. In Appendix E, we have shown that it can cause the non-negligible change of the overall size of the axion abundance at late times due to the slightly modified parametric dependence on string properties. It is also demonstrated in Fig. 16 for a set of selected parameters that will be further discussed in Section 8.1. However, the modified IR cutoff can significantly change parametric behavior if the small average axion field values $\langle a^2 \rangle^{1/2} \ll f_a$ are assumed. It is also true for the case with $q = 1$ similarly to [15] whose spectral index was claimed to be consistent with no-log hypothesis. The parametric behaviors of all distinctive cases are explicitly worked out in Appendix E.

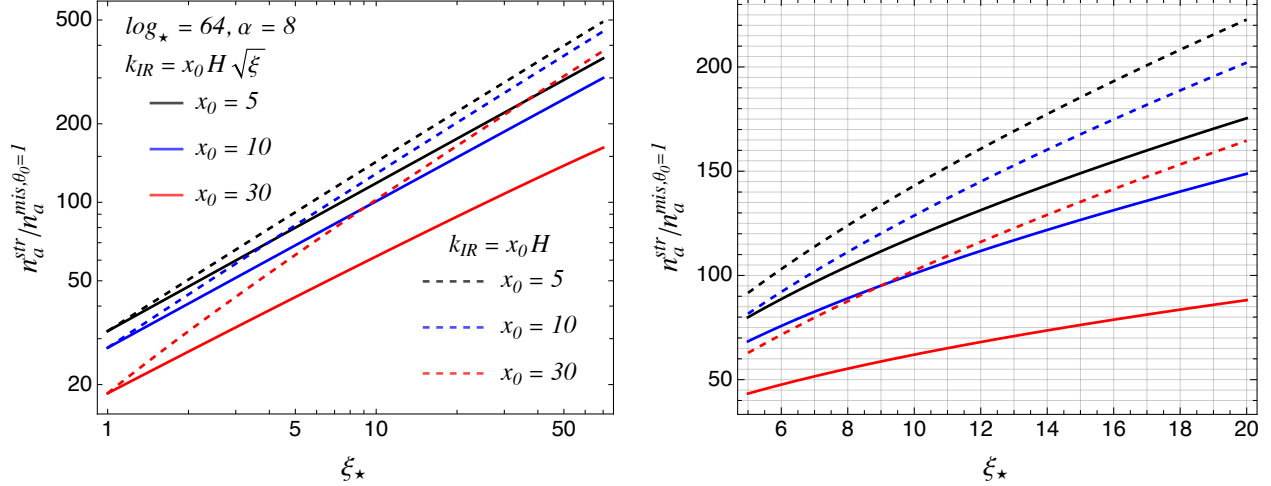


Figure 16: The analytic prediction of the axion abundance from strings with respect to the misalignment with $\theta_0 = 1$ as a function of ξ_* for varying x_0 while $\log_* = 64$ and $\alpha = 8$ are fixed. The solid lines correspond to those obtained with the IR momentum cutoff of $k_{\text{IR}} = x_0 H \sqrt{\xi_*}$ whereas the dashed ones are those with $x_0 H$. $c_n = 1.35$, $c_V = 0.13$, $c_m = 2.08$ and $c_n' = 2.81$ were taken from [14]. The right panel is zoomed-in version of the left one, and the color coding is the same as those in the left panel.

8.1 Bound on axion mass

The number of strings per the Hubble patch around time $\log_* = 64$ similarly to [14] is estimated from our simulation result, and they are $\xi_* = 13.4$ (fat-string pre-evolution) and $\xi_* = 16.6$ (thermal pre-evolution). Adopting fit values $c_n = 1.35$, $c_V = 0.13$, $c_m = 2.08$ and $c_n' = 2.81$ from [14] and setting $\alpha = 8$, the axion abundance with respect to the misalignment mechanism with the unit angle, given in Eq. (75) along with Eq. (76) in Appendix E, can be estimated to give $(n_a^{\text{str}, q>1} / n_a^{\text{mis}, \theta_0=1})|_{t_\ell} \sim 119$ (fat-string pre-evolution) and $(n_a^{\text{str}, q>1} / n_a^{\text{mis}, \theta_0=1})|_{t_\ell} \sim 134$ (thermal pre-evolution) with the choice of $x_0 = 10$ as an illustration. While the analytic predictions as a function of ξ_* for the different IR cutoff k_{IR} (with varying x_0) is illustrated in Fig. 16, more general expressions are given in Appendix E. The lower bound on the axion mass can be derived by requiring that the axion dark matter abundance does not exceed the currently observed value. Taking the reference value $\Omega_a^{\text{mis}} h^2 \approx 0.12 (28 \mu\text{eV}/m_a)^{7/6}$ in the post-inflationary scenario as in [14] where we assume $\langle \theta_0^2 \rangle \sim 5$ for translating it to $\Omega_a^{\text{mis}, \theta_0=1} h^2$ ⁹,

$$\Omega_a^{\text{str}} h^2 \approx \frac{n_a^{\text{str}, q>1}}{n_a^{\text{mis}, \theta_0=1}} \Omega_a^{\text{mis}, \theta_0=1} h^2 \leq 0.12 \rightarrow \begin{cases} m_a \gtrsim 420 (\mu\text{eV}) & : \text{ fat-string pre-evolution} \\ m_a \gtrsim 470 (\mu\text{eV}) & : \text{ thermal pre-evolution} . \end{cases} \quad (21)$$

Using $m_a \approx 5.7 \mu\text{eV} (10^{12} \text{ GeV} / (f_a / N_W))$ [56], $f_a / N_W \leq 1.3 \times 10^{10} \text{ GeV}$ (fat-string pre-evolution) and $f_a / N_W \leq 1.1 \times 10^{10} \text{ GeV}$ (thermal pre-evolution) for QCD axions are derived.

⁹The precise estimate of the contribution from the misalignment [7, 55, 56] amounts to shifting the bound.

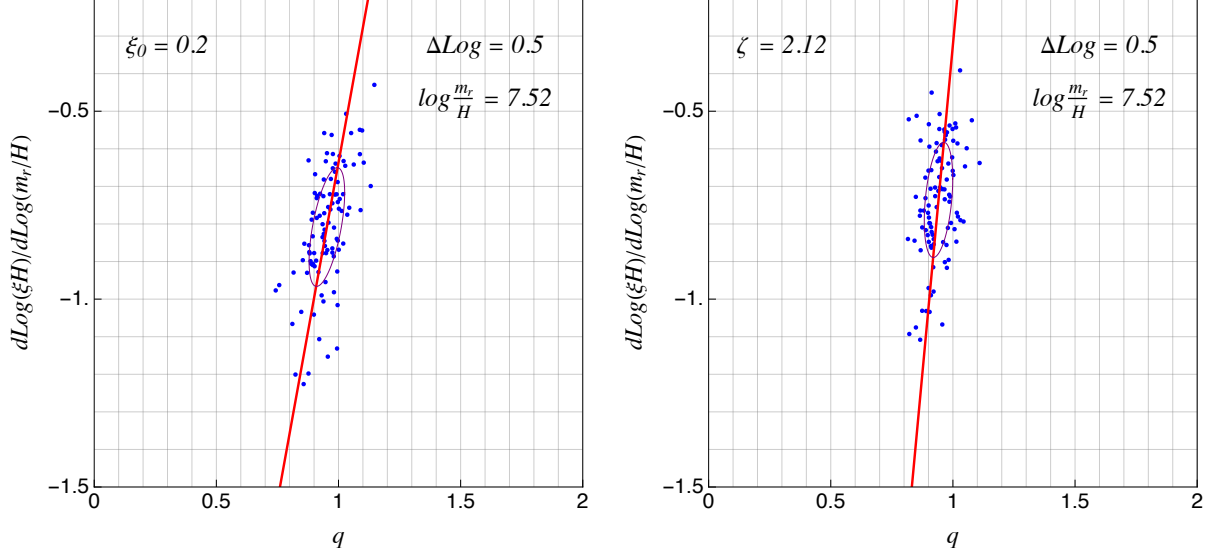


Figure 17: The correlation between q and $d\log(\xi H)/(d\log \frac{m_r}{H})$ over 100 ensemble elements from two benchmark simulations using the fat-string type pre-evolution (left) and thermal pre-evolution (right) on the lattice with $N^3 = 4096^3$.

9 Correlation between strings and axion spectrum

While our computing resources were limited only to two benchmarks, it would be interesting to explore possible observables or relations that can hint for the behavior for the benchmark points with different initial conditions. In this section, we investigate one such a correlation between q and time variation of ξH . While ξ in the scaling regime is the consequence of two competing factors, namely decays of strings and more strings entering into the Hubble patch, the quantity ξH will count only the effect from string decays. Each benchmark scenario for $\xi_0 = 0.2$ and $\zeta = 2.12$ consists of 100 independent simulations, and individual elements are spread around the central values in ξ and q distributions. Over all samples, the normalized differential change of ξH in logarithmic time, $d\log(\xi H)/(d\log \frac{m_r}{H})$, and spectral index q are computed at some time slices for various choices of $\Delta \log$. An illustrative example taken at $\log \sim 7.5$ is presented in Fig. 17 for the choice of $\Delta \log = 0.5$, and it reveals a strong correlation. The correlation is slightly less pronounced, when $\Delta \log = 0.25$ is used, and more pronounced with $\Delta \log = 0.75$ in that scattered data points are slightly less and more densely aligned along the correlation axes for the cases with $\Delta \log = 0.25$ and 0.75 , respectively. While the correlation is not stable in early times, it becomes robust at late times, for instance, the orientation of the correlation axis stays same for $\log \gtrsim 7$. A higher decay rate of strings is correlated with a smaller q according to Fig. 17. This looks consistent with the analytic study in [26, 32] that the faster string decay rates are associated with the emission of harder axions and vice versa. The detailed discussion is postponed to Appendix D.2.

Assuming that the similar correlation holds for different averaged ξ curves from different

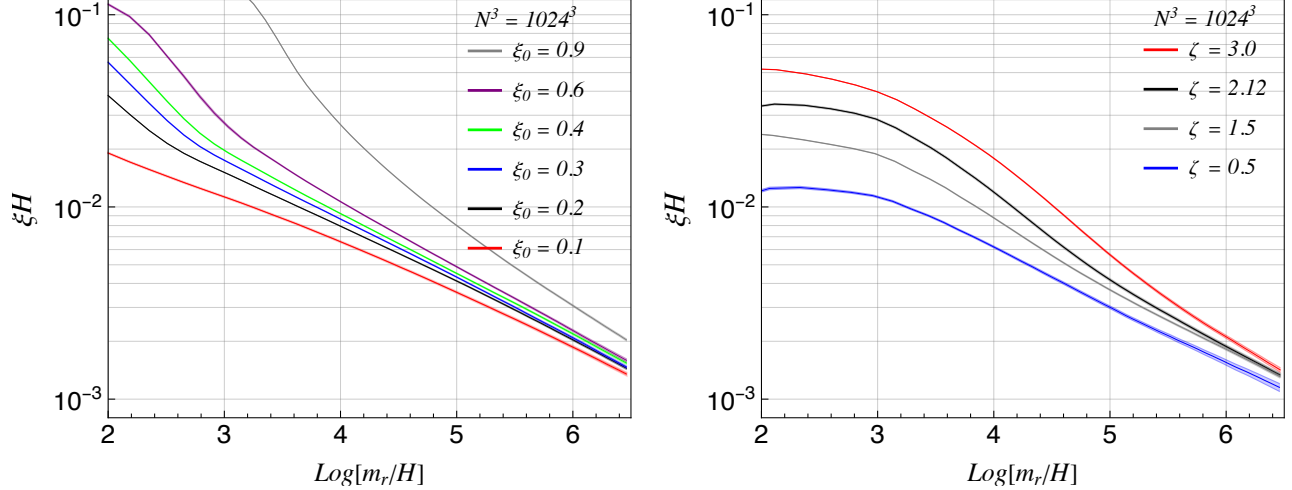


Figure 18: The ξH evolution from simulations using the fat-string type pre-evolution (left) and thermal pre-evolution (right) on the lattice with $N^3 = 1024^3$ for various initial conditions.

initial conditions of ξ_0 or ζ , the correlation in Fig. 17 can imply that the spectral index will have similar values in the vicinity of the benchmark points. For instance, the distributions of ξH from simulations on the smaller lattice with $N^3 = 1024^3$ are illustrated in Fig. 18. Although the maximal dynamic time range in Fig. 18 is smaller than $\log \sim 7$, it looks strong enough to support that the values of $d \log(\xi H) / (d \log \frac{m_r}{H})$ will become even closer at late times in the vicinity of the benchmark curves and thus the spectral index will not be significantly different from those from our benchmark simulations.

10 Conclusion

We have studied the dynamics of the global cosmic strings, originated from the PQ symmetry breaking, in the post-inflationary scenario where the definite prediction on the axion dark matter abundance can be made. We performed independent numerical checks on recently discovered various logarithmic scalings in properties of the cosmic string network. Especially, we provided the strong evidences for two logarithmically growing scalings in the number of strings in the Hubble patch and the spectral index of the power law of the axion spectrum against two differently prepared initial field configurations. Having established the strong evidence of $q > 1$ around the QCD scale, extrapolated from the simulation time, we pointed out a possible strong correlation between the axion spectrum and the string evolution with different initial conditions as a way of supporting the robust behavior of q against nearby string evolution trajectories with different initial data. We showed that this strong correlation agrees with the theoretical prediction from a simple string vibration model. The IR dominated spectrum of axions radiated from cosmic strings in the scaling regime may indicate the insensitivity to UV physics of cosmic string modeling. It will be interesting to see if this property can lead us an extra handle for

better understanding the nature of cosmic strings.

We surveyed various parametric behaviors of the axion abundance including the impact from the value of the spectral index, nonlinearities around the QCD scale, and average inter-string distances. This exercise should greatly help in extracting the lower bound on the axion mass accurately from the simulation result and comparing with different scenarios. Finally we estimated the lower bound on the axion mass based on our simulation.

Acknowledgments

We thank Masahide Yamaguchi for useful discussions. We thank Marco Gorghetto for discussions about their previous work. We thank the department of physics at KAIST for supporting with the computing resources in the cluster center. HK, JP, and MS were supported by National Research Foundation of Korea under Grant Number NRF-2021R1A2C1095430. The simulation in this work was supported by KISTI National Supercomputing Center under Project Number KSC-2023-CRE-0078.

A Equation of motion

The equation of motion from the Lagrangian in Eq. (1) in the expanding universe with the scale factor of R is given by

$$\ddot{\phi} + 3H\dot{\phi} - \frac{1}{R^2}\nabla^2\phi + \frac{m_r^2}{f_a^2}\phi\left(|\phi|^2 - \frac{f_a^2}{2}\right) = 0, \quad (22)$$

where dot is the differentiation with respect to the cosmic time t and the gradient ∇ is evaluated in the comoving coordinate. To simply our implementation in coding and numerical operation, we rescale field and spacetime coordinates to make them dimensionless in such a way that m_r^2/f_a^2 appears:

$$\phi \rightarrow f_a\phi, \quad t \rightarrow m_r^{-1}t, \quad \vec{x} \rightarrow m_r^{-1}\vec{x}, \quad (23)$$

under which $H \rightarrow m_r H$. After the rescaling, the equation of motion becomes

$$\ddot{\phi} + 3H\dot{\phi} - \frac{1}{R^2}\nabla^2\phi + \phi\left(|\phi|^2 - \frac{1}{2}\right) = 0, \quad (24)$$

where now dot is the differentiation with respect to the dimensionless cosmic time t and the gradient ∇ is evaluated in the dimensionless comoving coordinate. Similarly H is dimensionless.

Upon the discretization, the field evolution in terms of ϕ is subject to the CFL condition, $\Delta t \lesssim R\Delta x$. This condition requires arbitrarily small time step size in the early stage of the evolution where the scale factor is small, and it is rather inefficient from the simulation point of view. Since we want more sampling points at later times, we re-express the equation of motion

in terms of the rescaled field $\psi(\tau, \vec{x}) = R\phi(t, \vec{x})$ in the comoving spacetime coordinate,

$$\psi'' - \nabla^2\psi + \psi \left(|\psi|^2 - \frac{R^2}{2} - \frac{R''}{R} \right) = 0, \quad (25)$$

where the H -dependent term disappeared and it makes the simulation simpler. The CFL condition in this situation is relaxed to $\Delta\tau \lesssim \Delta x$. While the last term R''/R vanishes in the radiation dominated era, it may not vanish in the universe with a generic scale factor.

In the approach using the relaxation during the thermal evolution, we add the thermal mass term to the original Lagrangian,

$$\Delta\mathcal{L} = -\frac{m_r^2}{6f_a^2} T^2 |\phi|^2. \quad (26)$$

After the rescaling in Eq. (23) along with $T \rightarrow f_a T$ and the replacement $\psi(\tau, \vec{x}) = R\phi(t, \vec{x})$, the equation of motion for ϕ in the radiation dominated era becomes

$$\psi'' - \nabla^2\psi + \psi \left(|\psi|^2 - \frac{R^2}{2} + \frac{1}{6} R^2 T^2 \right) = 0, \quad (27)$$

where $T^2 = 2\zeta H$ (the definition of ζ will be given in Appendix B.5).

B Evolutions on the lattice

The approach toward the scaling solution can be boosted by the relaxation which cleans up the noisy short-distance string structure. The pre-evolution runs over the time interval $\tau = [\tau_{pi}, \tau_{pf}]$. The outcome of the pre-evolution is taken as the initial condition at $\tau = \tau_i$ for the actual physical string evolution. In our numerical simulation, three different time values, τ_{pi} , τ_{pf} , and τ_i are chosen to satisfy certain properties. In this section, we describe the detail of our simulation setup regarding two different types of the pre-evolutions.

In what follows, we present all the expressions in terms of the dimensionful spacetime to avoid any confusion. To make it easier to convert the dimensionful spacetime to the dimensionless one in the m_r unit for the convenience in the simulation, we adopt $R(t) = \sqrt{t/t_0}$ with $t_0 = 1/m_r$ for the radiation dominated era. In terms of the comoving time τ , $R(\tau) = \frac{\tau}{2} m_r$ as $t = (\frac{\tau}{2})^2 m_r$. For the situation with the scaling of $R(t) \propto t$, we adopt $R(t) = t/t_0$ again with $t_0 = 1/m_r$. In terms of τ , $R(\tau) = e^{m_r \tau}$ through $t = \frac{1}{m_r} e^{m_r \tau}$. One can pair t and/or x with m_r to convert it to the dimensionless one in the m_r unit.

B.1 Common setup

We first explain how we set Δx which allows the longest simulation time in m_r/H . For given N , one can require the minimum number of the lattice points within the core at the final time, denoted by n_c , and the minimum number of the Hubble length within the simulation box L at

the final time, denoted by n_H :

$$\frac{m_r^{-1}}{R\Delta x} \geq n_c, \quad \frac{L}{H^{-1}} = \frac{NR\Delta x}{H^{-1}} \geq n_H \quad \rightarrow \quad \frac{m_r}{H} \leq \frac{N}{n_c n_H}, \quad (28)$$

where the maximum time coverage in m_r/H is reached when two inequalities in Eq. (28) for n_c and n_H are saturated at the same time. The lattice spacing Δx is set to guarantee the maximal m_r/H , and it is given by

$$\Delta x = \frac{m_r^{-1}}{n_c R(t)} \Big|_{t=(1/2H)_{\max}} = \frac{m_r^{-1}}{n_c} \left(\frac{2n_c n_H}{N} \right)^{1/2}. \quad (29)$$

The step size of the conformal time $\Delta\tau$ is chosen to $\Delta\tau = r_{\text{CFL}} \Delta x$ where $r_{\text{CFL}} = 1/3 \sim 1/10$ depending on the simulation approach.

It is useful to compare this setup with that in the simulation assisted by the AMR. When turning on the AMR which zooms in a local region recursively by the factor of 2^k , one can repeat the similar steps as in Eq. (28) with the replacement of either $n_c \rightarrow n_c/2^k$ or $N \rightarrow 2^k N$ (up to the implication to Δx) to estimate the maximal time coverage. In either choice, the maximum dynamic time range in $\log \frac{m_r}{H}$ is extended to (by $k \ln 2$)

$$\log \frac{m_r}{H} \leq \log \frac{N \cdot 2^k}{n_c n_H}. \quad (30)$$

Since $N \rightarrow 2^k N$ implies that the local resolution effectively increases by the factor of 2^k , Δx in Eq. (28) corresponds to the lattice spacing of the finest grids in the comoving coordinate,

$$\Delta x|_{\text{Finest grids by } 2^k} = \frac{m_r^{-1}}{n_c} \left(\frac{2n_c n_H}{2^k N} \right)^{1/2}. \quad (31)$$

On contrary, $n_c \rightarrow n_c/2^k$ in Eq. (28) implies that the minimum number of grids within the core is relaxed by the factor of 2^k since the local region around the string core will be resolved later up to by 2^k . In this case, Δx in Eq. (28) corresponds to the lattice spacing of the coarsest grids in the comoving coordinate,

$$\Delta x|_{\text{Coarsest grids}} = \frac{m_r^{-1}}{n_c} \left(\frac{2n_c n_H}{N} \right)^{1/2} \times 2^{k/2}, \quad (32)$$

which is $2^k \times \Delta x|_{\text{Finest grids by } 2^k}$ and it should be compared to the lattice spacing of the static simulation for the region away from strings. A peculiar feature of the scaling in Eq. (32) is that the lattice spacing away from strings in AMR is larger than that of the static case by the factor of $2^{k/2}$ for fixed n_c and N . This can be compensated with a larger n_c .

B.2 Fat string pre-evolution: $R(t) \propto \sqrt{t}$

The first scheme introduced in [9] is that, during the fat-string pre-evolution, the core radius $m_{r,\text{fat}}^{-1}$ scales as $R \propto \sqrt{t}$ while the VEV of ϕ is fixed to be f_a , or equivalently, the string is made to be fat such that its size r_{fat} in the comoving coordinate stays the same during the evolution. The quartic coupling scales as $1/R^2$ ¹⁰,

$$\frac{m_{r,\text{fat}}^2}{2f_a^2} = \frac{1}{2f_a^2 R^2 (m_{r,\text{fat}}^{-1}/R)^2} = \frac{1}{2f_a^2 R^2 r_{\text{fat}}^2} \propto \frac{1}{R^2}. \quad (33)$$

We choose the string core size during the fat string pre-evolution to match the value at the initial time τ_i of the physical evolution, or

$$r_{\text{fat}}(\tau_i) = \left. \frac{m_{r,\text{fat}}^{-1}}{R} \right|_{\tau=\tau_{pi}} = \frac{m_r^{-1}}{R(\tau_i)} = m_r^{-1} \times \frac{2}{m_r \tau_i}. \quad (34)$$

The number of lattice points within the string core at the initial time τ_i , denoted by N_r , of our physical string simulation is given by

$$N_r = \left. \frac{m_{r,\text{fat}}^{-1}}{\Delta x R} \right|_{\tau=\tau_{pi}} = \frac{m_r^{-1}}{\Delta x} \times \frac{2}{m_r \tau_i}. \quad (35)$$

This allows us to start the physical evolution from the same initial time τ_i for the given Δx and N_r . We choose the initial time of the pre-evolution τ_{pi} such that the number of lattice within the Hubble length at τ_{pi} is roughly a similar order of the one within a wavelength of the string core, $2\pi m_r^{-1}$, at the time τ_i up to an arbitrary constant α ,

$$\underbrace{\frac{\tau_{pi}}{\Delta x} = \frac{H^{-1}}{\Delta x R} \Big|_{\tau_{pi}}}_{\text{Number of lattice within the Hubble length}} = \alpha \times \underbrace{\frac{m_r^{-1}}{\Delta x R} \Big|_{\tau_i}}_{\text{Number of lattice within the string core}}, \quad (36)$$

where the second term is equal to αN_r which stays the same over the entire fat string evolution. The role of the condition in Eq. (36) is to achieve roughly the reasonable size of the correlation length of the cosmic string at τ_i . The ambiguity in the identification in Eq. (36) is taken into account by the constant α that can be empirically determined. The setting in Eq. (36) ensures that $\frac{m_{r,\text{fat}}}{H} \Big|_{\tau_{pi}} \sim \alpha$ which is taken to be order one. The ending time of the fat-string evolution τ_{pf} is determined by demanding the requested value for the number of strings per Hubble patch

¹⁰The decreasing quartic coupling in this scheme indicates that the field becomes less and less interacting with the evolution, and it might be the reason for why the simulation reach the attractor solution faster than the case for the physical string simulation.

ξ_0 , namely, $\xi(\tau_{pf}) = \xi_0$ ¹¹. The value of τ_{pf} varies depending on ξ_0 , and the correlation length at τ_{pf} (which will be the property of the initial condition for the physical string evolution) is determined posteriori. A drawback is that the correlation length with respect to the core radius can significantly grow until τ_{pf} due to the scaling, $\frac{m_{r,\text{fat}}}{H}|_{\tau_{pf}} \propto \tau$. While the value of τ_i for the physical string evolution can be freely chosen irrespective of τ_{pf} (τ_i is not necessarily larger τ_{pf}), the implicit correlation length at τ_i is genuinely determined by the configuration of fields at τ_{pf} instead of being determined in terms of $H^{-1}(\tau_i)$. While the condition in Eq. (36) looks a bit ad-hoc, it will be replaced by more consistent one in the second scheme.

B.3 Fat string pre-evolution: $R(t) \propto t$

The second scheme that we take as a default option for the pre-evolution was introduced in [14]. In this scheme, during the fat-string evolution, the core radius m_r^{-1} scales as $R_{\text{fat}} \propto t \sim H_{\text{fat}}^{-1}$ while the VEV of ϕ is fixed to be f_a . Similarly to the option 1 in Section B.2, we match the core radii in the comoving coordinate in the transition from the pre-evolution to the physical one,

$$r_{\text{fat}}(\tau_i) = \left. \frac{m_{r,\text{fat}}^{-1}}{R_{\text{fat}}} \right|_{\tau=\tau_{pi}} = \frac{m_r^{-1}}{R(\tau_i)} = m_r^{-1} \times \frac{2}{m_r \tau_i}. \quad (37)$$

The number of lattice points within the string core at the initial time τ_i will be the same as that during the pre-evolution. Since $H_{\text{fat}}^{-1}/R_{\text{fat}}$ stays constant during the pre-evolution, we can maintain the exactly same correlation length in the comoving coordinate at τ_i as the one at τ_{pi} by demanding

$$\left. \frac{H_{\text{fat}}^{-1}}{\Delta x R_{\text{fat}}} \right|_{\tau_{pi}} = \left. \frac{H^{-1}}{\Delta x R} \right|_{\tau_i} = \frac{\tau_i}{\Delta x}, \quad (38)$$

which sets the comoving Hubble length H^{-1}/R during the pre-evolution to τ_i . Combining two relations in Eqs. (37) and (38), it is straightforward to see that the correlation length over the core size stays the same, that is,

$$\frac{m_{r,\text{fat}}(\tau)}{H_{\text{fat}}(\tau)} = \frac{R_{\text{fat}}(\tau)}{m_{r,\text{fat}}^{-1}(\tau)} \frac{H_{\text{fat}}^{-1}(\tau)}{R_{\text{fat}}(\tau)} = \left. \frac{R}{m_r^{-1}} \right|_{\tau_i} \left. \frac{H^{-1}}{R} \right|_{\tau_i} = \frac{m_r}{H(\tau_i)}, \quad (39)$$

where the initial correlation length over the core size is given by $\frac{m_r}{H(\tau_i)} = \frac{1}{2} m_r^2 \tau_i^2$. The initial time for the physical string evolution τ_i is fixed by Eq. (38)¹² in this scheme which accordingly determines N_r through Eq. (37). Similarly to the option 1 in Section B.2, the final time of the pre-evolution is determined by requesting a certain number of strings per Hubble patch

¹¹While the fat string evolution can be designed to be terminated at τ_{pf} when it reaches the same requested correlation length, the initial value ξ_0 will not be same in this case.

¹²The freedom to choose any value of τ_i (or the freedom to choose any desired value of $\frac{m_r}{H(\tau_i)}$) effectively amounts to introducing α in $R(t) = \alpha(t/t_0)$, or $\tau_i = \frac{1}{\alpha m_r}$ from Eq. (38).

ξ_0 , namely, $\xi(\tau_{pf}) = \xi_0$. While the initial time τ_{pi} of the pre-evolution is apparently a free parameter, we set it to $\tau_{pi} = 0$.

B.4 From pre-evolution to physical one

Since field equations in two regions in options 2 and 3 are qualitatively different and not physically equivalent, there may not be a unique way of gluing two regions. In this work, we join two regions by two relations,

$$\begin{aligned} (R^{-1}\psi)|_{\tau=\tau_{pf}} &= (R^{-1}\psi)|_{\tau=\tau_i} , \\ \left(-\frac{R'}{R^2}\psi + \frac{1}{R}\psi'\right)|_{\tau=\tau_{pf}} &= \left(-\frac{R'}{R^2}\psi + \frac{1}{R}\psi'\right)|_{\tau=\tau_i} , \end{aligned} \quad (40)$$

where the second relation is the continuity of $(R^{-1}\psi)'$, or the velocity of $R^{-1}\psi$ with respect to the conformal time and it ensures that the energy density is smoothly connected between two regions¹³. We empirically find that maintaining the continuity of the energy density in the transition is strongly favored not to artificially introduce the discrete enhancement of the radial modes in the transition from the pre-evolution to the physical one.

B.5 Thermal pre-evolution

We continue presenting the relations in terms of the dimensionful parameters. The expressions in terms of the dimensionless quantities can be straightforwardly obtained as the previous discussion along with the rescaling T by f_a . The critical temperature T_c is given by $T_c = \sqrt{3}f_a$. Using the relation for the Hubble parameter $H^2 = \frac{\pi^2}{90}g_*\frac{T^4}{M_p^2}$, the temperature can be expressed as

$$T^4 = f_a^4 \times \frac{H^2}{m_r^2} \times 4\zeta^2 \quad \text{with} \quad \zeta^2 = \frac{45}{2\pi^2 g_*} \frac{M_p^2 m_r^2}{f_a^4} , \quad (41)$$

from which the correlation length over the core size at the critical temperature T_c is given by

$$\frac{m_r}{H}|_{T_c} = \frac{2}{3}\zeta . \quad (42)$$

While $\zeta \sim \mathcal{O}(1)$ ensures the order one size of $\frac{m_r}{H}$ at the phase transition where cosmic strings are formed, the natural size of it is given by

$$\zeta = 2 \times 10^7 \left(\frac{100}{g_*}\right)^{1/2} \left(\frac{\lambda}{1}\right)^{1/2} \left(\frac{M_p}{1. \times 10^{18}\text{GeV}}\right) \left(\frac{1. \times 10^{10}\text{GeV}}{f_a}\right) . \quad (43)$$

¹³While the velocity $\dot{\phi}$ is discontinuous in this scheme, we have numerically checked that the impact of the discontinuity on the scaling solution is negligible.

Eq. (43) implies that the order one size of ζ corresponds to the symmetry breaking scale of $f_a \sim 10^{17}$ GeV, a huge number of relativistic degrees of freedom of $g_* \sim 10^{14}$, or an extremely small quartic coupling¹⁴ $\lambda = \frac{m_r^2}{2f_a^2} \sim 10^{-15}$ (or the combination of three factors). This might be considered to be a drawback of this option. The initial time of the simulation τ_i can be chosen to be any value earlier than the phase transition time τ_c which is given by, using Eq. (42),

$$\tau_c^2 = m_r^{-2} \times \frac{4}{3} \zeta. \quad (44)$$

In our numerical simulation, we fix the initial time to $\tau_i = 0.1\tau_c$ with the varying ζ . The value of ζ can be fixed to have a specific Hubble length in the m_r^{-1} unit at the critical temperature as was indicated in Eq. (42), for instance, $\zeta = \frac{3}{\sqrt{2}} \sim 2.12132$ for $\frac{m_r}{H}|_{\tau_c} = \sqrt{2}$, and it implies $\frac{m_r}{H}|_{\tau_i} = \left(\frac{\tau_i}{\tau_c}\right)^2 \frac{m_r}{H}|_{\tau_c}$ at the initial time τ_i .

B.6 Random initial conditions

In fat string type relaxations explained in Sections B.2 and B.3, a random field configuration ϕ (and its velocity $\dot{\phi}$) is generated with the Fourier modes with the wavenumber truncated at m_r , or $|\vec{k}|_{\max} = \frac{2\pi}{N\Delta x R(\tau_i)} |\vec{n}_k|_{\max} = m_r$. The field can be discretized as $\phi(\vec{x} = \Delta x \vec{n}_x) = \sum_{\vec{n}_k} \frac{1}{(N\Delta x R)^3} \tilde{\phi} \left(\frac{2\pi}{N\Delta x R} \vec{n}_k \right) \exp \frac{2\pi i \vec{n}_k \cdot \vec{n}_x}{N}$ where the Fourier mode $\tilde{\phi}(\vec{k})$ is randomly generated below the cutoff scale of the momentum as $\tilde{\phi}_0 \frac{\text{Rand}_1 + i \text{Rand}_2}{\sqrt{2}}$ where $\text{Rand}_{1,2}$ are random numbers following the standard normal distribution such that $\langle \text{Rand}_i(\vec{n}_{k_1}) \text{Rand}_j(\vec{n}_{k_2}) \rangle = \delta_{ij} \delta_{\vec{n}_{k_1} \vec{n}_{k_2}} (N\Delta x R)^3$. The overall size $\tilde{\phi}_0$ is chosen such that $\langle |\phi(\vec{n}_x)|^2 \rangle = f_a^2 \times \frac{1}{2}$:

$$\langle \phi^*(\vec{n}_{x_1}) \phi(\vec{n}_{x_2}) \rangle = |\tilde{\phi}_0|^2 \sum_{\vec{n}_k} \frac{1}{(N\Delta x R)^3} \exp^{-\frac{2\pi i \vec{n}_k \cdot (\vec{n}_{x_1} - \vec{n}_{x_2})}{N}}, \quad (45)$$

where the sum is truncated at $|\vec{n}_k|_{\max}$. The randomly generated Fourier mode $\tilde{\phi}$ is given by

$$\tilde{\phi} = \frac{f_a}{\sqrt{2}} \frac{(N\Delta x R)^{3/2} \text{Rand}_1(\vec{n}_k) + i \text{Rand}_2(\vec{n}_k)}{\sqrt{N_k}} \theta(|\vec{n}_k|_{\max} - |\vec{n}_k|), \quad (46)$$

where N_k is the total number of lattice points within the sphere in the momentum space, which is defined as $N_k \equiv \frac{1}{(\Delta k)^3} \int d^3 \vec{k} \theta(|\vec{n}_k|_{\max} - |\vec{n}_k|)$ in terms of the notation in the continuum limit, and θ is a step function. The random velocity distribution for ϕ' is similarly generated with the Fourier mode further weighted by RE , compared to $\tilde{\phi}$ in Eq. (46), where $E(\vec{k} = 2\pi \vec{n}_k / (N\Delta x R)) = \sqrt{m_r^2 + \vec{k}^2}$.

In the thermal relaxation scheme in Section B.5, the initial conditions for the field and velocity are generated assuming the Gaussian random field configuration following the thermal distributions as in [10]. Similarly to the fat string type relaxation, a random field configuration

¹⁴This looks like a similar unnatural situation in the fat-string type pre-evolution which relies on the quartic coupling scaling away as R^{-2} .

and its velocity will be generated with an appropriate cut on the wavenumber. For the periodic boundary condition, the lowest wavenumber in the m_r unit at the initial time is given by $\left. \frac{k_{\min}}{m_r} \right|_{t_i} = \left. \frac{2\pi}{m_r R N \Delta x} \right|_{t_i} = \frac{10\sqrt{3}}{\sqrt{\zeta}} \frac{2\pi}{(2n_H N/n_c)^{1/2}}$. The cutoff on the physical momentum will be imposed as the multiple of m_r . It will correspond to including only $|\vec{n}_k|_{\max}$ number of lowest modes, or $k_{\max} = \frac{2\pi}{R N \Delta x} |\vec{n}_k|_{\max} = \kappa m_r$ at $\tau = \tau_i$ from which $|\vec{n}_k|_{\max} = \kappa (k_{\min}/m_r)^{-1}|_{\tau_i}$. For $\zeta = 2.12$ and $N = 1024/2048/4096$ along with our default setting $n_H = 4^{1/3}$ and $n_c = 1$, $(k_{\min}/m_r)^{-1}|_{\tau_i} \sim 0.763/1.079/1.526$. Therefore, the cut $k_{\max}|_{\tau_i} \leq 10 m_r$ is equivalent to including only $|\vec{n}_k| \lesssim 8/11/15$ lowest modes, respectively. As $k_{\max} \propto \tau^{-1}$, $k_{\max}|_{\tau_i} \leq 10 m_r$ will imply $k_{\max}|_{\tau_c} \leq m_r$ with the choice of $\tau_i = 0.1\tau_c$ (note that m_r denotes the constant string core scale).

B.7 Tetrahedron-based string identification

We subdivide the entire lattice box into a series of tetrahedrons as in the left panel of Fig. 1, and decide whether a string penetrates a face or not by examining the pattern of the phases in three vertices. Once the criterion for the existence of a string is met, we simply determine the string core by the linear interpolation (although it is not guaranteed to be the truth position). In this approach, we estimate total string length in the simulation box by summing over all line segments connecting string cores. On the other hand, since the position of the string core over the plaquette (see right panel of Fig. 1) through which a string penetrates is likely randomly distributed from the statistics point of view, the total string length in the simulation box can be estimated by just counting the number of plaquettes and multiply it by a weighting factor [34]. Using the simulation on the grid with $N^3 = 1024^3$, we have compared our algorithm with the string identification in [34], and the discrepancy $\Delta\xi/\xi$ over the entire simulation time was found to be smaller than a few %. Since we want to visualize the string formation and take snapshots at some selected times, we take our approach for the estimation of the total string length. The number of long strings per Hubble patch in our simulation is calculated as

$$\xi = \frac{(L_{\text{Lattice unit}} \Delta x R) t^2}{(N \Delta x R)^3} = \frac{L_{\text{Lattice unit}} t^2}{N^3 \Delta x^2 R^2}. \quad (47)$$

where $L_{\text{Lattice unit}}$ is the total length of strings measured in a lattice unit.

In our prescription using the tetrahedron, the surface of the tetrahedron in the left panel of Fig. 1 is the triangle with three vertices, call them $v_{i=1,2,3}$. Given the complex field values on three vertices, one can define $\theta_{ij} = \arg(\phi_j/\phi_i) = \arg(\phi_j\phi_i^*)$. A string core on the triangular surface is declared if $\theta_{123} \equiv \theta_{12} + \theta_{23} + \theta_{31}$ has the value of $\pm 2\pi$. Note that θ_{123} can have only $0, \pm 2\pi$. In practice, the computation of the arguments for all complex fields are time-consuming. To reduce the computational time, we replace the above criterion with more efficient equivalent step. $\theta_{123} = 2\pi$ (-2π) is equivalent to the situation where all θ_{ij} 's are non-negative (non-positive) while not all of them are zero. The sign of θ_{ij} is equivalently replaced with that of $\omega_{ij} = \Re\phi_i\Im\phi_j - \Im\phi_i\Re\phi_j$. Therefore, $\theta_{123} = 2\pi$ (-2π) is equivalent to the case where all ω_{ij} 's are non-negative (non-positive) while ω_{123} is positive (negative) ($\omega_{123} \equiv \omega_{12} + \omega_{23} + \omega_{31}$). Once

the string core is identified, the location of the string core inside the triangle where the field value vanishes is assigned via the linear interpolation, or $(\omega_{23}v_1 + \omega_{31}v_2 + \omega_{12}v_3)/\omega_{123}$ where v_i is the position of the i -th vertex on the triangle. It can be easily proven that the string core is strictly inside the triangle. This approach is well-defined as each tetrahedron includes either a pair of two faces on which string cores are found or none, and thus strings are guaranteed to be connected without any discontinuity. We find that our tetrahedron-based string identification algorithm is quite efficient in the numerical simulation.

The connectedness of the string in our tetrahedron approach of the string identification can be rigorously proven as follows. One can introduce an arbitrary complex field as a linear function of coordinates, $\phi_{\text{inter}}(x, y, z) = \beta_0 + \beta_1x + \beta_2y + \beta_3z$ with four complex constants which we fix them by matching the interpolating field ϕ_{inter} to field values at four vertices, labeled as $v_{i=0,1,2,3}$, of the tetrahedron, or $\phi_{\text{inter}}(v_i) = \phi_i$. That is, $\phi_{\text{inter}}(x, y, z)$ interpolates between vertices of the tetrahedron in three-dimensional space. The linear interpolation of the field on the triangular face of the tetrahedron is equivalent to restricting ϕ_{inter} onto the triangle. In this picture, the corresponding triangular face will be declared to have a string core if and only if the triangular face and the locus of zero, $\phi_{\text{inter}}(x, y, z) = 0$, intersect. $\phi_{\text{inter}}(x, y, z) = 0$ represents the straight line as it is collection of two constraints (for real and complex components of β 's) in three-dimensional space. A straight line can penetrate only a pair of triangular faces of the tetrahedron if it intersects unless the line passes through a vertex or an edge of the tetrahedron. Therefore, there must be none or exactly two triangular faces which are penetrated by a cosmic string. This prescription will work well for long strings compared to the size of the tetrahedron.

B.8 Masking

The axion energy density is approximated by $2 \times \langle \frac{1}{2} \dot{a}^2 \rangle$ where $\langle \dots \rangle$ denotes (with the abuse of the notation) the spatial average over the physical space (denoted by $\vec{x}_p = R\vec{x}$),

$$\rho_a = \frac{1}{L^3} \int d^3\vec{x}_p \dot{a}^2(\vec{x}_p) = \frac{1}{L^3} \int \frac{d^3\vec{k}}{(2\pi)^3} |\tilde{a}(\vec{k})|^2, \quad (48)$$

from which the axion energy spectrum for the momentum k is given by

$$\frac{\partial \rho_a}{\partial k} = \frac{k^2}{2\pi^2 L^3} \int \frac{d\Omega_k(\hat{k})}{4\pi} \left| \tilde{a}(\vec{k} = k\hat{k}) \right|^2. \quad (49)$$

Importantly, $\dot{a}(\vec{x}_p)$ in Eq. (48) should be the axion field velocity with the string effect removed. To this end, in presence of strings, the masking function needs to be applied to the unmasked axion velocity field to screen off the effect from string cores and extract the pure axion energy density,

$$\tilde{a}_{\text{masked}}(\vec{k}) = \int d^3\vec{x}_p W(\vec{x}_p) \dot{a}_{\text{unmasked}}(\vec{x}_p) e^{-i\vec{k}\cdot\vec{x}_p}, \quad (50)$$

where $W(\vec{x}_p)$ is the masking function. We adopt the natural masking $W(\vec{x}_p) = (1 + r(\vec{x}_p)/f_a)$ for the smooth screening the string core effect as a default. Another choice for the masking adopted in literature is the hard-masking which sets $W = 0$ for the region with distance from string $r < d_s m_r^{-1}$ (for some positive d_s) and $W = 1$ outside the region. The masked Fourier transform $\tilde{a}_{\text{masked}}(\vec{k})$ is related to the Fourier transform $\tilde{a}(\vec{k})$ of the axion velocity field $\dot{a}(\vec{x}_p)$, now separated from the string effect, by the convolution,

$$\tilde{a}_{\text{masked}}(\vec{k}) = \int \frac{d^3 \vec{k}'}{(2\pi)^3} \tilde{W}(\vec{k} - \vec{k}') \tilde{a}(\vec{k}') , \quad (51)$$

where $\tilde{W}(\vec{k})$ is the Fourier transform of the masking function $W(\vec{x}_p)$ itself. In our simulation, $\mu_{a,\text{masked}}(k) = \int \frac{d\Omega_k}{4\pi} |\tilde{a}_{\text{masked}}(\vec{k})|^2$ and similarly $\mu_W(k) = \int \frac{d\Omega_k}{4\pi} |\tilde{W}(\vec{k})|^2$ are numerically computed. The value of $\mu_a(k) = \int \frac{d\Omega_k}{4\pi} |\tilde{a}(\vec{k})|^2$ for the axion velocity with the string core effect screened off can be obtained by inverting the following relation,

$$\mu_{a,\text{masked}}(k) = \frac{1}{4\pi^2 k L^3} \int dk' k' \left(\int_{|k-k'|}^{k+k'} dk'' k'' \mu_W(k'') \right) \mu_a(k) . \quad (52)$$

This relation is derived under the assumption that each \vec{k} modes of \dot{a} are independent and has random amplitude from mean zero Gaussian ensemble whose variance only depends on the size of the momentum k . Here, $\mu_{a,\text{masked}}$ and $\mu_a(k)$ need to be the average over the ensemble to make the relation mathematically exact. Using the relation to get μ_a from the measured $\mu_{a,\text{masked}}$ is secretly relying on the law of large number applied to $\mu_{a,\text{masked}}(\vec{k})$ for \vec{k} 's with large number of different directions and the same magnitude. However, once space is discretized, and so is the momentum, there are only a few number of different momentum \vec{k} for small magnitude k , and this may result in larger uncertainty at low momentum region while estimating the unmasked spectrum. Using $\mu_a(k)$ extracted from Eq. (52), the axion energy spectrum for the momentum k with the string core effect screened off is given by

$$\frac{\partial \rho_a}{\partial k} = \frac{k^2}{2\pi^2 L^3} \mu_a(k) . \quad (53)$$

Similar masking is applied to the radial modes.

C Dependency on initial conditions and relaxations

C.1 Scaling regime and fitting

The underlying assumption behind the pre-evolution is that the string network eventually approaches the scaling solution. Any residual influence from the different pre-evolutions or/and different initial conditions should be faded away as the string network enters the scaling regime. Any justification for it within the consistent numerical setup should be highly beneficial. To

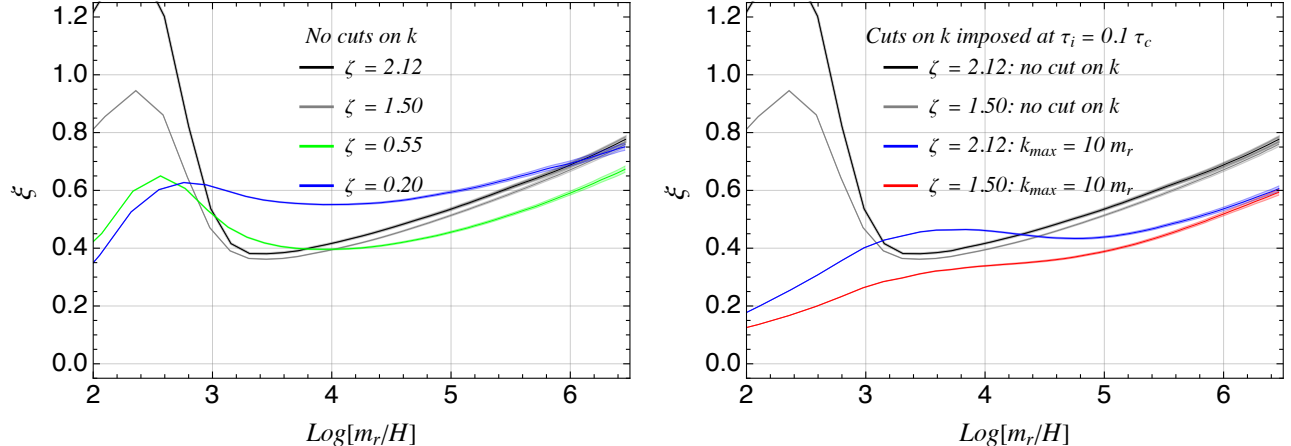


Figure 19: The impact of higher modes above $k_{\max} = 10m_r$ on ξ for physical string simulations with initial data generated with the thermal pre-evolution. Note that $k_{\max} = 10m_r$ at $\tau_i = 0.1\tau_c$ is equivalent to $k_{\max} = m_r$ at τ_c .

this end, we extend our discussion in Section 5 to include more comprehensive and detailed comparisons between results obtained by two different pre-evolution schemes for various initial data. We do this task mainly with simulations on the lattice of $N^3 = 1024^3$ to accumulate as many simulation runs as possible for various initial conditions within a reasonable time. As was discussed in Section 5 and illustrated in Fig. 2, this task helped us in choosing our benchmark points to be run on a larger lattice space for the study at much later dynamic time.

The left panel of Fig. 19 is similar to the right panel of Fig. 2 except that the cutoffs on the momentum were not imposed. That is, the initial configurations with k modes between maximally allowed value (set by the lattice spacing and lattice size) and $10m_r$ at $\tau_i = 0.1\tau_c$ were included. While the ξ curves in the left panel of Fig. 19 illustrate the approach toward the scaling regime, the ξ values are overall larger than those with momentum cutoffs as is evident in the right panel of the same Fig. 19 where the dependence on the k cutoffs is demonstrated for two selected ζ values.

Since the maximally allowed k modes varies with the lattice size, ξ curves obtained from simulations with different lattice sizes do not overlap, and the simulation on the larger lattice space populates more strings and takes longer time to be relaxed. The cutoffs on the momentum removes this ambiguity as is illustrated in Fig. 20 for two benchmark simulations: $\xi_0 = 0.2$ using fat-string pre-evolution (left panel) and $\zeta = 2.12$ (with $\tau_i = 0.1\tau_c$) using thermal pre-evolution (right panel). Since the same momentum modes are initially randomly generated irrespective of the lattice size, the ξ curves exactly on top of each other¹⁵. A good agreement between different

¹⁵The slight mismatch between $N^3 = 1024^3$ and $N^3 = 2048^3$ in the right panel of Fig. 20 is due to the round-off error, for instance, the cutoff $k > 10m_r$ includes k modes within the radius of roughly ~ 8 and ~ 11 for $N^3 = 1024^3$ and $N^3 = 2048^3$, respectively, (see Appendix B.6) and rounding-off causes an error up to 10%. We have checked via independent simulations that increasing the cutoff, allowing more k modes, makes the effect due to the round-off error negligible. A similar statement applies to the case with $N^3 = 4096^3$.

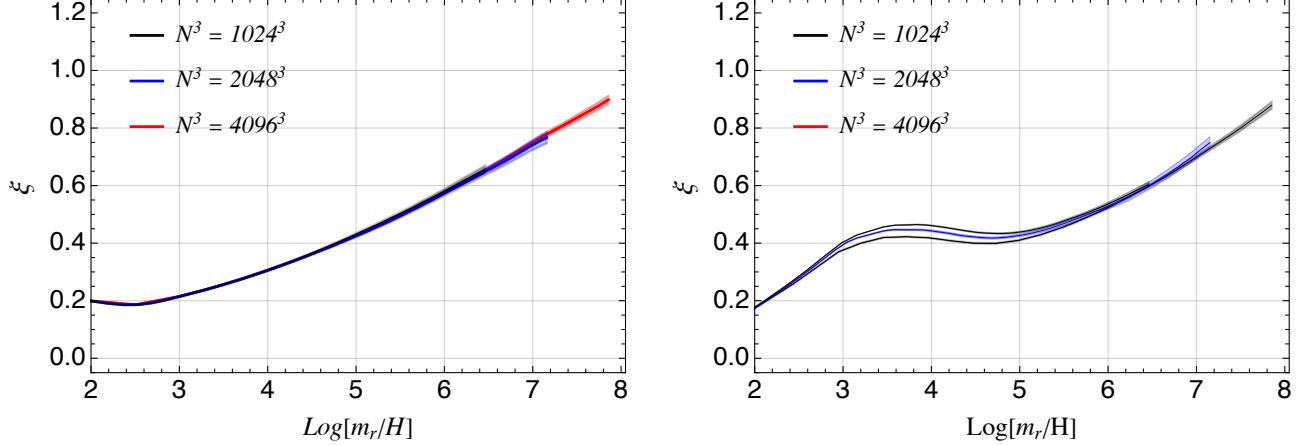


Figure 20: The independence of ξ curves on the lattice spacing Δx (and thus lattice size N as well) for simulations with the momentum cutoffs imposed.

lattice sizes in Fig. 20 indicates that the impact of the lattice spacing is not relevant as long as the string core includes at least one grid at the final time, or $n_c = 1$. At the final time of the simulation with $N^3 = 1024^3$ where $n_c^{1024} = 1$, the number of grids within the string core for the simulation with $N^3 = 2048^3$ is $n_c^{2048}|_{t_f^{1024} \sim 6.3} = \sqrt{2}$.

To quantify the quality of the scaling solution, we fit the curves to the form in Eq. (6). Given an ensemble of N_{ens} independent runs for ξ curves, we select the N_{fit} number of sampling points in the logarithmic time $\log \frac{m_r}{H}$ for fitting the curve. The Gaussian likelihood function is constructed as

$$L(c_0, c_1, d_1) = \frac{1}{(2\pi)^{N_{\text{fit}}/2} \sqrt{\det(S)}} e^{-\frac{1}{2} \sum_{i,j=1}^{N_{\text{fit}}} (\bar{\xi}_i - \xi_i^{\text{sc}}(c_0, c_1, d_1, d_2)) (S^{-1})_{ij} (\bar{\xi}_j - \xi_j^{\text{sc}}(c_0, c_1, d_1, d_2))}, \quad (54)$$

where $\bar{\xi}_i$ is the mean of ξ data at the time $\log_i = \log \frac{m_r}{H}|_i$ and the ansatz for the scaling solution is given by $\xi_i^{\text{sc}}(c_0, c_1, d_1, d_2) = c_0 + c_1 \log_i + \frac{d_1}{\log_i} + \frac{d_2}{\log_i^2}$. The matrix S in Eq. (54) is the $N_{\text{fit}} \times N_{\text{fit}}$ covariance matrix of the sampling points along the curve whose element is given by $S_{ij} = \frac{1}{N_{\text{ens}} - 1} \sum_{k=1}^{N_{\text{ens}}} (\xi_{i,k} - \bar{\xi}_i) (\xi_{j,k} - \bar{\xi}_j)$. The uncertainties σ_{c_0} , σ_{c_1} and σ_{d_1} for the c_0 , c_1 and d_1 are estimated to be $\frac{1}{\sigma_X^2} = -\frac{\partial^2}{\partial X^2} \log L$ for $X = \{c_0, c_1, d_1\}$ at the maximizing point. One may ignore the correlation among ξ_i at different times for a large enough separation $\Delta \log$ between two consecutive \log_i , or

$$L(c_0, c_1, d_1) = \prod_{i=1}^{N_{\text{fit}}} \frac{1}{\sqrt{2\pi}\sigma_i} e^{-\frac{1}{2\sigma_i^2} (\bar{\xi}_i - \xi_i^{\text{sc}}(c_0, c_1, d_1, d_2))^2}, \quad (55)$$

where $\sigma_i^2 = \frac{1}{N_{\text{ens}} - 1} \sum_{j=1}^{N_{\text{ens}}} (\xi_{i,j} - \bar{\xi}_i)^2$. Our fitting result is presented in Table 3. We find that the fitting results are sensitive to the fit ansatz and the interval. Based on our fitting result, we select two benchmark points for further simulations on the larger lattice. For the simulation

Fat string pre-evolution				Thermal pre-evolution			
ξ_0	Lattice size (N^3)	Cuts	N_{runs}	ζ	Lattice size (N^3)	Cuts at $\tau_i = 0.1\tau_c$	N_{runs}
0.1	1024^3	$k \leq m_r$	160	0.5	1024^3	$k \leq 10m_r$	130
0.2	1024^3	$k \leq m_r$	160	1.5	1024^3	$k \leq 10m_r$	160
0.3	1024^3	$k \leq m_r$	160	1.5	1024^3	no cuts	130
0.4	1024^3	$k \leq m_r$	160	2.12	1024^3	$k \leq 10m_r$	160
0.6	1024^3	$k \leq m_r$	100	2.12	1024^3	no cuts	130
0.9	1024^3	$k \leq m_r$	100	3.0	1024^3	$k \leq 10m_r$	130
0.2	2048^3	$k \leq m_r$	100	2.12	2048^3	$k \leq 10m_r$	100
0.2	4096^3	$k \leq m_r$	100	2.12	4096^3	$k \leq 10m_r$	100

Table 3: Summary of our data set used for the analyses. Note that the cut $k \leq 10m_r$ at $\tau_i = 0.1\tau_c$ is equivalent to $k \leq m_r$ at τ_c

with the fat-string type relaxation, $\xi_0 = 0.2$ is chosen. For the one with the thermal relaxation, $\zeta = 2.12$ and $\tau_i = 0.1\tau_c = 0.1414$ is chosen.

C.2 Cosmological evolution of string network

C.2.1 Energy budget

In addition to illustrations in Section 6.1, Fig. 21 shows the dependence of the energy budgets on the initial conditions for two benchmark simulations using our large ensemble data from simulations on the lattice of $N^3 = 1024^3$. As is evident in Fig. 21, the fraction of the string energy density, ρ_s/ρ_{tot} ($\rho_s = \rho_{\text{tot}} - \rho_a - \rho_r$), tends to have a larger value for a bigger size of ξ_0 or ζ in early times. However, the hierarchy switches over the time, namely ρ_s/ρ_{tot} eventually tends to have a smaller value for a bigger ξ_0 or ζ at late times. The transition time for switching the hierarchy, or $\log \frac{m_r}{H} \sim 2.5$ (fat-string pre-evolution) and $\log \frac{m_r}{H} \sim 4.5$ (thermal pre-evolution), looks consistent with the evolution of ξ in Fig. 2. While the decreased fractional string energy density, when increasing ξ_0 , goes democratically into axions and radial modes for the case with the fat-string pre-evolution (see left panel of Fig. 21), the situation, when increasing ζ , in the case with the thermal pre-evolution (see right panel of Fig. 21) looks more difficult to interpret due to a large migration of radial modes to axions (see also more noisy spectrum in F for a smaller ζ in the right panel of Fig. 23). More detailed study on the distinctive behaviors of energy budgets originated from different relaxations will be interesting.

C.2.2 Instantaneous emission

We continue investigating the dependency of our simulation result on the initial configurations and relaxation schemes with the large ensemble data from simulations on the lattice of 1024^3 . The differential axion energy spectrum $\partial\rho_a/\partial k$ and instantaneous emission F for the curves

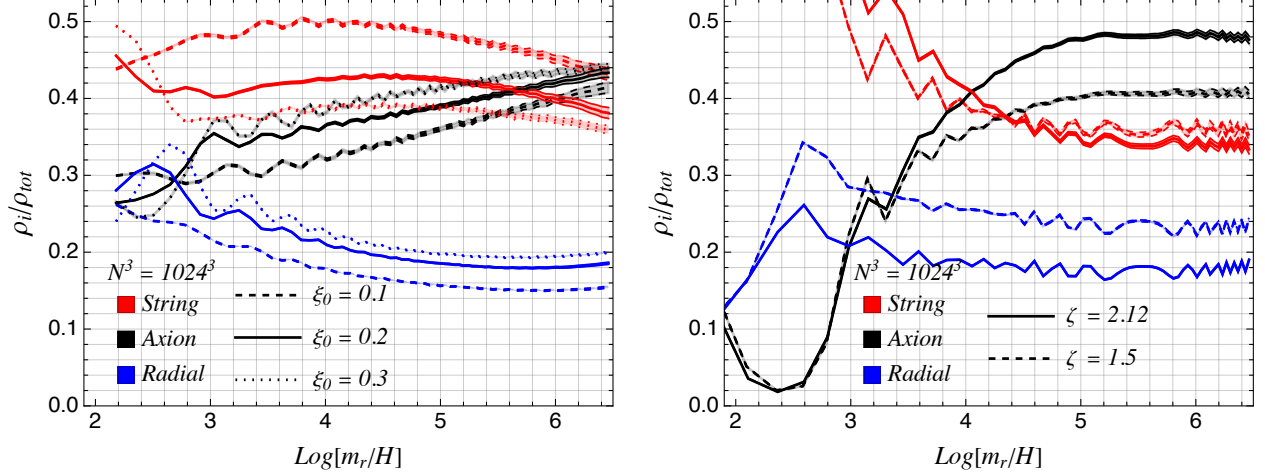


Figure 21: Energy budget for axion, radial, and string modes from simulations with different lattice sizes: $N^3 = 1024^3$ (solid), $N^3 = 2048^3$ (dashed), and $N^3 = 4096^3$ (dotted), which equivalently represents the dependence on $m_r \Delta$.

with various initial values of ξ_0 and ζ are illustrated in Figs. 22 and 23, respectively. Overall, the instantaneous emission obtained by the simulation with the thermal relaxation shows more noisy spectrum. While the larger (smaller) value of ξ populates more (less) pronounced high momentum modes which cause more (less) oscillatory instantaneous emission spectrum in the left panel of Fig. 23, the larger value of ζ appears to populate more broad range of momentum modes (see the right panel of Figs. 22) and the strength of the oscillation amplitudes in the corresponding instantaneous emissions for both $\zeta = 2.12$ and 1.5 look similar (although the case with $\zeta = 1.5$ is more noisy) as is evident in the right panel of Fig. 23. The axion emission spectra in Fig. 23 look more oscillatory than the case in [9] where the average over samples with finite-ranged initial times was considered. It may be reasonable to assume the stochastic distribution of the Hubble length during the phase transition, instead of being fixed to one specific value, and consider its influence on the instantaneous emission spectrum. It can be implemented by sampling physical string simulations over finite-ranged initial time and average over them to derive the emission spectrum as was done in [9]. We also performed the simulation taking into account the stochastic distribution of the initial Hubble length, and we confirmed that distributions become significantly smoothed. While this effect is visibly pronounced in early times where the higher modes were not relaxed enough, it gets diminished in later times beyond the time coverage of 1024^3 , for instance, it becomes less relevant in the simulation with the lattice size of $N^3 = 4096^3$.

Finally we demonstrate in Fig. 24 the impact on the differential axion energy spectrum and the instantaneous emission from UV modes shorter than string core length. The momentum cutoff set by the lattice spacing is higher than the string core scale m_r and generating those UV modes above the m_r scale significantly distorts the spectrum as is seen in Fig. 24. Although the initial field configurations above m_r are not generated at the start of the simulation, higher

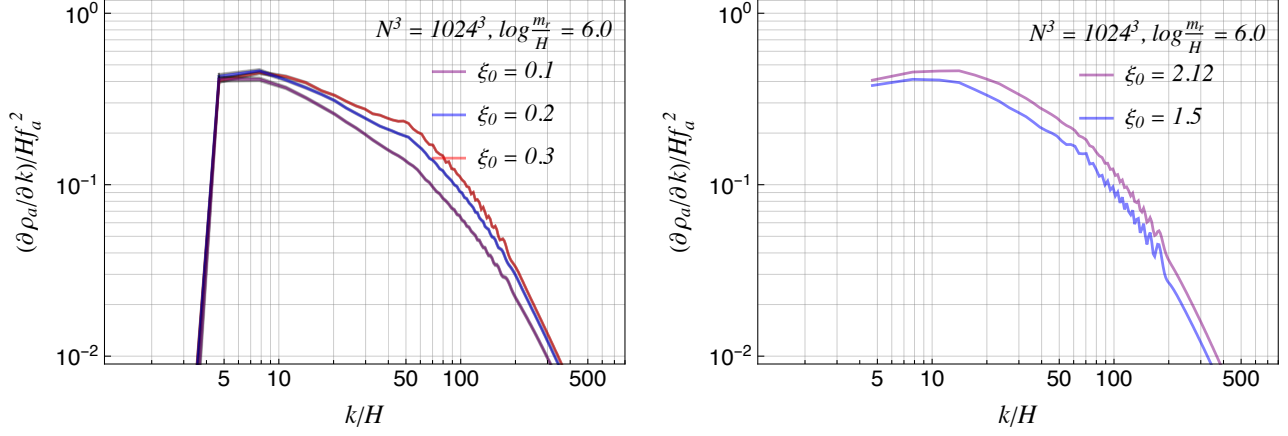


Figure 22: The differential axion energy spectrum rescaled by $H f_a^2$ at the time slice $\log \frac{m_r}{H} = 6$ for various initial conditions in two different simulation setups: fat-string type pre-evolution (left) and thermal pre-evolution (right).

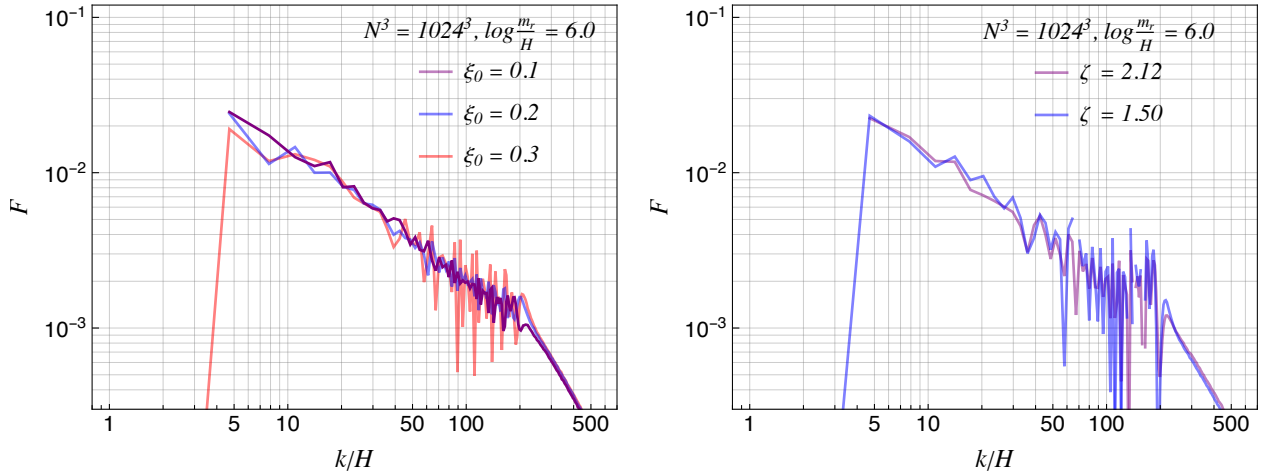


Figure 23: The instantaneous emission F at the time slice $\log \frac{m_r}{H} = 6$ for various initial conditions in two different simulation setups: fat-string type pre-evolution (left) and thermal pre-evolution (right).

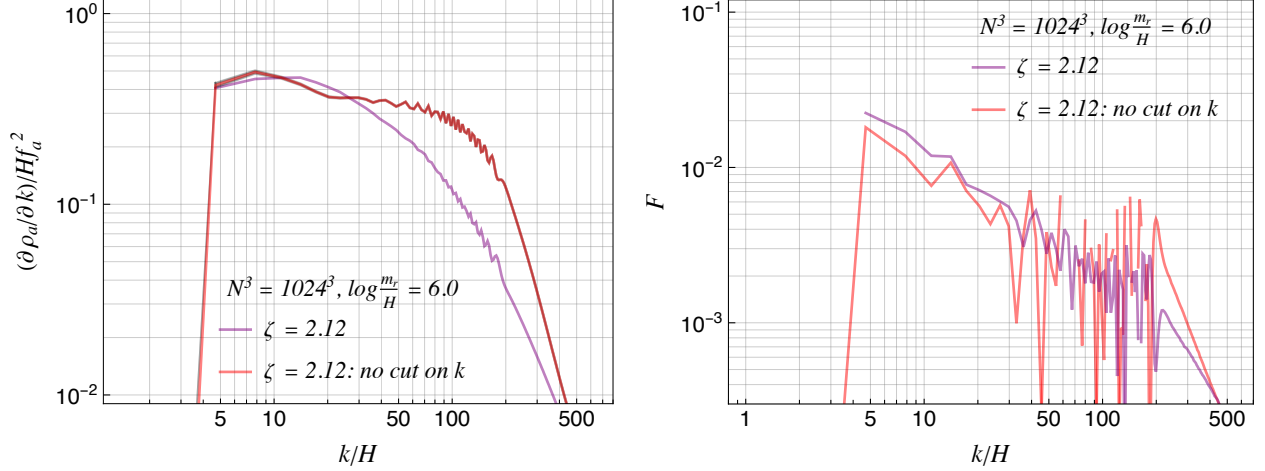


Figure 24: The differential axion energy spectrum (left) and instantaneous emission F (right) at the time slice $\log \frac{m_r}{H} = 6$ for two situations with and without the cuts on UV modes above m_r in the simulation using the thermal pre-evolution.

modes above m_r show up later through the equations of motion and their effects are much smaller compared to those from directly generated UV modes from initial random fields generation.

D More on axion spectrum

D.1 Fitting instantaneous emission function

We explain how the instantaneous emission was fitted using the ansatz for the power law fall-off profile. The spectral index q for each individual simulation is fit with the ansatz for $F(x, y)$ assuming the Gaussian distribution with the mean ax^{-q} and the standard deviation $\sigma(x, B, p, C) = Bx^{-p} + C$ (similarly to [15]) where $x = \frac{k}{H}$ is the momentum in the Hubble unit. The fit is performed within the finite range $[x_{\text{IR}}, \frac{y}{x_{\text{UV}}}]$ at a given time $y \equiv \frac{m_r}{H}$, and the fit parameters a, q, B, p and C are estimated by maximizing the likelihood function,

$$L(a, q, B, p, C) = \prod_{j=1}^{N_{\text{fit}}} \frac{1}{\sqrt{2\pi}\sigma(x_j, B, p, C)} e^{-\frac{1}{2\sigma(x_j, B, p, C)^2} (F_j - ax_j^{-q})^2} \quad (56)$$

where $\{x_j, F_j\}$ are the N_{fit} number of data points within the fit interval $x_{\text{IR}} \leq x \leq y/x_{\text{UV}}$. Our ansatz in Eq. (56) assumes no correlation among the measurements of instantaneous power spectrum at different momenta to be consistent with string core masking procedure in which the mode independence is assumed. The results from individual fits are averaged to yield the spectral index for the corresponding ensemble. They are illustrated in Figs. 14, 15, 25 and 26. The fit results of the spectral index in Figs. 25 and 26 differs from those in Figs. 14 and 15 in Section 7.1 only by the $\Delta \log$. With the increasing time interval from the default value,

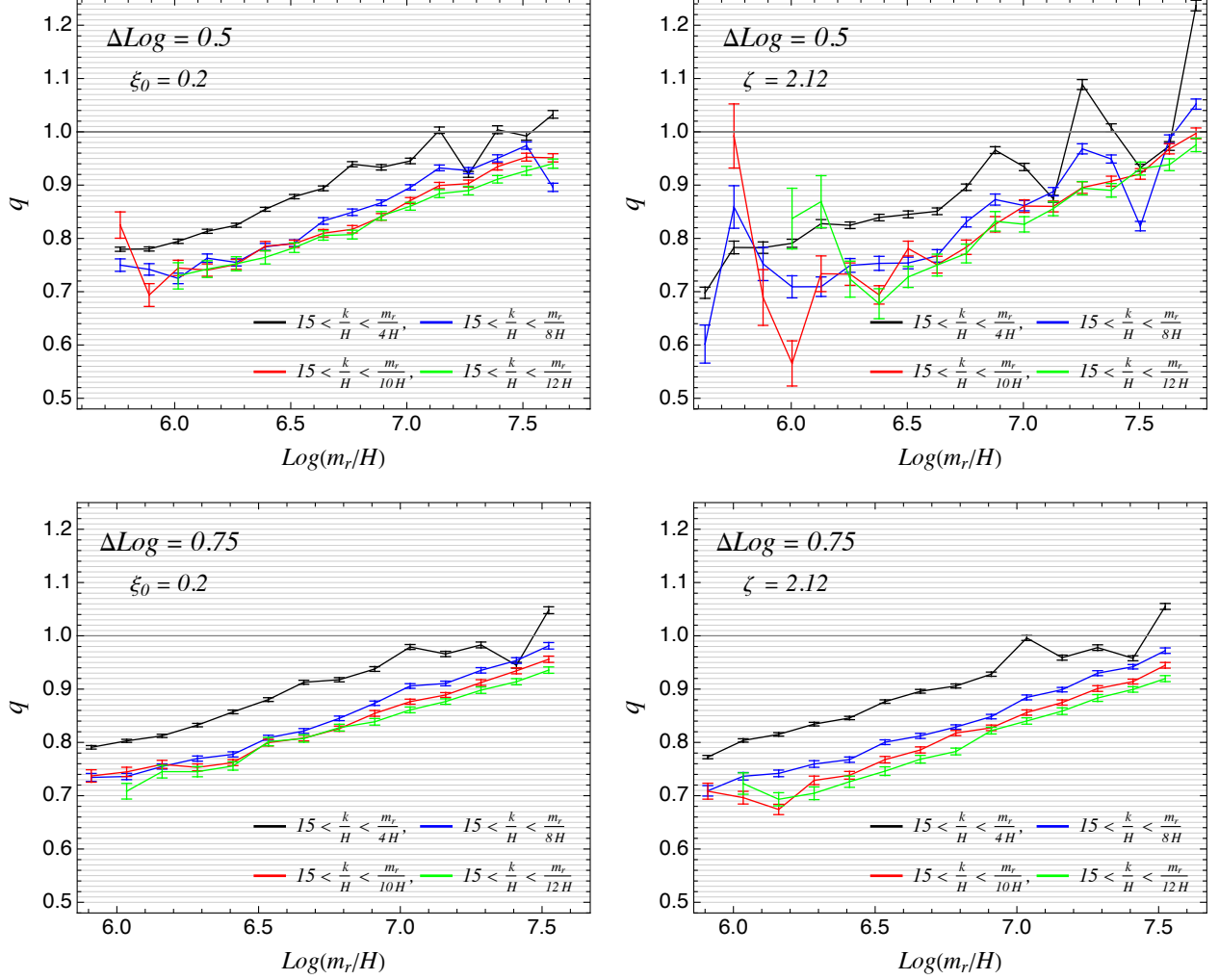


Figure 25: The spectral index q of the instantaneous emission F fitted in the interval with the varying x_{UV} while $x_{IR} = 15$. The error bars are statistical.

$\Delta \log = 0.25$, to $\Delta \log = 0.5$ and 0.75 makes the distributions smoother. As was illustrated in Figs. 14 and 15, $x_{UV} \sim 10$ looks good enough to get the stable result, and the distribution is less sensitive to x_{IR} .

While those in Figs. 14, 15, 25 and 26 are our fiducial fit results, the fits of q with no Bx^{-p} term in σ are carried out as well by setting $B = 0$ by hand. It leads to 30% deviation in slope q_1 compared to our fiducial result. Nevertheless, the conclusion from linear growth model fit expecting $q \sim O(10)$ at $\log \frac{m_r}{H} \sim 70$ is not altered.

The final fit results with two different forms of the standard deviations as well as varying UV, IR cutoffs and the time interval $\Delta \log$ are summarized in Figs. 27 and 28.

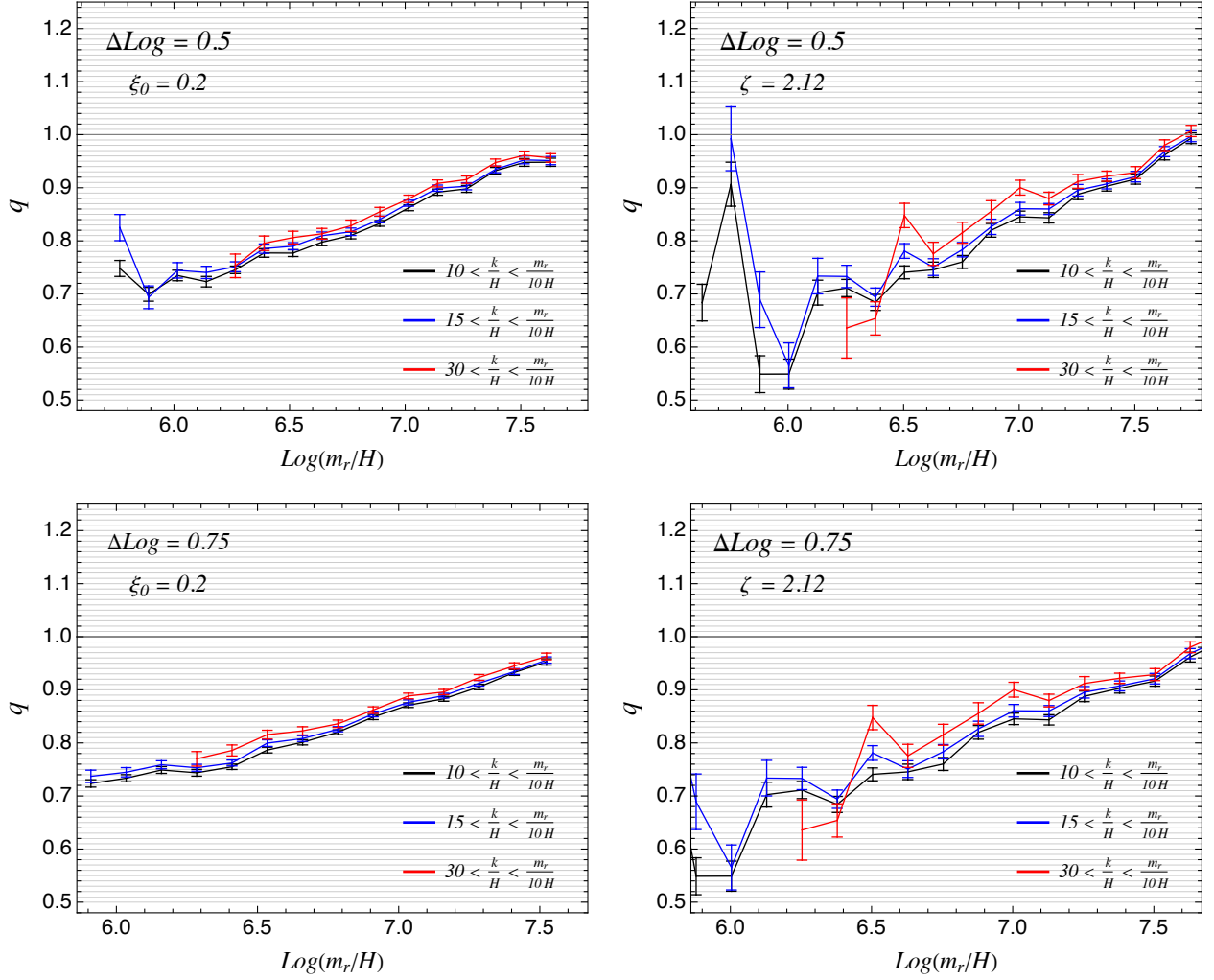


Figure 26: The spectral index q of the instantaneous emission F fitted in the interval with the varying x_{IR} while $x_{\text{UV}} = 10$. The error bars are statistical.

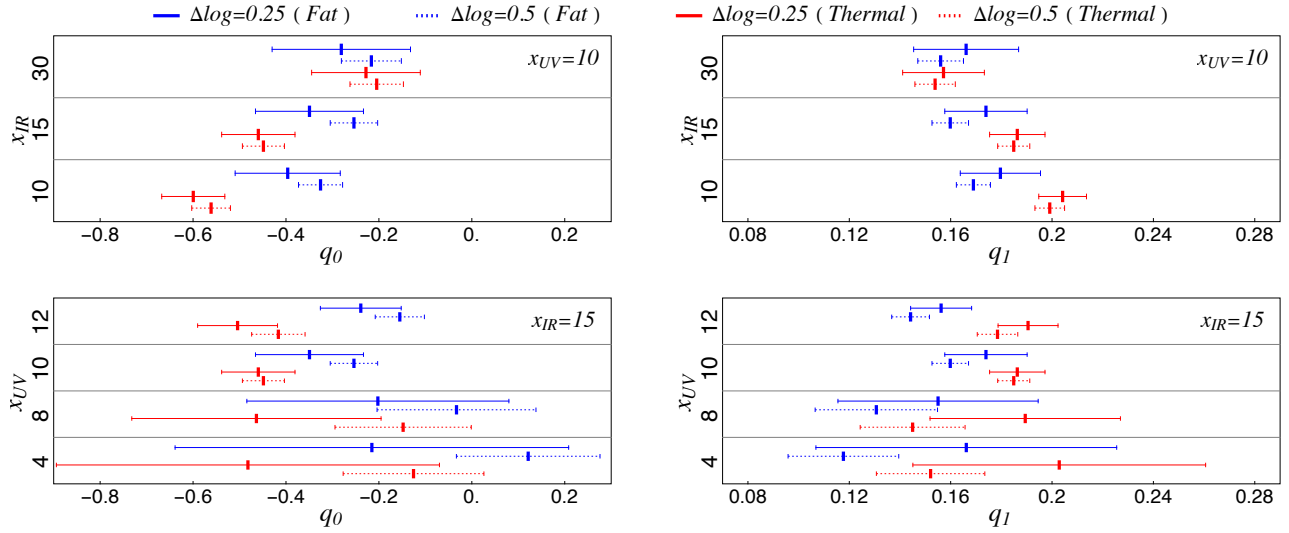


Figure 27: Our fit results on the spectral index with log-hypothesis ($q = q_0 + q_1 \log \frac{m_r}{H}$), assuming the standard deviation of the form $\sigma = Bx^{-p} + C$, for two types of relaxations (fat-string and thermal pre-evolutions) while varying x_{IR} or x_{UV} . See Appendix D.1 for the detail.

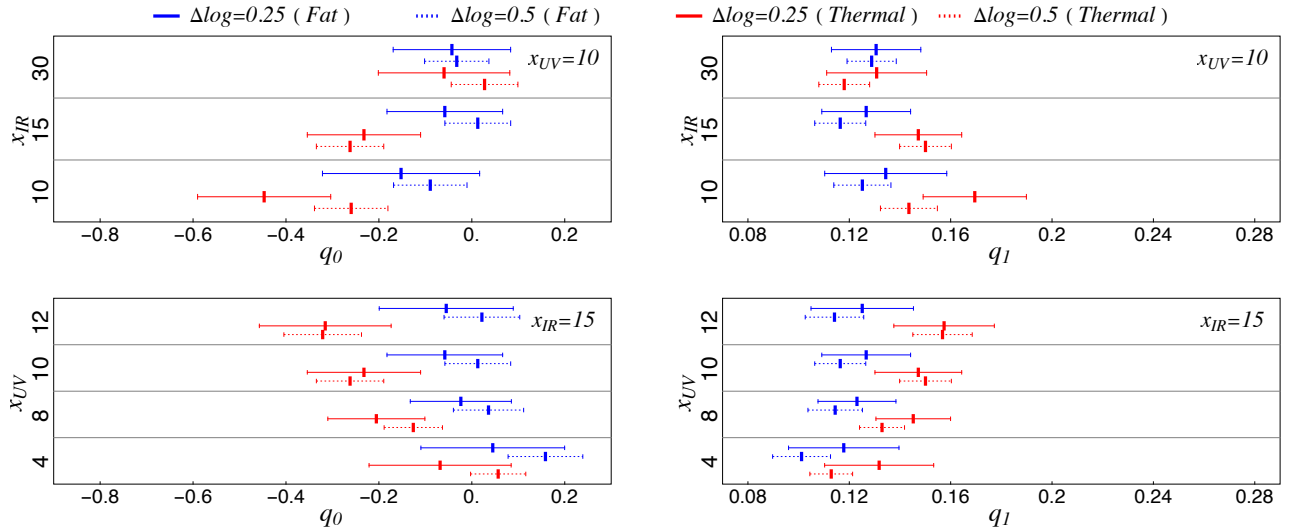


Figure 28: Our fit results on the spectral index with log-hypothesis ($q = q_0 + q_1 \log \frac{m_r}{H}$), assuming the constant standard deviation for two types of relaxations (fat-string and thermal pre-evolutions) while varying x_{IR} or x_{UV} . See Appendix D.1 for the detail.

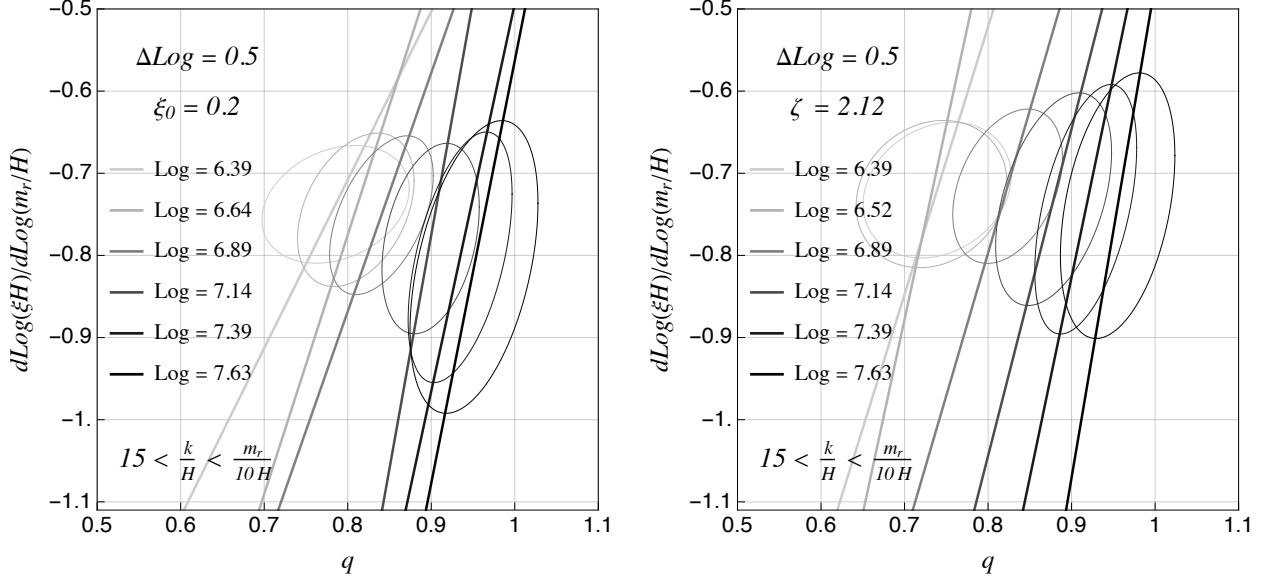


Figure 29: The correlation between the differential rate of the comoving number of strings per Hubble with respect to the logarithmic time change, $d\log(\xi H)/(d\log \frac{m_r}{H})$, and the spectral index q at various instant times from two benchmark simulations. The straight lines are major axes of the ellipses and each ellipse denotes 1-sigma contour of the Gaussian distribution over 100 individual runs.

D.2 Analytic understanding of positive correlation

Fig. 29 shows the correlation between the spectral index q and $d\log(\xi H)/(d\log \frac{m_r}{H})$ (the differential rate of the comoving number of strings per Hubble with respect to time) for multiple instant time slices to illustrate that the orientation of the correlation axes get saturated at late times while the spectral index q increases with the logarithmic time. The ellipse represents the 1σ contour around the central values, assuming the Gaussian distribution of the 100 ensemble samples at each instant time. In both simulations using the fat-string and thermal pre-evolutions, the correlation axes, which is taken from the major axis of the ellipse, similarly stay constant at later times for $\log > 7$. This correlation can hint us on how the spectral index might have shifted when a different initial condition following a different ξ evolution curve was chosen.

The positive correlation between q and $d\log(\xi H)/(d\log \frac{m_r}{H})$ can be qualitatively understood by the analytic study on the axion radiation power from sinusoidal string oscillations with small-amplitudes [26, 32]. The time averaged radiation power per unit length by long strings aligned in z -direction is given by the second harmonic at leading-order,

$$\frac{\partial P}{\partial z} \simeq \frac{\beta f_a^2}{8\lambda_{\text{str}}} \varepsilon^4, \quad (57)$$

in terms of the wavelength of the string λ_{str} , the relative amplitude $\varepsilon \equiv 2\pi A/\lambda_{\text{str}}$ which is the ratio of the amplitude A to its wavelength λ_{str} , and a constant β encoding the string geometry, for instance, $\beta = \pi^3/4$ for the sinusoidal oscillation. The relative amplitude ε is expected to not

vary much with respect to λ_{str} for being a normalized amplitude. Assuming no energy transfer to radial modes, the radiation power can be related to the decay rate of the string energy per unit length, $\partial E_{\text{str}}/\partial z$, via the energy conservation,

$$\frac{\partial}{\partial t} \frac{\partial E_{\text{str}}}{\partial z} = -\frac{\partial P}{\partial z}. \quad (58)$$

With the relation of the string energy to the string length assuming the constant string tension μ_{eff} , $\frac{\partial E_{\text{str}}}{\partial z} = \mu_{\text{eff}} \frac{\partial L_{\text{str}}}{\partial z}$, the back-reaction leads to shortening of string length L_{str} ,

$$\frac{1}{L_{\text{str}}} \frac{\partial L_{\text{str}}}{\partial t} = -\frac{1}{\partial E_{\text{str}}/\partial z} \frac{\partial P}{\partial z} \simeq -\frac{\beta f_a^2 \varepsilon^4}{8\mu_{\text{eff}} \lambda_{\text{str}}}. \quad (59)$$

As the energy is mostly radiated into axions of wavelength $\lambda_{\text{str}}/2$ [32], the relation in Eq. (59) indicates more rapid decay rate of the string length for higher-frequency (or shorter wavelength) fluctuations, which are associated with smaller spectral indices, and vice versa.

E More on axion abundance

The parametric behavior of the axion abundance crucially depends on the size of the spectral index q (whether $q > 1$ or $q = 1$), the average axion field values in the f_a unit (whether $\langle a^2 \rangle^{1/2}/f_a \ll 1$ or $\langle a^2 \rangle^{1/2}/f_a \gtrsim 1$), and the lower boundary of the momentum integral (whether $k_{\text{IR}} = H$ or $H\sqrt{\xi}$). The nature of the evolution after the scaling regime ends until the axions become nonrelativistic crucially relies on the value of $\langle a^2 \rangle^{1/2}/f_a$. The average inter-string distance is order of $1/(H\sqrt{\xi})$ as opposed to H^{-1} . The discrepancy between literature is basically originated from different set of those factors. Therefore, sorting out all possible parametric behaviors should be highly beneficial for the clearer comparison. In this section, we follows the similar computation to [14] not only filling more details, but also extending to other cases.

The axion spectrum is given by

$$\frac{\partial \rho_a}{\partial k} = \int^t dt' \frac{\Gamma(t')}{H(t')} \left(\frac{R(t')}{R(t)} \right)^3 F \left[\frac{k'}{H(t')}, \frac{m_r}{H(t')} \right], \quad (60)$$

where $k' = (R(t)/R(t'))k$ and the normalized instantaneous emission in the interval $x = [x_{\text{IR}}, y/x_{\text{UV}}]$ is given by, depending on q ,

$$F[x, y] = \begin{cases} \frac{q-1}{x_{\text{IR}}^{1-q} - \left(\frac{y}{x_{\text{UV}}}\right)^{1-q}} \frac{1}{x^q} & \text{for } q > 1 \\ \frac{1}{\log \frac{y}{x_{\text{UV}} x_{\text{IR}}}} \frac{1}{x^q} & \text{for } q = 1. \end{cases} \quad (61)$$

The transfer rate from strings to axions Γ is approximated at late times, $\Gamma \sim \xi \mu_{\text{eff}}/t^3 \sim$

$8\pi H^3 f_a^2 \xi \log \frac{m_r}{H}$ [9] where $\langle \gamma \rangle \mu_0 = \pi f_a^2$ in Eq. (11) was used in the second relation.

E.1 Estimation for $q > 1$

Following similar steps in [14], we show that modifying IR momentum cutoff can induce non-negligible change in the overall size of the axion abundance due to the slightly changed parametric behavior. Using the approximation $\xi \sim c_1 \log \frac{m_r}{H}$ at late times, the axion spectrum in Eq. (60) can be rewritten as

$$\frac{\partial \rho_a}{\partial k}(k, t) = \frac{4\pi f_a^2 c_1 m_r}{y^{3/2}} \int_{y_0}^y dy' \frac{(\log y')^2}{y'^{1/2}} F \left[\left(\frac{y'}{y} \right)^{1/2} x, y' \right], \quad (62)$$

where $x = \frac{k}{H}$, $y = \frac{m_r}{H(t)}$, and the integration over t' in the interval $[t_0, t]$ was converted in terms of $y' = \frac{m_r}{H(t')}$ with the interval $[y_0, y]$. We take into account the modified IR cutoff by setting $x_{\text{IR}} = x_0 \sqrt{\xi}$. $x_{\text{UV}} = 1$ is chosen similarly to [14] and the result is insensitive to this choice. The instantaneous emission in Eq. (61) for $q > 1$ can be approximated as

$$F[x, y] \sim \begin{cases} \frac{q-1}{x_{\text{IR}}^{1-q}} \frac{1}{x^q} & \text{for } x_0 \sqrt{\xi} = x_{\text{IR}} \leq x \leq y \\ 0 & \text{otherwise.} \end{cases} \quad (63)$$

In terms of arguments in Eq. (62), the finite support of the function F is defined by the interval $(x_0^2 c_1 \log y')^{1/2} \leq (y'/y)^{1/2} x \leq y'$ and, subsequently, it defines the integration range $y_1 \leq y' \leq y_2$ in which F in Eq. (62) is nonvanishing. There are two choices of (y_1, y_2) depending on the value of $y^{-1/2} x = \frac{k}{\sqrt{m_r H}}$.

When $y^{-1/2} x$ is large (large momentum region), the integration is done over $x^2/y = y_1 \leq y' \leq y_2 = y$ where x^2/y is the intersection between two curves y' and $(y'/y)^{1/2} x$. The integration in Eq. (62) can be done straightforwardly:

$$\begin{aligned} \frac{\partial \rho_a}{\partial k}(k, t) &= 8\pi f_a^2 c_1 m_r (x_0^2 c_1)^{\frac{q-1}{2}} y^{\frac{q-3}{2}} \frac{1}{x^q} \left(\frac{q-1}{2} \right)^{-\frac{q+3}{2}} \\ &\times \left[\Gamma \left(\frac{q+5}{2}, \frac{q-1}{2} \log \frac{x^2}{y} \right) - \Gamma \left(\frac{q+5}{2}, \frac{q-1}{2} \log y \right) \right], \end{aligned} \quad (64)$$

where $\Gamma(s, x) = \int_x^\infty dt t^{s-1} e^{-t}$ is the incomplete Gamma function. The variable $x^2/y = \frac{k^2}{m_r H}$ for the fixed momentum k . When $\frac{m_r}{H}$ is taken to be large, the second argument of Γ function in Eq. (64) becomes large as well. Since $\Gamma(s, x) \rightarrow x^{s-1} e^{-x}$ as $x \rightarrow \infty$, the result in Eq. (64) can be approximated as, in the large m_r/H limit,

$$\frac{\partial \rho_a}{\partial k}(k, t) \approx \frac{8H \mu_{\text{eff}} \sqrt{\xi}}{x_0} \left(\frac{H x_0 \sqrt{\xi}}{k} \right)^q f \left(\frac{m_r}{H}, \frac{k}{m_r} \right), \quad (65)$$

where $\pi f_a^2 \log y \sim \mu_{\text{eff}}$ and $c_1 \log y \sim \xi$ and the function $f(y, u)$ is defined as

$$f(y, u) = \left(\frac{\log(yu^2)}{u^2 \log y} \right)^{\frac{q+3}{2}} u^4 - 1. \quad (66)$$

Since $f(y, 1) = 0$ and $\partial f / \partial u < 0$ for $\exp \frac{q+3}{2(q-1)} < y^{1/2} u = \frac{k}{\sqrt{m_r H}}$, the function $f(y, u)$ is positive decreasing function in u for $u < 1$. Therefore, we see that $\partial \rho_a / \partial k$ rapidly decays faster than $\sim k^{-q}$ for the momentum $k \gtrsim e^{\frac{q+3}{2(q-1)}} \sqrt{m_r H}$, and its contribution to the axion abundance will be accordingly suppressed.

When $y^{-1/2} x$ is small (low momentum region), the integration is done over $-\frac{x_0^2 c_1 y}{x^2} W_{-1}(-\frac{x^2}{x_0^2 c_1 y}) = y_1 \leq y' \leq y_2 = y$ where y_1 in terms of Lambert W function is the intersection between two curves $(y'/y)^{1/2} x$ and $(x_0^2 c_1 \log y')^{1/2}$. The integration in Eq. (62) can also be done straightforwardly and it is given by

$$\begin{aligned} \frac{\partial \rho_a}{\partial k}(k, t) &= 8\pi f_a^2 c_1 m_r (x_0^2 c_1)^{\frac{q-1}{2}} y^{\frac{q-3}{2}} \frac{1}{x^q} \left(\frac{q-1}{2} \right)^{-\frac{q+3}{2}} \\ &\times \left[\Gamma \left(\frac{q+5}{2}, \frac{q-1}{2} \log \left(-\frac{x_0^2 c_1 y}{x^2} W_{-1} \left(-\frac{x^2}{x_0^2 c_1 y} \right) \right) \right) - \Gamma \left(\frac{q+5}{2}, \frac{q-1}{2} \log y \right) \right], \\ &= 8\pi f_a^2 c_1 m_r (x_0^2 c_1)^{\frac{q-1}{2}} y^{\frac{q-3}{2}} \frac{1}{x^q} \left(\frac{q-1}{2} \right)^{-\frac{q+3}{2}} \\ &\times \left[\Gamma \left(\frac{q+5}{2}, -\frac{q-1}{2} W_{-1} \left(-\frac{x^2}{x_0^2 c_1 y} \right) \right) - \Gamma \left(\frac{q+5}{2}, \frac{q-1}{2} \log y \right) \right], \end{aligned} \quad (67)$$

where $\log(-wW_k(-w^{-1})) = -W_k(-w^{-1})$ was used in the second relation. It can be easily shown that $-W_{-1}(-w^{-1})$ becomes large at large y for the low momentum. Using $\Gamma(s, x) \rightarrow x^{s-1} e^{-x}$ as $x \rightarrow \infty$ as before, the expression in Eq. (67) can similarly be approximated as, in the large $\log \frac{m_r}{H}$ limit,

$$\frac{\partial \rho_a}{\partial k}(k, t) \approx \frac{8H^2 \mu_{\text{eff}} \xi}{k} \left[\left(\frac{-W_{-1} \left(-\frac{H}{m_r} \log \frac{m_r}{H} \left(\frac{k}{x_0 H \sqrt{\xi}} \right)^2 \right)}{\log \frac{m_r}{H}} \right)^2 - \left(\frac{k}{x_0 H \sqrt{\xi}} \right)^{1-q} \right], \quad (68)$$

where the identity $\exp[-W_k(-w^{-1})] = -wW_k(-w^{-1})$ was used and $\pi f_a^2 \log y \sim \mu_{\text{eff}}$ and $c_1 \log y \sim \xi$ were used for the neat expression. The above expression can be further simplified by approx-

imating the Lambert function,

$$\frac{\partial \rho_a}{\partial k}(k, t) \approx \frac{8H^2 \mu_{\text{eff}} \xi}{k} \left[\left(1 - 2 \frac{\log \frac{k}{x_0 H \sqrt{\xi}}}{\log \frac{m_r}{H}} \right)^2 - \left(\frac{k}{x_0 H \sqrt{\xi}} \right)^{1-q} \right]. \quad (69)$$

From Eq. (69), we see that axion spectrum $\partial \rho_a / \partial k$ scales as $\sim k^{-1}$ in the low momentum region $x_0 H \sqrt{\xi} \lesssim k \lesssim z_k \sqrt{m_r H}$ ¹⁶. Comparing with [14], the net effect by the modification of the IR cutoff from $x_0 H$ to $x_0 H \sqrt{\xi}$ is equivalent to shifting $k^0 = x_0 H$ (in their notation) to $k^0 = x_0 H \sqrt{\xi}$ without changing the overall factor.

Another place where the modified IR cutoff can affect is the average axion field value, $\langle a^2 \rangle^{1/2} / f_a$ where $\langle a^2(t) \rangle = \int dk k^{-2} (\partial \rho_a / \partial k)$. Using our result in Eq. (69), we can evaluate $\langle a^2(t) \rangle$ (or by a simple power counting to get the leading term) with the modified cutoff $k_{\text{IR}} = x_0 H \sqrt{\xi}$, and it gives rise to $\langle a^2(t) \rangle \approx \frac{8\mu_{\text{eff}}}{x_0^2} (1/2 - (1+q)^{-1} - \log^{-1} \frac{m_r}{H} + \log^{-2} \frac{m_r}{H})$. That is, $\langle a^2(t) \rangle \sim 4\mu_{\text{eff}}$ at late times for $q > 1$, as opposed to $\langle a^2(t) \rangle \sim 4\mu_{\text{eff}} \xi$ when the IR cutoff is $\sim H$. The ratio $\langle a^2 \rangle^{1/2} / f_a$ is reduced by the factor of $\sqrt{\xi}$. While $\langle a^2(t_*) \rangle \sim 4\mu_{\text{eff}*} \gg 1$ is still expected around the time t_* of the QCD crossover based on our simulation, it may be informative to consider the opposite case with $\langle a^2(t) \rangle^{1/2} / f_a \ll 1$ and see how the modified IR cutoff by $\sqrt{\xi}$ can change the parametric of the axion abundance. In this hypothetical situation, the nonlinearities due to the axion potential will be suppressed, and the axion number density at later time $t > t_*$ will be simply given by $n_a^{\text{str}}(t) = (H(t)/H_*)^{3/2} n_a^{\text{str}}(t_*)$ where $n_a^{\text{str}}(t_*) = \int dk k^{-1} (\partial \rho_a / \partial k) \approx 8H_* \mu_{\text{eff}*} \sqrt{\xi_*}$, as opposed to $8H_* \mu_{\text{eff}*} \xi_*$ when $k_{\text{IR}} \sim H$ was assumed. That is, the shifted cutoff by $\sqrt{\xi}$ suppresses the abundance by the factor of $\sqrt{\xi}$.

Now getting back to the our situation where a large $\langle a^2(t_*) \rangle^{1/2} / f_a$ is expected, and the nonlinearities arising due to the axion potential can not be neglected. The axions after time t_* still evolves as free relativistic fields, and the axion energy density at time $t > t_*$ is accordingly redshifted and it is given by, in the range of $x_0 \sqrt{\xi_*} H_* \bar{H} < k < z_k \sqrt{m_r \bar{H}}$,

$$\frac{\partial \rho_a}{\partial k}(k, t) \approx \frac{8H^2 \mu_{\text{eff}*} \xi_*}{k} \left[\left(1 - 2 \frac{\log \frac{k}{x_0 \sqrt{\xi_*} H_* \bar{H}}}{\log \frac{m_r}{H_*}} \right)^2 - \left(\frac{k}{x_0 \sqrt{\xi_*} H_* \bar{H}} \right)^{1-q} \right]. \quad (70)$$

The evolution continues until the transition time, denoted by t_ℓ , where the axion energy density stored in the gradient terms becomes comparable with the axion potential and during which the axion energy density is assumed to promptly converted into non-relativistic ones, namely

$$\rho_{\text{IR}}(t_\ell) = \int_{x_0 \sqrt{\xi_*} H_* \bar{H}}^{c_m m_a(t_\ell)} dk \frac{\partial \rho_a}{\partial k}(k, t_\ell) = c_V m_a^2(t_\ell) f_a^2, \quad (71)$$

¹⁶ $z_k = (-\frac{x_0^2 c_1}{2} W_{-1}(-\frac{2}{x_0^2 c_1}))^{1/4}$ can be read off from the equality $-\frac{x_0^2 c_1 y}{x^2} W_{-1}(-\frac{x^2}{x_0^2 c_1 y}) = \frac{x^2}{y}$, provided that $\frac{x^2}{x_0^2 c_1 y} < e^{-1}$, for our relevant choice of parameters, and it is found to be order one constant. The large and low momentum regions are separated below and above $\sim \sqrt{x_0 m_r \bar{H}}$ when the IR cutoff of H is used.

where c_m and c_V are order one parameters that have to be determined by numerical simulation. Axions with $k > c_m m_a$ will decay faster than those contributing to the dominant abundance. The relation in Eq. (71) leads to the condition (differs by the definition of κ compared to [14]),

$$8H_\ell^2 \mu_{\text{eff}\star} \xi_\star \left[\log \kappa \left(1 - 2 \frac{\log \kappa}{\log \frac{m_r}{H_\star}} + \frac{4}{3} \frac{\log^2 \kappa}{\log^2 \frac{m_r}{H_\star}} - \frac{1 - \kappa^{1-q}}{q-1} \right) \right] = c_V m_a^2(t_\ell) f_a^2, \quad (72)$$

where $\kappa = \frac{c_m m_a(t_\ell)}{x_0 \sqrt{\xi_\star} H_\star H}$ and $H_\ell = H(t_\ell)$. Parametrizing the axion mass as $m_a(t) = H_\star (H_\star/H)^{\alpha/4}$ with $m_a(t_\star) = H_\star$ and introducing [14],

$$z \equiv \left(\frac{m_a(t_\ell)}{H_\star} \right)^{1 + \frac{6}{\alpha}}, \quad (73)$$

we obtain, keeping only first term as the dominant one in Eq. (72) at late times $\log \gg 1$,

$$\frac{8\mu_{\text{eff}\star} \xi_\star}{c_V f_a^2} \log \left(\frac{c_m}{x_0 \sqrt{\xi_\star}} z^{\frac{\alpha+2}{\alpha+6}} \right) = z^{\frac{2(\alpha+4)}{\alpha+6}}. \quad (74)$$

Comparing with the result in [14], the modified momentum IR cutoff amounts to shifting x_0 to $x_0 \sqrt{\xi_\star}$. The axion abundance at $t = t_\ell$ is estimated as $n_a^{\text{str}}(t_\ell) = c_n \frac{\rho_{\text{IR}}(t_\ell)}{m_a(t_\ell)} = c_n c_V m_a(t_\ell) f_a^2$ whereas the contribution from the misalignment with the order one angle is $n_a^{\text{mis}}(t_\ell) = c'_n m_a(t_\star) f_a^2 (H_\ell/H_\star)^{3/2}$. Expressing $m_a(t_\ell)$ in terms of the solution z using Eq. (73) and taking ratio of two different types of contributions, we obtain

$$\frac{n_a^{\text{str}}(t_\ell)}{n_a^{\text{mis}}(t_\ell)} = \frac{c_n c_V}{c'_n} z, \quad (75)$$

where the solution z of Eq. (87) is given by

$$z = \left[-\frac{\alpha+2}{2(\alpha+4)} \frac{8\mu_{\text{eff}\star} \xi_\star}{c_V f_a^2} W_{-1} \left(-\frac{2(\alpha+4)}{\alpha+2} \frac{c_V f_a^2}{8\mu_{\text{eff}\star} \xi_\star} \left(\frac{c_m}{x_0 \sqrt{\xi_\star}} \right)^{-\frac{2(\alpha+4)}{\alpha+2}} \right) \right]^{\frac{\alpha+6}{2(\alpha+4)}}, \quad (76)$$

which is the same as that in [14] except for $x_0 \rightarrow x_0 \sqrt{\xi_\star}$. Using the relation, $-W_{-1}(-w^{-1}) = \log(w \log(w \log(\dots)))$, the above ratio of two different contributions is finally given by (in the similar form to [14])

$$\frac{n_a^{\text{str}, q>1}(t_\ell)}{n_a^{\text{mis}}(t_\ell)} = \frac{c_n c_V}{c'_n} \left[\frac{4\mu_{\text{eff}\star} \xi_\star}{c_V f_a^2} \frac{\alpha+2}{\alpha+4} \log \left(\frac{4\mu_{\text{eff}\star} \xi_\star}{c_V f_a^2} \frac{\alpha+2}{\alpha+4} \left(\frac{c_m}{x_0 \sqrt{\xi_\star}} \right)^{\frac{2(\alpha+4)}{\alpha+2}} \log(\dots) \right) \right]^{\frac{\alpha+6}{2(\alpha+4)}}. \quad (77)$$

Comparing to [14], the final result differs by the replacement of $x_0 \rightarrow x_0 \sqrt{\xi_\star}$ without changing the overall factors. Upon replacements of $\mu_{\text{eff}\star} \sim \pi f_a^2 \log_\star$, $\xi_\star \sim c_1 \log_\star$ inside log at late times, or $\log_\star \gg 1$, the shifted momentum induces the modification of the overall coefficient of the

axion abundance (and sub-leading terms) as

$$\frac{n_a^{\text{str}, q>1}(t_\ell)}{n_a^{\text{mis}}(t_\ell)} \approx \frac{c_n c_V}{c'_n} \left[\frac{4\mu_{\text{eff}\star}\xi_\star}{c_V f_a^2} \frac{\alpha}{\alpha+4} \left(\log \log \frac{m_r}{H_\star} + \mathcal{O}(\log \log \log \frac{m_r}{H_\star}) \right) \right]^{\frac{1}{2}(1+\frac{2}{\alpha+4})}, \quad (78)$$

where the factor $\frac{\alpha}{\alpha+4}$ will change to $\frac{\alpha+2}{\alpha+4}$ when using $k_{\text{IR}} = x_0 H$ as in [14]. For instance, it can cause roughly 20% reduction of the overall rate for the typical choice $\alpha = 8$.

E.2 Estimation for $q = 1$

We extend the previous discussion to the case with $q = 1$ for the sake of completeness (and for the clear comparison with literature). We primarily present the estimate with IR cutoff $x_{\text{IR}} = x_0 \sqrt{\xi}$ while commenting on the case with $x_{\text{IR}} = x_0$ when it is relevant. $x_{\text{UV}} = 1$ is chosen as before. The instantaneous emission for $q = 1$ is given by

$$F[x, y] \sim \begin{cases} \frac{1}{\log \frac{y}{x_{\text{IR}}}} \frac{1}{x} & \text{for } x_0 \sqrt{\xi} = x_{\text{IR}} \leq x \leq y \\ 0 & \text{otherwise .} \end{cases} \quad (79)$$

Since the finite support of F is the same as in Section E.1, the integration in Eq. (62) can be done similarly for large and small momenta k , or $y^{-1/2}x$ over similar integration ranges to Section E.1.

When $y^{-1/2}x$ is large, the integration gives rise to

$$\frac{\partial \rho_a}{\partial k}(k, t) = \frac{2\pi f_a^2 c_1 m_r}{yx} \left(\log^2 y - \log^2 \frac{x^2}{y} \right) \approx \frac{8H^2 \mu_{\text{eff}} \xi}{k} \frac{\log \frac{k}{H}}{\log \frac{m_r}{H}} \left(1 - \frac{\log \frac{k}{H}}{\log \frac{m_r}{H}} \right), \quad (80)$$

where $\pi f_a^2 \log y \sim \mu_{\text{eff}}$ and $c_1 \log y \sim \xi$ were used. While $\partial \rho_a / \partial k$ scales as $\sim k^{-1}$ as expected, it is multiplied by the logarithmic suppression $\frac{\log(k/H)}{\log(m_r/H)}$. Similarly, when $y^{-1/2}x$ is small, the integration is given by

$$\begin{aligned} \frac{\partial \rho_a}{\partial k}(k, t) &= \frac{2\pi f_a^2 c_1 m_r}{yx} \left[\log^2 y - \log^2 \left(-\frac{x_0^2 c_1 y}{x^2} W_{-1} \left(-\frac{x^2}{x_0^2 c_1 y} \right) \right) \right] \\ &= \frac{2\pi f_a^2 c_1 m_r}{yx} \left[\log^2 y - \left(-W_{-1} \left(-\frac{x^2}{x_0^2 c_1 y} \right) \right)^2 \right], \end{aligned} \quad (81)$$

where the relation $\log(-wW_k(-w^{-1})) = -W_k(-w^{-1})$ is used in the second relation. Using the approximate relations $\pi f_a^2 \log y \sim \mu_{\text{eff}}$ and $c_1 \log y \sim \xi$ and approximating the Lambert function,

the expression in Eq. (81) is further simplified as

$$\frac{\partial \rho_a}{\partial k}(k, t) \approx \frac{8H^2 \mu_{\text{eff}} \xi \log \frac{k}{x_0 H \sqrt{\xi}}}{k \log \frac{m_r}{H}} \left(1 - \frac{\log \frac{k}{x_0 H \sqrt{\xi}}}{\log \frac{m_r}{H}} \right). \quad (82)$$

The axion spectrum $\partial \rho_a / \partial k$ in the large momentum also scales as $\sim k^{-1}$, as is expected, with the logarithmic suppression. Unlike the situation with $q > 1$, the current case with $q = 1$ shows the power law behavior $\sim k^{-1}$ over the entire momentum range as well as the logarithmic suppression. These properties remain the same even if $x_{\text{IR}} = x_0$ is taken. It does not change $\partial \rho_a / \partial k$ except for replacing $x_0 H \sqrt{\xi}$ with $x_0 H$ and, subsequently, the splitting of the momentum range into $x_0 H < k \leq \sqrt{x_0 m_r H}$ (for low) and $\sqrt{x_0 m_r H} < k$ (for high).

Switching from $q > 1$ to $q = 1$ case also affects the average axion field value. Using the result in Eq. (82) with cutoff $k_{\text{IR}} = x_0 H \sqrt{\xi}$, the average axion field value is given by

$$\langle a^2(t) \rangle \approx \frac{2\mu_{\text{eff}}}{x_0^2 \log \frac{m_r}{H}} \quad \text{for } x_{\text{IR}} = x_0 \sqrt{\xi}, \quad (83)$$

that is, $\langle a^2(t) \rangle \sim 2\pi f_a^2$ at late times with no $\log \frac{m_r}{H}$ enhancement unlike to $q > 1$ case. However, this behavior is IR cutoff sensitive, and taking $x_{\text{IR}} = x_0$ instead gives

$$\langle a^2(t) \rangle \approx \frac{2\mu_{\text{eff}} \xi}{x_0^2 \log \frac{m_r}{H}} \quad \text{for } x_{\text{IR}} = x_0, \quad (84)$$

which has a log enhancement. It implies that the size of $\langle a^2(t_*) \rangle^{1/2} / f_a$ is not obvious in priori when $q = 1$, explicit numerical check may be necessary as in [15]. Here we discuss the parametric behavior of axion number density for both cases, one with $\langle a^2(t_*) \rangle^{1/2} / f_a \ll 1$ and the other one with $\langle a^2(t_*) \rangle^{1/2} / f_a \gg 1$. In the former case, the scaling in $\log \frac{m_r}{H_\star}$ is sensitive to the IR cutoff. As was discussed in Section E.1, the axion number density at later time $t > t_\star$ is given by $n_a^{\text{str}}(t) = (H(t)/H_\star)^{3/2} n_a^{\text{str}}(t_\star)$ where $n_a^{\text{str}}(t_\star) = \int dk k^{-1} (\partial \rho_a / \partial k) \approx \frac{8\pi f_a^2 H_\star}{x_0} \sqrt{\xi_\star}$ for $x_{\text{IR}} = x_0 \sqrt{\xi}$. The abundance is enhanced by the factor of $\sqrt{\xi_\star}$, when $x_{\text{IR}} = x_0$, or $n_a^{\text{str}}(t_\star) \approx \frac{8\pi f_a^2 H_\star \xi_\star}{x_0}$. However, this may not cause a large deviation in the abundance $n_a^{\text{str}}(t_\star)$ since ξ_\star is limited to $\xi_\star \lesssim \frac{x_0^2}{2\pi}$ to satisfy $\langle a^2(t_*) \rangle^{1/2} / f_a \lesssim 1$.

Now we discuss the latter case, where $\langle a^2(t_*) \rangle^{1/2} / f_a$ is large. Similarly to the case for $q > 1$, the axion radiation around the transition time t_ℓ is estimated by solving the relation in Eq. (71) with the axion energy density at time $t > t_\star$,

$$\frac{\partial \rho_a}{\partial k}(k, t) \approx \frac{8H^2 \mu_{\text{eff}\star} \xi_\star \log \frac{k}{x_0 \sqrt{\xi_\star H_\star H}}}{k \log \frac{m_r}{H_\star}} \left(1 - \frac{\log \frac{k}{x_0 \sqrt{\xi_\star H_\star H}}}{\log \frac{m_r}{H_\star}} \right), \quad (85)$$

in the range of $x_0 \sqrt{\xi_\star H_\star H} < k < z_k \sqrt{m_r H}$. Solving the relation in Eq. (71) and expressing in

terms of $\kappa = \frac{c_m m_a(t_\ell)}{x_0 \sqrt{\xi_\star H_\star H}}$ and $H_\ell = H(t_\ell)$ gives rise to

$$8\pi f_a^2 H_\ell^2 \xi_\star (\log \kappa)^2 \left(\frac{1}{2} - \frac{1}{3} \frac{\log \kappa}{\log \frac{m_r}{H_\star}} \right) = c_V m_a^2(t_\ell) f_a^2. \quad (86)$$

With the same parametrization of the axion mass $m_a(t)$ and introducing the z parameter as in Section E.1, we obtain, keeping only the first term in the parenthesis on the left hand side in Eq. (86),

$$\left(\frac{4\pi \xi_\star}{c_V} \right)^{\frac{1}{2}} \log \left(\frac{c_m}{x_0 \sqrt{\xi_\star}} z^{\frac{\alpha+2}{\alpha+6}} \right) = z^{\frac{\alpha+4}{\alpha+6}}, \quad (87)$$

where choosing $x_{IR} = x_0$ amounts to the replacement of $x_0 \sqrt{\xi_\star}$ with x_0 . As in Section E.1, the relative axion abundance with respect to the misalignment can be estimated using the solution z to Eq. (87) which is given by

$$z = \left[-\frac{\alpha+2}{\alpha+4} \left(\frac{4\pi \xi_\star}{c_V} \right)^{\frac{1}{2}} W_{-1} \left(-\frac{\alpha+4}{\alpha+2} \left(\frac{c_V}{4\pi \xi_\star} \right)^{\frac{1}{2}} \left(\frac{c_m}{x_0 \sqrt{\xi_\star}} \right)^{-\frac{\alpha+4}{\alpha+2}} \right) \right]^{\frac{\alpha+6}{\alpha+4}}. \quad (88)$$

Unlike the case for $q > 1$, the above solution z in Eq. (88) does not hold for an arbitrarily large ξ_\star for given fixed value of c_m . The value of $-W_{-1}(-w^{-1})$ exists only for $w \geq e$, and the solution in Eq. (88) makes sense only for ξ_\star smaller than $\left(\frac{1}{e} \frac{\alpha+2}{\alpha+4} \sqrt{\frac{4\pi}{c_V}} \right)^{\alpha+2} \left(\frac{c_m}{x_0} \right)^{\alpha+4}$, denoted by $\xi_{\star \max}$. The solution to Eq. (88) does not exist for larger values of $\xi_\star > \xi_{\star \max}$ since the low momentum range $x_0 \sqrt{\xi_\star H_\star H} < k \leq c_m m_a(t)$ (that dominantly contributes to ρ_{IR}) becomes too narrow so that $\rho_{IR}(t)$ can not be large enough to satisfy Eq. (88).

A large ξ_\star may become compatible with the solution to Eq. (88) if c_m is allowed to depend on ξ_\star . While the actual values of c_m should be determined from numerical simulations, applying the property $-W_{-1}(-w^{-1}) \geq 1$ to the solution z in Eq. (88), we obtain

$$z \geq \left(\frac{\alpha+2}{\alpha+4} \left(\frac{4\pi \xi_\star}{c_V} \right)^{\frac{1}{2}} \right)^{\frac{\alpha+6}{\alpha+4}}, \quad (89)$$

where switching inequality to equality amounts to restoring the multiplicative $-W_{-1}(-w^{-1})$ function which depends at most logarithmically on w . Finally, the axion abundance from strings in the scaling regime is estimated as

$$\frac{n_a^{\text{str}, q=1}(t_\ell)}{n_a^{\text{mis}}(t_\ell)} \approx \frac{c_n c_V}{c'_n} \left[\frac{\alpha+2}{\alpha+4} \left(\frac{4\pi \xi_\star}{c_V} \right)^{\frac{1}{2}} \right]^{1+\frac{2}{\alpha+4}}, \quad (90)$$

with a possible multiplicative factor scaling at most as $\log \log \frac{m_r}{H_\star}$.

References

- [1] R. D. Peccei and H. R. Quinn, *CP Conservation in the Presence of Instantons*, *Phys. Rev. Lett.* **38** (1977) 1440–1443.
- [2] S. Weinberg, *A New Light Boson?*, *Phys. Rev. Lett.* **40** (1978) 223–226.
- [3] F. Wilczek, *Problem of Strong P and T Invariance in the Presence of Instantons*, *Phys. Rev. Lett.* **40** (1978) 279–282.
- [4] M. Dine and W. Fischler, *The Not So Harmless Axion*, *Phys. Lett. B* **120** (1983) 137–141.
- [5] J. Preskill, M. B. Wise, and F. Wilczek, *Cosmology of the Invisible Axion*, *Phys. Lett. B* **120** (1983) 127–132.
- [6] L. F. Abbott and P. Sikivie, *A Cosmological Bound on the Invisible Axion*, *Phys. Lett. B* **120** (1983) 133–136.
- [7] D. J. E. Marsh, *Axion Cosmology*, *Phys. Rept.* **643** (2016) 1–79, [[arXiv:1510.07633](#)].
- [8] T. W. B. Kibble, *Evolution of a system of cosmic strings*, *Nucl. Phys. B* **252** (1985) 227. [Erratum: *Nucl.Phys.B* 261, 750 (1985)].
- [9] M. Gorghetto, E. Hardy, and G. Villadoro, *Axions from Strings: the Attractive Solution*, *JHEP* **07** (2018) 151, [[arXiv:1806.04677](#)].
- [10] M. Kawasaki, T. Sekiguchi, M. Yamaguchi, and J. Yokoyama, *Long-term dynamics of cosmological axion strings*, *PTEP* **2018** (2018), no. 9 091E01, [[arXiv:1806.05566](#)].
- [11] A. Vaquero, J. Redondo, and J. Stadler, *Early seeds of axion miniclusters*, *JCAP* **04** (2019) 012, [[arXiv:1809.09241](#)].
- [12] V. B. Klaer and G. D. Moore, *Global cosmic string networks as a function of tension*, *JCAP* **06** (2020) 021, [[arXiv:1912.08058](#)].
- [13] M. Buschmann, J. W. Foster, and B. R. Safdi, *Early-Universe Simulations of the Cosmological Axion*, *Phys. Rev. Lett.* **124** (2020), no. 16 161103, [[arXiv:1906.00967](#)].
- [14] M. Gorghetto, E. Hardy, and G. Villadoro, *More axions from strings*, *SciPost Phys.* **10** (2021), no. 2 050, [[arXiv:2007.04990](#)].
- [15] M. Buschmann, J. W. Foster, A. Hook, A. Peterson, D. E. Willcox, W. Zhang, and B. R. Safdi, *Dark matter from axion strings with adaptive mesh refinement*, *Nature Commun.* **13** (2022), no. 1 1049, [[arXiv:2108.05368](#)].
- [16] C. A. J. O’Hare, G. Pierobon, J. Redondo, and Y. Y. Y. Wong, *Simulations of axionlike particles in the postinflationary scenario*, *Phys. Rev. D* **105** (2022), no. 5 055025, [[arXiv:2112.05117](#)].
- [17] M. Hindmarsh, J. Lizarraga, A. Lopez-Eiguren, and J. Urrestilla, *Scaling Density of Axion Strings*, *Phys. Rev. Lett.* **124** (2020), no. 2 021301, [[arXiv:1908.03522](#)].
- [18] M. Yamaguchi, M. Kawasaki, and J. Yokoyama, *Evolution of axionic strings and spectrum of axions radiated from them*, *Phys. Rev. Lett.* **82** (1999) 4578–4581, [[hep-ph/9811311](#)].
- [19] M. Yamaguchi, *Scaling property of the global string in the radiation dominated universe*, *Phys. Rev. D* **60** (1999) 103511, [[hep-ph/9907506](#)].
- [20] M. Yamaguchi, J. Yokoyama, and M. Kawasaki, *Evolution of a global string network in a matter dominated universe*, *Phys. Rev. D* **61** (2000) 061301, [[hep-ph/9910352](#)].

- [21] M. Yamaguchi and J. Yokoyama, *Quantitative evolution of global strings from the Lagrangian view point*, *Phys. Rev. D* **67** (2003) 103514, [[hep-ph/0210343](#)].
- [22] T. Hiramatsu, M. Kawasaki, T. Sekiguchi, M. Yamaguchi, and J. Yokoyama, *Improved estimation of radiated axions from cosmological axionic strings*, *Phys. Rev. D* **83** (2011) 123531, [[arXiv:1012.5502](#)].
- [23] M. Kawasaki, K. Saikawa, and T. Sekiguchi, *Axion dark matter from topological defects*, *Phys. Rev. D* **91** (2015), no. 6 065014, [[arXiv:1412.0789](#)].
- [24] D. P. Bennett, *The evolution of cosmic strings*, *Phys. Rev. D* **33** (1986) 872. [Erratum: *Phys.Rev.D* 34, 3932 (1986)].
- [25] D. P. Bennett, *Evolution of cosmic strings. 2.*, *Phys. Rev. D* **34** (1986) 3592.
- [26] R. A. Battye and E. P. S. Shellard, *Global string radiation*, *Nucl. Phys. B* **423** (1994) 260–304, [[astro-ph/9311017](#)].
- [27] R. A. Battye and E. P. S. Shellard, *Axion string constraints*, *Phys. Rev. Lett.* **73** (1994) 2954–2957, [[astro-ph/9403018](#)]. [Erratum: *Phys.Rev.Lett.* 76, 2203–2204 (1996)].
- [28] C. J. A. P. Martins and E. P. S. Shellard, *String evolution with friction*, *Phys. Rev. D* **53** (1996) 575–579, [[hep-ph/9507335](#)].
- [29] W. Zhang, A. Myers, K. Gott, A. Almgren, and J. Bell, *AMReX: Block-Structured Adaptive Mesh Refinement for Multiphysics Applications*, [arXiv:2009.12009](#).
- [30] W. Zhang, A. Almgren, V. Beckner, J. Bell, J. Blaschke, C. Chan, M. Day, B. Friesen, K. Gott, D. Graves, M. Katz, A. Myers, T. Nguyen, A. Nonaka, M. Rosso, S. Williams, and M. Zingale, *AMReX: a framework for block-structured adaptive mesh refinement*, *Journal of Open Source Software* **4** (May, 2019) 1370.
- [31] K. Clough, P. Figueras, H. Finkel, M. Kunesch, E. A. Lim, and S. Tunyasuvunakool, *GRChombo : Numerical Relativity with Adaptive Mesh Refinement*, *Class. Quant. Grav.* **32** (2015), no. 24 245011, [[arXiv:1503.03436](#)].
- [32] A. Drew and E. P. S. Shellard, *Radiation from global topological strings using adaptive mesh refinement: Methodology and massless modes*, *Phys. Rev. D* **105** (2022), no. 6 063517, [[arXiv:1910.01718](#)].
- [33] M. J. Berger and J. Olinger, *Adaptive mesh refinement for hyperbolic partial differential equations*, *Journal of Computational Physics* **53** (1984), no. 3 484–512.
- [34] L. Fleury and G. D. Moore, *Axion dark matter: strings and their cores*, *JCAP* **01** (2016) 004, [[arXiv:1509.00026](#)].
- [35] M. Yamaguchi and J. Yokoyama, *Lagrangian evolution of global strings*, *Phys. Rev. D* **66** (2002) 121303, [[hep-ph/0205308](#)].
- [36] K. Saikawa, J. Redondo, A. Vaquero, and M. Kaltschmidt, *Spectrum of global string networks and the axion dark matter mass*, [arXiv:2401.17253](#).
- [37] T. W. B. Kibble, *Topology of Cosmic Domains and Strings*, *J. Phys. A* **9** (1976) 1387–1398.
- [38] T. W. B. Kibble, *Some Implications of a Cosmological Phase Transition*, *Phys. Rept.* **67** (1980) 183.
- [39] A. Vilenkin, *Cosmic Strings*, *Phys. Rev. D* **24** (1981) 2082–2089.

- [40] A. Albrecht and N. Turok, *Evolution of Cosmic Strings*, *Phys. Rev. Lett.* **54** (1985) 1868–1871.
- [41] D. P. Bennett and F. R. Bouchet, *Evidence for a Scaling Solution in Cosmic String Evolution*, *Phys. Rev. Lett.* **60** (1988) 257.
- [42] B. Allen and E. P. S. Shellard, *Cosmic string evolution: a numerical simulation*, *Phys. Rev. Lett.* **64** (1990) 119–122.
- [43] W. H. Press, B. S. Ryden, and D. N. Spergel, *Dynamical Evolution of Domain Walls in an Expanding Universe*, *Astrophys. J.* **347** (1989) 590–604.
- [44] J. N. Moore, E. P. S. Shellard, and C. J. A. P. Martins, *On the evolution of Abelian-Higgs string networks*, *Phys. Rev. D* **65** (2002) 023503, [[hep-ph/0107171](#)].
- [45] G. Vincent, N. D. Antunes, and M. Hindmarsh, *Numerical simulations of string networks in the Abelian Higgs model*, *Phys. Rev. Lett.* **80** (1998) 2277–2280, [[hep-ph/9708427](#)].
- [46] A. Dabholkar and J. M. Quashnock, *Pinning Down the Axion*, *Nucl. Phys. B* **333** (1990) 815–832.
- [47] R. L. Davis, *Goldstone Bosons in String Models of Galaxy Formation*, *Phys. Rev. D* **32** (1985) 3172.
- [48] R. L. Davis, *Cosmic Axions from Cosmic Strings*, *Phys. Lett. B* **180** (1986) 225–230.
- [49] D. Harari and P. Sikivie, *On the Evolution of Global Strings in the Early Universe*, *Phys. Lett. B* **195** (1987) 361–365.
- [50] C. Hagmann, S. Chang, and P. Sikivie, *Axions from string decay*, *Nucl. Phys. B Proc. Suppl.* **72** (1999) 81–86, [[hep-ph/9807428](#)].
- [51] D. H. Lyth, *Axions and inflation: Vacuum fluctuations*, *Phys. Rev. D* **45** (May, 1992) 3394–3404.
- [52] P. Sikivie, *Axion Cosmology*, *Lect. Notes Phys.* **741** (2008) 19–50, [[astro-ph/0610440](#)].
- [53] T. Hiramatsu, M. Kawasaki, K. Saikawa, and T. Sekiguchi, *Axion cosmology with long-lived domain walls*, *JCAP* **01** (2013) 001, [[arXiv:1207.3166](#)].
- [54] T. Hiramatsu, M. Kawasaki, K. Saikawa, and T. Sekiguchi, *Production of dark matter axions from collapse of string-wall systems*, *Phys. Rev. D* **85** (2012) 105020, [[arXiv:1202.5851](#)].
[Erratum: *Phys.Rev.D* 86, 089902 (2012)].
- [55] P. Fox, A. Pierce, and S. D. Thomas, *Probing a QCD string axion with precision cosmological measurements*, [hep-th/0409059](#).
- [56] G. Grilli di Cortona, E. Hardy, J. Pardo Vega, and G. Villadoro, *The QCD axion, precisely*, *JHEP* **01** (2016) 034, [[arXiv:1511.02867](#)].